

https://dspace.org/

Synthesis and characterization of nano-crystalline diamond films

Chimowa, George

2011-09-13
http://hdl.handle.net/10539/10410

Downloaded from a DSpace repository. https://dspace.org/

Synthesis and Characterization of Nano-crystalline Diamond Films

George Chimowa

School of Physics

University of the Witwatersrand, Johannesburg

Supervisor: Prof S. Bhattacharyya

A dissertation submitted to the Faculty of Science, University of the Witwatersrand, Johannesburg, in fulfillment of the requirements for the degree of Master of Science.

Johannesburg, 2011

Declaration

I declare that this thesis is my own, unaided work. It is being submitted for the Degree of Master of Science in the University of the Witwatersrand, Johannesburg. It has not been submitted before for any degree or examination in any other University.

The work of other researchers is greatly acknowledged when used as references.

_____

(Signature of candidate)

_____ Day of _____ 20 _____

..Dissertation for a Master of Science Degree.

Abstract

The objective of this project is to understand the details of the electronic transport in low dimensional carbon structures at low temperatures as well as high magnetic fields. The emphasis is on the quasi-2 dimensional thin grain boundary regions of nanodiamond films and one dimensional carbon nanotubes. As such nitrogen "doped" and undoped nanodiamond films were synthesized by the hot filament chemical vapor deposition method (HFCVD). The films were micro-structurally and electrically characterized using several techniques such as Raman spectroscopy, scanning electron microscopy, transmission electron microscopy, atomic force microscopy and magnetoresistance (MR) measurements. The electronic transport properties were compared to the films deposited by microwave plasma enhanced chemical vapour deposition (MWCVD). The conductivity revealed a typical semiconducting and semi-metallic behavior for the HFCVD films depending on the nitrogen percentage in the chamber. The dephasing time of the electronic wave function was found to be weakly temperature dependant i.e. $\tau_\phi \sim T^{-p}$ with $p < 1$, a behavior reported in artificial superlattices. These results show potential application of these materials in novel nano-electronic devices.

Previously the transport mechanism in nanodiamond films has been attributed to hopping conduction in the grain boundaries which is predominately disordered sp^2 phases. Our studies on nanodiamond films have however shown different mechanisms in these films. We observed very little contribution from hopping and pronounced weak localization contributions in nanodiamond films. We thus establish the significance of tunneling transport in nanodiamond films.

We also studied the electronic transport in films of metal filled multiwalled carbon nanotubes which show significant contribution from the hopping mechanism and a negative magnetoresistance at low fields that crosses over into positive MR at high magnetic fields.

Dedication

To

My

Son

(“Nathaniel, Tatenda”)

Acknowledgements

I would like to sincerely thank my Supervisor Prof S. Bhattacharyya for introducing me to nano-science, his guidance and offering support during the entire project. I have been fortunate to work in the Nanoscale-transport physics laboratory equipped with a number of state of the art facilities which helped me to complete my MSc project smoothly. I would also like to extend my gratitude to the NRF who granted me a bursary under the nanotechnology flagship project awarded to Prof Bhattacharyya.

Let me pass my gratitude to the DST/NRF centre of excellence in strong materials and the university research office for the Hot Filament Chemical Vapor Deposition (HFCVD) system and Cryogenic free measurement (CFM) system, respectively which were granted to Prof Bhattacharyya.

My appreciation goes to Dr D Churochkin for the timely insights during the analysis of electrical measurements data. Many thanks to Dr Z Chiguvare who taught me the operation of the above mentioned instruments. A big thank you also goes to MR C Sandrock and the workshop team for the technical support.

Let me also pass my gratitude to Miss E Linganiso and Prof N Coville who provided the carbon nanotube samples for my studies. Another big thank you goes to members of our research team (Christopher Coleman, Ross McIntosh, Dr K. Shah, Dr M. Katkov and Dr M. Mamo) for the wonderful research atmosphere in the Nano-Scale and Transport Physics Laboratory.

I would love to also extend my gratitude to Dr R. Erasmus who performed the Raman Spectroscopy measurements and Prof M.J. Witcomb who assisted with the electron microscopy (SEM and TEM) measurements.

Finally let me also pass my sincere gratitude to my family (wife, son and parents) who were very generous with their time allowing me to be the in the laboratory much of the time.

Table of Contents

Declaration ……..(ii)

Abstract ……..(iii)

Dedication……(iv)

Acknowledgements……(v)

Chapter 1 – Introduction……1

1.1 Early works on synthetic diamond ……1

1.2 What are Nanodiamond films?……2

1.3 Research background……2

1.4 Problem statement ……5

1.5 Research aims……5

1.6 Why polycrystalline diamond ?……6

Chapter 2- Literature Review ……7

2.1 Diamond: Geometrical Structure ……7

2.2 Substrate pretreatment……10

2.3 Synthesis techniques ……11

2.4 CVD basic concepts……13

2.5 Growth model of nanodiamond films……14

2.6 Characterization techniques ……17

2.7 Electron transport in mesoscopic systems ……19

2.8 The Drude model ……23

Chapter 3- Experimental ……25

3.1 HFCVD synthesis of nanodiamond films ……..25

3.2 Electron transport measurements……..28

3.3 Operation of the Cryogenic free measurements system……..31

3.4 Sample preparation for TEM……32

Chapter 4- Results and Discussions ……33

4.1 Effect of substrate pretreatment ……33

4.2 Optimization of the synthesis process ……..36

4.3 Conclusions on the synthesis process ……50

Chapter 5 - Electronic Transport in Nanodiamonds films ……51

5.1 Activated and hopping conduction in nanodiamond films……51

5.2 Weak localization in nanodiamond films……56

5.3 2D Weak localization in nanodiamond films……58

5.4 3D Weak localization in nanodiamond films……58

5.5 Results and analysis of the 20% HFCVD-N_2 films……..60

5.6 Results and analysis of the 22% HFCVD-N_2 films ……75

5.7 Results and analysis of the 20% MWCVD-N_2 films……81

5.8 Results and analysis of the 10% MWCVD-N_2 films ……90

5.9 Conclusions on transport in nanodiamond films……96

Chapter 6- Electronic transport in Fe-MWNT's……98

6.1 R-T Data for 5% and 27% samples compared……..98

6.2 MR in strongly localized regime of disordered systems……..99

6.3 Analysis of 5% Fe-MWNT ……101

6.4 Analysis of 27% Fe-MWNT ……103

6.5 Weak localization in Fe-MWNT……107

6.6 Conclusions on Fe-MWNT Results ……111

Chapter 7 - Conclusions and Recommendations……112

Appendix ……116

Bibliography ……117

List of Figures

Fig 1.1: Graphs of atomic nitrogen percentage in UNCD films as a function of nitrogen gas in the chamber and temperature dependence of conductivity of nitrogen doped UNCD films [10,11] -**4**

Fig 2.1: An illustration of the FCC structure of diamond and an SEM micrograph of synthetic microcrystalline diamond films from Seki Technotron USA -**7**

Fig 2.2: A schematic illustration of NCD and UNCD morphology [4] -**9**

Fig 2.3: A flow chart diagram to show the relative stabilities of carbon allotropes [7] -**9**

Fig 2.4: Schematic reaction paths showing the various surface carbon dimmers and bridge sites important for diamond growth [22] -**14**

Fig 2.5: A flow chart showing various types of diamond produced depending on the active radical [23] -**15**

Fig 2.6: Mapping graph showing the diamond growth as a function of methane/hydrogen and Argon percentages [24] -**16**

Fig 2.7: An illustration of phase relaxation length and the elastic scatterings in phase coherent region [29] -**20**

Fig 2.8: Schematic graphs showing the hopping mechanism and variation of electron energy with position and density of states [30] -**22**

Fig 2.9: An illustration of the transition from diffusive to ballistic conduction [32] -**23**

Fig 3.1: A schematic diagram of the HFCVD chamber which was used for the synthesis of nanodiamond films -**25**

Fig 3.2: A photograph of the actual HFCVD chamber used for the synthesis -**26**

Fig 3.3: A photograph showing the CFM system used for the electrical transport measurements -**29**

Fig 3.4: A schematic diagram of VTI cooling stage -**30**

Fig 4.1: SEM micrographs of different nanodiamond films which were seeded differently -**33**

Fig 4.2: AFM images of films prepared at 74 mbar showing the good seeding -**34**

Fig 4.3: SEM micrograph of a sample that shows the sharp edges of the films -**35**

Fig 4.4: TEM micrographs of films prepared at 750^{o}C -**35**

Fig 4.5: Raman Spectra of samples prepared at different temperatures -**36**

Fig 4.6: SEM images showing the effect of temperature on the cluster sizes -**37**

Fig 4.7: Raman Spectra of films prepared under different pressure -**39**

Fig 4.8: SEM images showing the effect of pressure on the nanodiamond films -**40**

Fig 4.9: Raman spectra showing the effect of filament distance from the substrate on film quality -**41**

Fig 4.10: Raman spectra showing the effect of methane concentration on the film quality -**43**

Fig 4.11: Raman spectra showing the effect of hydrogen concentration on the film quality -**45**

Fig 4.12: Raman spectra showing the effect of the use of different substrate types -**46**

Fig 4.13: Raman spectra showing the effect of doping with nitrogen on the film quality -**48**

Fig 4.14: High magnification SEM images of nitrogen doped films -**49**

Fig 5.1: Arrhenius plots of MWCVD films [10] -**51**

Fig 5.2: An illustration of the change of density of states with nitrogen percentage [37]-**52**

Fig 5.3: Electronic structures of various nitrogen centers in different N-Complexes in nanocrystalline films [38] -**53**

Fig 5.4: An illustration of temperature and nitrogen concentration of the conductivity for nitrogen doped films [38] -**54**

Fig 5.5: Schematic of the density of states of clusters in the different N-Complexes in NCD films -**55**

Fig 5.6: An illustration of weak localization with and without a magnetic field -**57**

Fig 5.7: Resistance-Temperature graph for the 20% HFCVD-N_2 films -**61**

Fig 5.8: Arrhenius plot for the 20% HFCVD-N_2 conductivity -**62**

Fig 5.9: ln R vs. $T^{-1/2}$ graph to check for 1D VRH in the 20% HFCVD-N_2 films -**64**

Fig 5.10: ln R vs. $T^{-1/3}$ graph to check for 2D VRH in the 20% HFCVD-N_2 films -**65**

Fig 5.11: ln R vs. $T^{-1/4}$ graph to check for 3D VRH in the 20% HFCVD-N_2 films -**66**

Fig 5.12: Conductance vs. Temperature for the 20% HFCVD-N_2 showing the 3D WL fit -**67**

Fig 5.13: MR results for 20% HFCVD-N_2 films -**69**

Fig 5.14: MR vs. $B^{1/2}$ for the 20% HFCVD-N_2 films -**70**

Fig 5.15: Normalized MR results with 3D WL isotropic fitting model to determine the relevance of the mechanism -**72**

Fig 5.16: Anisotropic 3D WL fit for the 20% HFCVD-N_2 MR results showing the relevance of the mechanism -**73**

Fig 5.17: A graph of the dephasing length vs. temperature for the 20% HFCVD-N_2 to determine its temperature dependence -**74**

Fig 5.18: R-T graph for the 22% HFCVD-N_2 films -**75**

Fig 5.19: ln T vs. T^{-x} to check for hopping in 22% HFCVD-N_2 films -**76**

Fig 5.20: Conductance vs. Temperature graph fitted with the 3D WL model for the 22% HFCVD-N_2 films -**77**

Fig 5.21: MR vs. Magnetic field with the 3D WL anisotropic model for the 22% HFCVD-N_2 films -**79**

Fig 5.22: A graph to determine the temperature dependence of the dephasing length for the 22% HFCVD-N_2 films -**80**

Fig 5.23: A graph showing the resistance-temperature variation below 100K for the 20%-MWCVD-N_2 films -**81**

Fig 5.24: ln R vs. T^{-x} graph to check for VRH mechanism in the 20% MWCVD-N_2 films -**82**

Fig 5.25: A graph of conductance vs. Temperature to illustrate 3D weak localization in 20% MWCVD-N_2 films -**84**

Fig 5.26: A graph showing the raw MR results for the 20% MWCVD-N_2 films -**86**

Fig 5.27: A graph of the MR vs. Temperature to determine the temperature dependence at different fields for the 20% MWCVD-N_2 films -**87**

Fig 5.28: Normalized MR results with 3D WL anisotropic fit for the 20% MWCVD-N_2 films -**88**

Fig 5.29: A graph showing the temperature dependence of the dephasing length for the 20% MWCVD-N_2 films -**89**

Fig 5.30: Conductance vs. Temperature graph with 3D weak localization fit for the 10% MWCVD-N_2 films -**90**

Fig 5.31: ln R vs. T^{-x} to check for VRH in the 10% Fe-MWCVD-N_2 films -**91**

Fig 5.32: A graph showing MR results for 10% MWCVD-N_2 films -**93**

Fig 5.33: Normalized MR results with 3D WL anisotropic fitting curves for the 10% MWCVD-N_2 films -**94**

Fig 5.34: A graph of dephasing length vs. temperature for the 10% MWCVD-N_2 films -**95**

Fig 6.1: Conductance -Temperature graphs for Fe-MWNT samples compared -**98**

Fig 6.2: ln G vs. T^{-x} to check for VRH conduction mechanism in the 5% Fe-MWNT sample -**101**

Fig 6.3: Normalized MR graph for the 5% Fe-MWNT sample -**102**

Fig 6.4: ln G vs. T^{-x} to check for VRH conduction mechanism in the 27% Fe-MWNT sample -**103**

Fig 6.5: A graph showing the normalized MR results for 27% Fe-MWNT sample -**104**

Fig 6.6: Magneto-conductance graph for the 5% and 27% Fe-MWNT samples compared at 4.3K -**105**

Fig 6.7: Conductance – Temperature results for the 27% Fe-MWNT sample fitted with the 3D WL model -**108**

Fig 6.8: Magneto-conductance results for the 27% Fe-MWNT sample fitted with the 3D WL model -**109**

List of Tables

Table 2.1: A table showing the different pretreatment methods used for substrate seeding [19] -**10**

Table 6.1: A table of the calculated parameters for the Fe-MWNT samples -**106**

Appendix A: The dimensions of the nanodiamond films used in this research -**116**

Appendix B: The dimensions of the Fe-MWNT samples used in this research -**116**

Symbols and Abbreviations used in this document

Abbreviations of the mostly used terms in this Document

CVD – Chemical vapour deposition

HFCVD – Hot filament chemical vapour deposition

MWCVD – Microwave chemical vapour deposition

MWNT- Multiwalled carbon nanotubes

GB – Grain boundaries

UNCD- Ultrananocrystalline diamond

NCD – nanocrystalline diamond

MCD – Microcrystalline diamond

SEM – Scanning Electron microscope

TEM- Transmission Electron microscope

AFM – Atomic Force Microscope

DOS – Density of States

WL – Weak localization

MR – Magnetoresistance

Fe-MWNT- Iron filled MWNT

Standard Symbols used in this document.

h- *Planks constant*

$\hbar$ - *Reduced Planks' constant.*

e – Elementary electron charge.

k_B *– Boltzmann constant.*

σ - *Conductivity.*

ρ - *Resistivity.*

G – Conductance.

T – Temperature.

B – Magnetic field.

Chapter 1

Introduction

1.1 General Introduction : Early works on synthetic diamond

The search for synthetic diamond began in the late 1800 to early 1900 with many unconfirmed reports of diamond synthesis. Some of the most talked about early works were done by Henri Moissan a French chemist who used electric arc discharge to produce diamond from charcoal **[1].** Many other Scientist tried to repeat Moissan's method but with no success. One of the most notable attempts was done by Sir Charles Algernon Parsons who spent a considerable part of his entire fortune trying to replicate Moissan's method. He probably was inspired by Moissan who had been refunded back his personal money by the French academy (about 10 000 francs), he had used in the work of separating fluorine that later won him a Noble prize. After publishing a number of articles claiming that he (Parsons) had produced some diamonds he later retracted and said "most diamonds that had been produced up to that time, by him and others were likely synthetic Spinel" **[2]**.

To create something as elegant in beauty as diamond was a very challenging task. Nevertheless driven by the thought that it should be possible because it (diamond) is essentially a huge pure carbon crystal, in 1954 reproducible synthetic diamond was reported by the H.Tracy Hall's group at the General electric company **[3]**. They used the belt press method which is now classified as High temperature and high pressure (HTHP). And ever since then many methods of diamond synthesis have come into application. But however the early methods still dominate the industry. Today synthetic diamond is a reality and the quality of it is comparable to natural diamond. The processes developed to produce these beautiful synthetic gems are a marvel of advanced research in chemistry, material science and design technology, one of which was explored in this research.

1.2 What are nanodiamond films?

Nanodiamond films are synthetic poly / single crystalline thin film diamonds whose size range from a few hundreds of nanometers to two/three nanometers. It is the crystal size that is used to classify these materials into four categories namely ultra nano-crytsatalline diamond (UNCD) films, nano-crystalline diamond (NCD) films, micro-crystalline diamond (MCD) films and single crystalline diamond. These diamond films are synthesized through technological means which is one of the subjects of this thesis and shall be further elaborated. Unlike natural diamond which is produced through geological processes, nanodiamonds are very small and this makes it relatively easy to manipulate their properties because of the large surface area and reproducible synthesis. One further interesting thing about these particles is that their mechanical properties are comparable to natural diamond and these can be exploited at nano-scale, to make miniaturized devices that can withstand harsh environments. Most importantly NCD or UNCD films have very low surface roughness compared to MCD, hence it is considered to be ideal for nano-electromechanical systems (NEMS).

1.3 Research background

In recent years nanodiamond films have caught the attention of many researchers because of their unique properties for example high hardness, excellent thermal conductivity, chemical inertness, and optical transparency over a wide spectral range just to name but a few. In addition to this it has been discovered that synthetic diamonds can be doped to produce semiconducting materials with a wide band gap and this has opened another exciting chapter on the possible applications of this novel material. Single crystal diamond which can be produced by microwave plasma chemical vapor deposition (MWCVD), is now replacing natural diamond in some cutting and abrasive tools **[4]**. The music industry is now using synthetic diamond for tweeters; the high frequency part of a loudspeaker and has improved the sound quality in one top manufacturer's products **[5]**. Doped diamond is

currently being investigated for possible application in microelectro-mechanical (MEMS) devices, while some functionalized nanodiamond films are being tried in medicine for drug delivery **[6]**.

The electronics industry to date is heavily dependent on the electrical properties of semiconductor materials (mainly silicon, germanium and gallium arsenide) whose conductivity can be manipulated by increasing or decreasing certain types of charge carriers. At the present macro-scale, these materials are reaching a limit at which they can be miniaturized into integrated circuits (IC) and reduce the cost of manufacturing. This is because of the difficulties to achieve nano-scale and still maintain the bulk properties **[7]**.

Polycrystalline nanodiamond films have a high band gap of 5.5 eV, which gives it excellent dielectric properties **[8]**. In addition to that diamond films have negative electron affinity (NEA) characteristics **[9]**. This makes them promising for electron field emission devices and related emission properties. Further to that the strong mechanical properties, chemical inertness and high carrier mobility (which reach 4500 $cm^2/(V.s)$ in single crystalline diamond, these properties make nanodiamond ideal for high power switches, fast field effect transistors for electronic devices that can be used in harsh environments, e.g. high temperatures and high radiation. The optical transparency over a wide spectral range can be utilized in making diamond lasers, optical sensors and light emitting diodes (LED) **[8]**.

At present the use of synthetic single crystal diamond as a semiconductor is limited because it cannot be doped efficiently with nitrogen, to convert it into a useful n-type material. Nitrogen doping of nanodiamond films is of great interest because it can increase the conductivity of nanodiamond films 10^4 times (**see Fig. 1.1(a)**). This is due to the fact that nitrogen atomic percentage increases four times in nanodiamond films grown with 0.5% to 20% nitrogen gas in plasma **[10, 11]**. The inclusion of dopants such as nitrogen and boron has been found to enhance the field emission characteristics of diamond **[12]**. It is worth noting that many researchers including people in our group at the University of Witwatersrand paid much attention to understand the origin of enhanced electronic

properties however the problem is still unresolved. One of the most important features from these heavily nitrogen-doped films is nearly temperature independent conductivity and the fact that high nitrogen content in the films result in metallic films while low nitrogen films are semiconducting see **Fig 1.1(b)**.

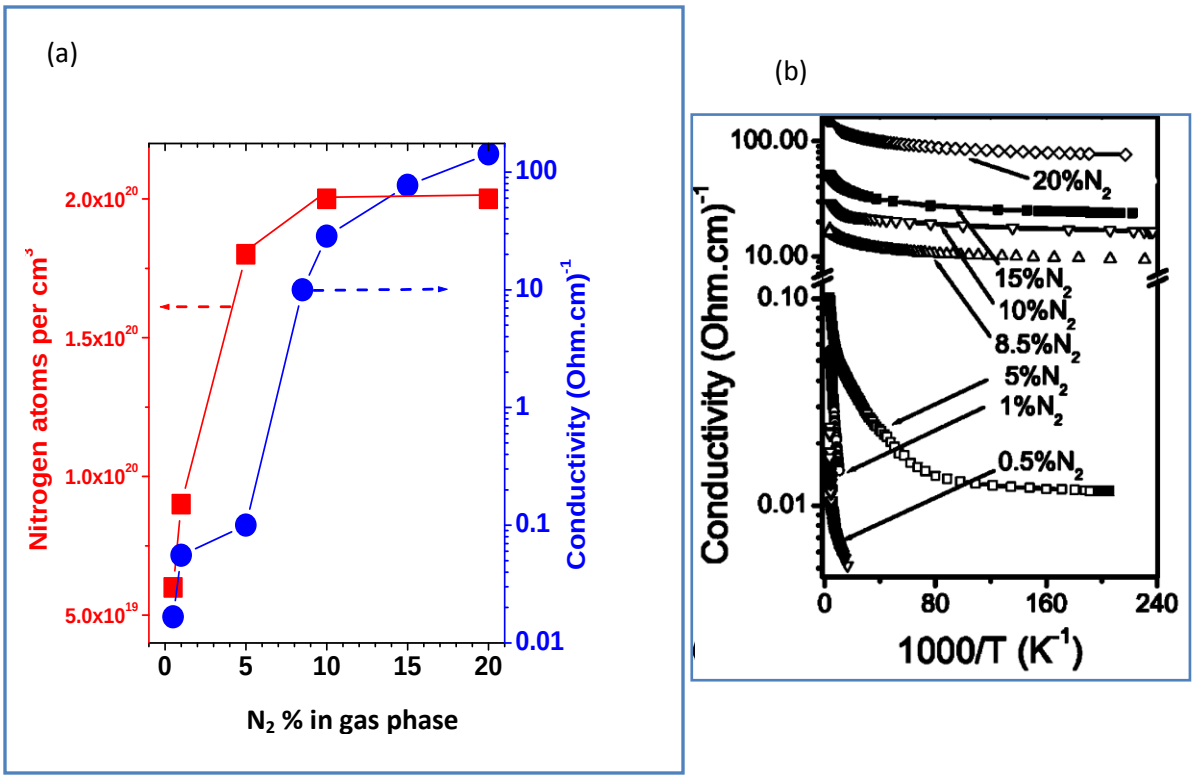


Fig 1.1.: *(a) Atomic nitrogen % (Squares) and conductivity (circles) of UNCD films as a function of nitrogen gas in the chamber [**10**]. (b): Temperature dependence in conductivity of nitrogen doped UNCD films as a function of nitrogen concentration in the films [**11**].*

Current work on diamond in electronics is still at research level with a few reports of field effect triodes and diodes **[13]**. Most of the previously reported work has been based on nanodiamond films prepared by microwave plasma CVD. This may be due to the efficiency of the method (ideal for device grade samples over large area) but it is however an expensive process currently. It is against this background that we decided to take a different direction and employ a method known as hot filament chemical vapor deposition (HFCVD) which offers a wide area deposition and is less expensive to run. In addition to that HFCVD is ideal for coating and offers excellent electrical properties when doped. Under this project an in-depth analysis of transport properties of nitrogen doped HFCVD nanodiamond films was done at various physical

conditions i.e. low temperatures, high magnetic fields. We also compare our HFCVD films with the MWCVD synthesized films.

1.4 Problem statement

As highlighted earlier there has not been much work by other groups to understand the electron transport properties of HFCVD nanodiamond films, the little that is there has only focused only on a narrow range of temperature without the effect of a strong magnetic field [**14**]. The conductivity mechanism in HFCVD nanodiamond films is still unresolved. Hence the need for further studies of electron transport properties in nanodiamond films [**11**].

In addition to that, the properties of nanodiamond films depend heavily on the synthesis process and as a result there have been many variations between laboratories and even reactors making it difficult to compare results [**15**]. Without a standard known behavior it would mean that these films will remain in the laboratories forever with no possible application in sight. It is therefore of paramount importance to study HFCVD nanodiamond and ascertain the transport properties of these films.

1.5 Research aims

There were two main aims of this research:

1.) To contribute to the understanding of the physics underlying charge carrier transport in nanodiamond films under different conditions (magnetic field, low temperature).
2.) To synthesize and improve the conductivity of HFCVD nanodiamond films by doping.

Achieving these aims will help to realize the applications of these nanodiamond films in nanotechnology. The application of nanodiamond films in nano-electronics, for example, could pave the way for the highly anticipated quantum computer, which could be faster and smaller

than today's computers [**16**]. This will possibly translate to a new age in medicine, science research, space exploration, improved and faster communication and many other applications.

1.6 Why polycrystalline nanodiamond?

At this juncture it is also important to explain why we focused on polycrystalline nanodiamond films instead of single crystalline that have the higher carrier mobility. Single crystalline diamonds have the disadvantage that they cannot be efficiently doped with nitrogen as a n-type impurities to make them semiconducting. It is believed that a dopant like nitrogen behaves as a deep impurity center in diamond, 1.7 eV below the conduction band thus making n-type doping difficult **[11]**. Furthermore it (single crystalline diamond) can only be efficiently deposited on polished diamond substrates [**17**]. While on the other hand polycrystalline diamond can be deposited on non-diamond substrates such as silicon and thus offer an opportunity to combine the silicon and diamond technology in electronic devices. Because of their polycrystalline nature (where the degree of disorder can be quite low confined to only 0.2 nm -0.4 nm grain boundary regions **[11]**) these films can easily be doped with impurities with some of the dopant elements being incorporated in the grain boundaries of the films. In this case, it also becomes interesting to understand how charge carriers tunnel through diamond crystals in what looks like a superlattice structure.

The next chapters (3, 4 & 5) will detail how the aims stated earlier were achieved. We will look into the details behind the CVD process, synthesis and characterization methods used and the theory of electron transport for both nanodiamond films and carbon nanotubes (CNTs). The main part of this thesis, which is results and discussions, is outlined before concluding with the recommendations. We also studied the transport properties of CNTs. The grain boundary regions of nanodiamond films made of sp^2 carbon is compared with the multiwalled carbon nanotubes in terms of the electron dephasing length since both of these materials have comparable values of magnetoresistance.

Chapter 2

Literature Review

2.1 Diamond: Geometrical Structure

Diamond has a modified face centered cubic (FCC) structure with a unique stacking of layers of carbon atoms. This arrangement makes diamond the toughest known solid, the best thermal conductor and gives it its transparency and optical dispersion properties. Interestingly, silicon, gallium arsenide and germanium have a diamond structure.

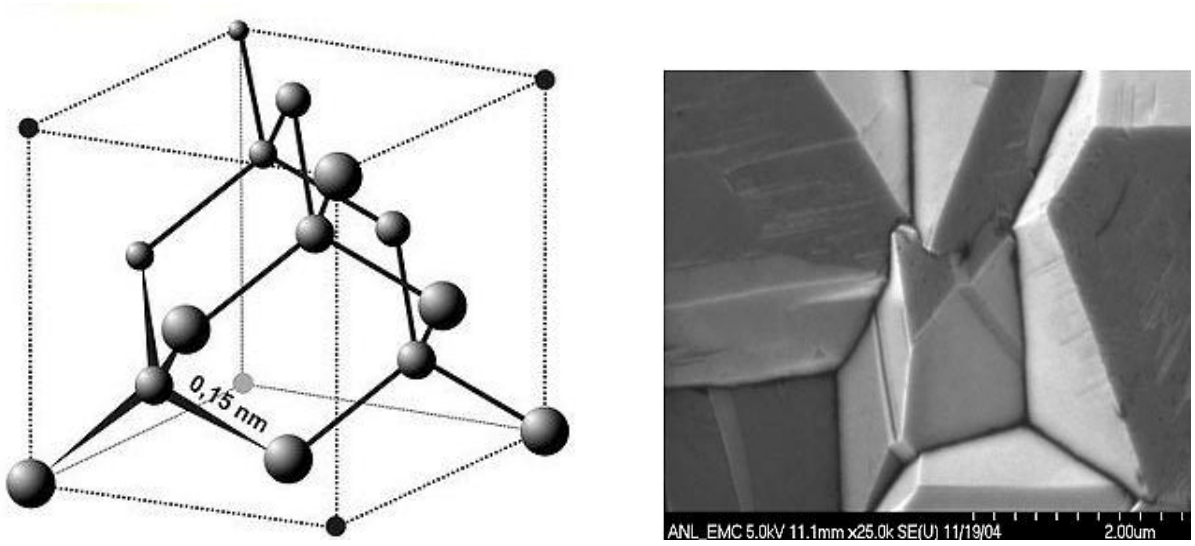


Fig 2.1 *(a) FCC structure of diamond.* *(b) SEM micrograph of industrial synthetic diamond.*

This unique and stable structure however makes it difficult to introduce needed impurities into the crystal structure and hence the need to use polycrystalline diamond in which there are grain boundaries (GB). The impurities can therefore be incorporated in these grain boundaries. Ion implantation can also be used to introduce impurities in nanodiamond and this tends to degrade the crystallinity of the diamond, its advantage however is that some impurities can be

lodged in the diamond structure. It is well known that boron can substitute carbon in the diamond lattice and hence improve the electron mobility in the structure [**18**].

As alluded to earlier, polycrystalline nanodiamond films can be classified into three categories:

- Microcrystalline diamond films (MCD)
- Nanocrystalline diamond films (NCD)
- Ultrananocrystalline diamond films (UNCD)

depending on the crystal size which we will describe briefly below.

Microcrystalline diamond films

These are nanodiamond films with grain sizes greater than a few hundred nanometers. They are rough and have wider grain boundaries which usually have amorphous carbon or diamond like carbon (DLC) depending on growth conditions. They can be deposited uniformly on a wide variety of materials depending on experimental conditions and are usually produced in hydrogen rich plasmas.

Nanocrystalline diamond films

Are smoother nanodiamond (when compared to MCD) films with grain size between one hundred and ten nanometers. They are often termed “cauliflower” or ballas diamond. They have larger number of grain boundaries with graphitic impurities.

Ultrananocrystalline diamond films

These are much smoother and denser films (better than NCD) and ideal for device application. They have grain sizes between ten and two nanometers and are prepared at relatively lower deposition temperatures. They are a result of renucleation mechanisms common in argon rich plasmas. The schematic pictures below (Fig 2.2) show the differences in UNCD and NCD morphology.

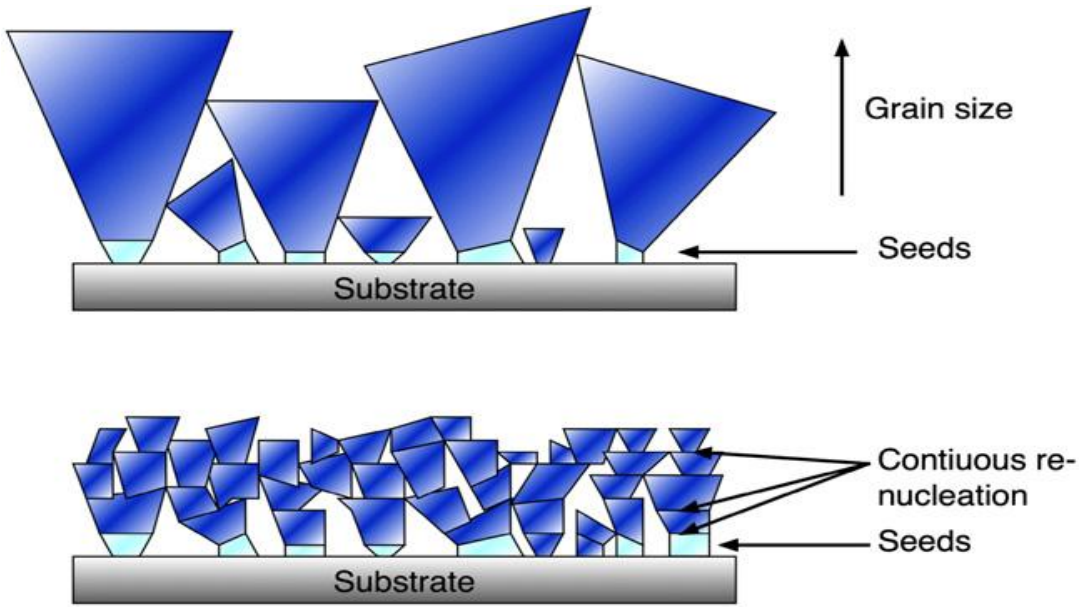


Fig 2.2: *Top: Schematic of NCD morphology. Bottom: Schematic of UNCD morphology. [**4**]*

The role of size at the nano-scale

It is well known that when the size of a material is reduced, its surface area increases. Surface area determines both physical and chemical properties e.g. catalytic activity, electrical resistivity, adhesion and stability, whether it is mechanical or chemical. This is usually true at macro scale; at nano-scale however this might not necessarily be true.

At nano-scale as the system size for all-carbon structure is increased, the most stable carbon form changes from fullerene to graphite as shown below **[7].**

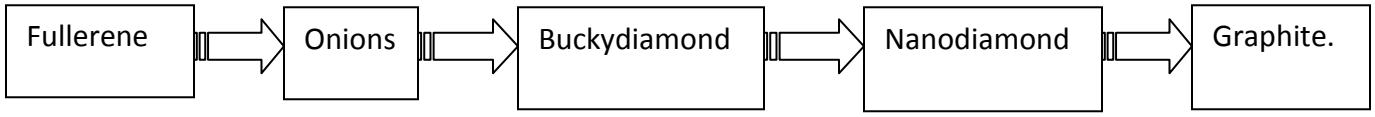


Fig 2.3*: Flow chain showing the stabilities of carbon structures and it shows that graphite is the most stable [**7**].*

It is this stability properties that determine the conditions at which nanodiamond films can be synthesized.

2.2 Substrate pretreatment

Diamond growth on quartz or silicon substrates requires that the substrate be pretreated so as to promote continuous and uniform growth of the diamond. A number of methods have been used to achieve this task and they differ in the type of substrate and application of the diamond films. The table below gives a summary of some of the methods used with their merits and demerits.

***Table 2.1**: A Table showing various methods of substrate pretreatments and their effects [**19**].*

Nucleation Method	**Nucleation Density**	**Substrate Type**	**Surface Effect**
Sonication	Up to 10^{10}	Most dielectric and Metal	Scratch surface
Bias-Enhanced Nucleation (BEN)	Up to 10^{11}	Conductive Silicon or metal	No damage
Diamond–Powder loaded Photoresist (PRD)	Approximately 10^{8}	Most dielectric and metal	No damage
Spray Paint	Up to 10^{11}	Most dielectric and metal	No damage

2.3 Synthesis techniques and the CVD

Ever since 1954 when the first confirmed and reproducible synthetic diamond was achieved, many methods of diamond synthesis have come into application. The various methods used depend on the use and type of diamond quality required. Below is a list of the various methods and where they are commonly used.

(a) **High Pressure – High Temperature** (HPHT) - This is a method which tries to replicate the natural process of diamond formation. A pure form of carbon e.g. coke or graphite is placed under very high pressure using an anvil and heated to vey high temperatures. By so doing the carbon transforms into its more stable allotrope, diamond. This method is used to make mainly micro and single crystalline diamond which has found its place in abrasives and jewellary.

(b) **Detonation of explosives** - This method uses the same principle as the HPHT method. Some carbon containing compound is detonated in a metal chamber and the high pressure and temperature created during the explosion converts the carbon into diamond. Rapid cooling prohibits the conversion of the diamond back to the more stable graphite. It is commonly used for industrial synthetic diamond.

(c) **Laser ablation** - Ablation of graphite using laser to produce diamond has of late been reported in research institutions with a couple of variations to the method. The principle used depends on the fact that laser induced carbon vapor condenses as sp^3 bonded matrix. The variations in the method are on the carrier gases, which are sometimes incorporated.

(d) **Graphite etching** - This is a method which is similar to the CVD. The only difference is that it uses a solid form of carbon (graphite) as a source of carbon which is etched by hydrogen. Its advantage is that it can be done at low substrate temperatures allowing the use of many substrates.

(e) **Chemical Vapor deposition (CVD)** - This is the most popular method for polycrystalline diamond and it is now being implemented for single crystalline diamond as well, in which case diamond substrates are required. CVD methods are used where a coated thin film is required. There are many forms of CVD techniques and they all differ in the way the activation of the precursor gases is achieved.

(i) Microwave plasma enhanced CVD (MWCVD) - uses microwave energy to activate the gases. It is perhaps one of the most widely used methods but is expensive to set up and run.

(ii) RF Plasma CVD - It uses radio frequencies (RF) for the activation purpose. It is often incorporated in other CVD's to improve the excitation of the feeder gases.

(iii) DC Plasma CVD – Makes use of direct current electrical energy and often incorporated in other CVD's just like RF plasma.

(iv) Hot Filament CVD (HFCVD) – This is perhaps the simplest, less expensive to run and maintain and allows large area deposition for nanodiamond films using multiple filaments. It makes use of a heated transition metal element such as tungsten/ tantalum or molybdenum for the activation of the precursor gases. This is the method we used and shall further be elaborated in the experimental section.

2.4 CVD- Basic concepts

In all CVD processes the objective is to set conditions well outside the region of the carbon phase, where diamond is the stable allotrope. For example, in a low pressure CVD where the synthesis was done the deposition is achieved in non-equilibrium conditions because under equilibrium conditions graphite is more stable than diamond [**20]**. Furthermore making the chamber rich with carbon favors the deposition of the graphitic phase. Thin film CVD processes are generally composed of several underlying, coupled processes:

(1) Growth Species generation – which is determined by feed gases proportions and how the activation of the precursor gases is achieved e.g. filament temperature in the case of HFCVD. A tungsten filament is known to catalyze the dissociation of hydrogen and nitrogen this helps to improve the efficiency of the system [**21**]. Overally the filament temperature determines the film morphology and grains.

(2) Gas phase diffusion – a process which is determined by the chamber pressure and the rate at which the gases are activated into reacting radicals.

(3) Homogeneous gas phase chemistry – this is one of the most important processes in the CVD, but difficult to monitor. It is determined by the gas composition, flow rates, and chamber pressure. It determines the sustenance of the growth species and hence the growth rate.

(4) Heterogeneous chemistry at the growth surface – Just like the gas phase chemistry, this is also difficult to monitor but very crucial. It is determined by the carbon diffusion coefficient of the material on which the diamond is being deposited, the efficiency of the seeding method and the substrate temperature.

Understanding these processes will help in achieving faster growth rates of high quality diamond films. At this point we will look briefly at some of the growth models put forward by other researchers on how nanodiamond films grow [see **22, 23** and **24**].

2.5 Growth model of nanodiamond films

In the study by P.May et al [**22**], Diamond growth is based upon the competition between –H, -CH_3 and C_1 radicals. They proposed that the -CH_3 radical is main reactive radical that adds on to the diamond lattice with continual abstraction of hydrogen by the –H radical. The diagrams below show some of the possible routes suggested by these researchers **[22]**.

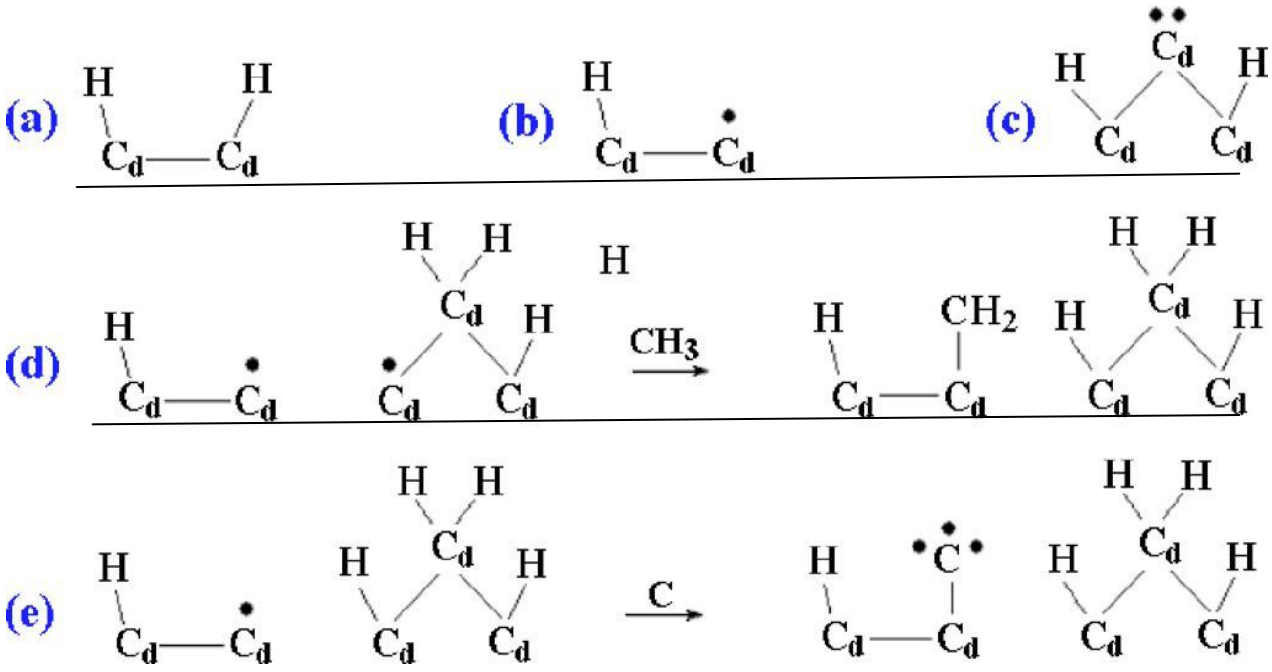


Fig 2.4: *Schematic: showing the various surface carbon radicals that form from hydrogen abstraction (a) Hydrogen terminated diamond site (b) surface radical site (c) A surface biradical site (d) Different surface biradical site followed by a reaction with methyl to give a CH_2 group (e) the radical site reacts with a C atom (not shown) to give a reactive surface Ċ. [**22**].*

The flow chart below shows the model put forward by P May et al, for determining which diamond type will form depending on the amount of the reactive radicals.

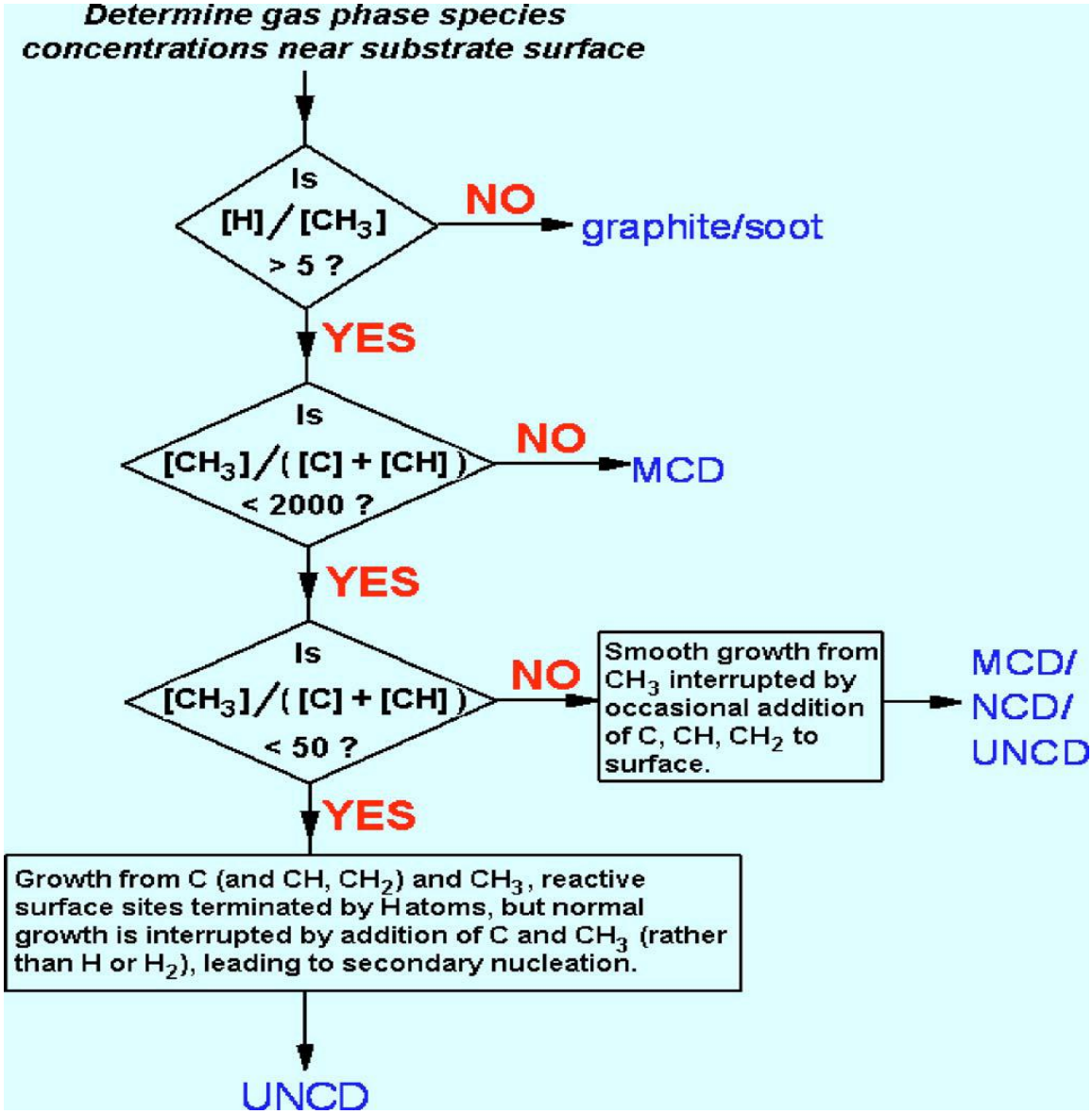


Fig 2.5*: Flow chart used to predict which diamond type can form depending on the active radical* ***[23]****.*

On the other hand, T.Lin et al **[24]** suggested a compositional mapping for an Ar- H_2 -CH_4 CVD system.

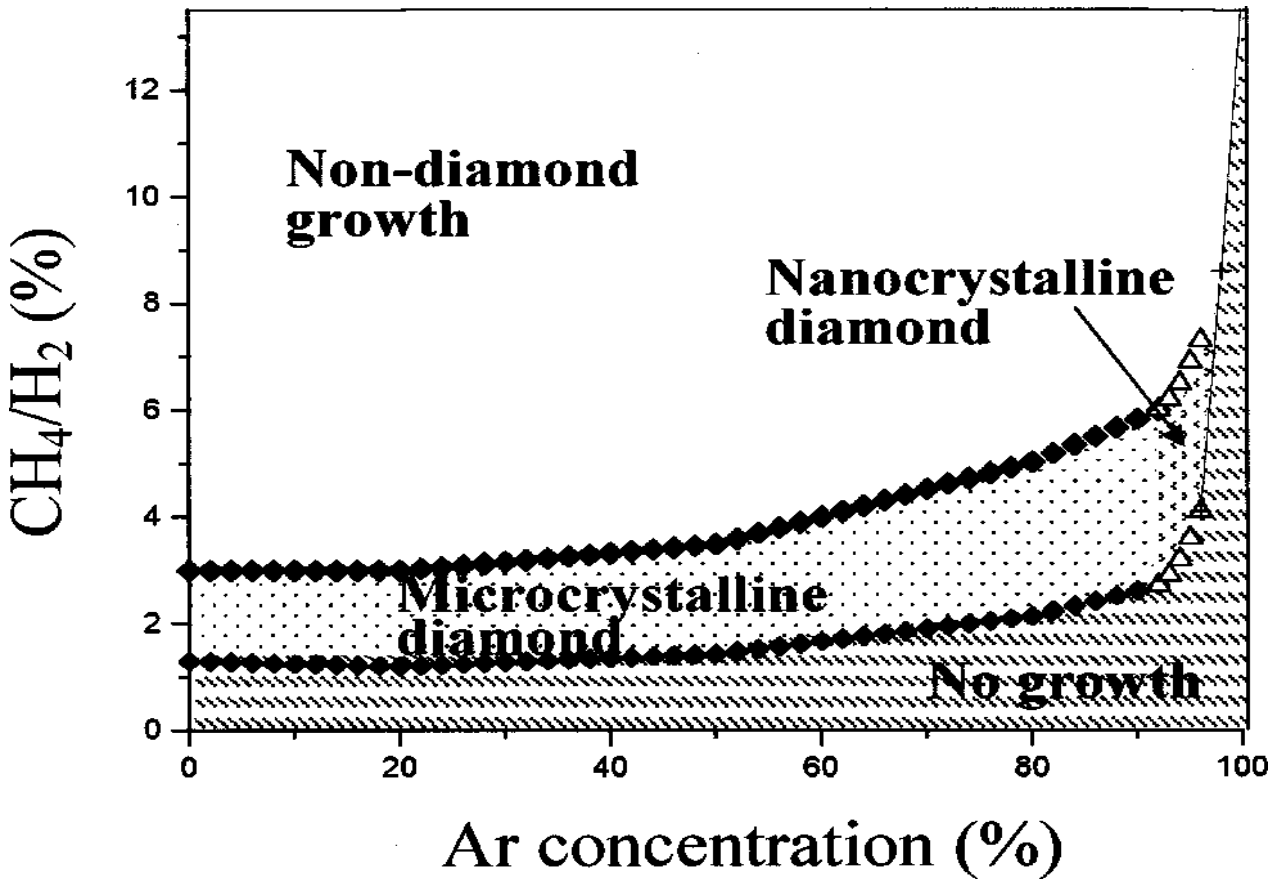


Fig 2.6: *A mapping diagram suggested by T Lin et al to determine the gas composition necessary for microcrystalline and nanocrystalline diamond films* ***[24]****.*

The diagram indicates that there is a narrow window in terms of argon , methane and hydrogen concentration under which nanocrystalline diamond films can be deposited and this is observed in an argon rich CVD with approximately 95% argon and between 3% to 5% of the methane/hydrogen percentages.

2.6 Characterization techniques

After the nanodiamond films were synthesized the next step was to do micro structural characterization and this was done using the following techniques:

(a) Raman spectroscopy

Raman spectroscopy is a common, nondestructive characterization technique for any carbon system. It is the most widely used method for establishing the crystalline quality of diamond films and this is because it is able to distinguish between sp^2 and sp^3 carbon sites. The measured spectra change with varying excitation energy. Using laser light in the visible spectrum for excitation one can only see the bond stretching and breathing modes of sp^2 sites. The sp^3 sites can only be directly determined when excitation is done using Ultraviolet (UV). Below is a list of common peaks associated with nanodiamond films **[25].**

(i) D peak (1350-1360 cm^{-1}) - due to breathing modes of sp^2 atoms in rings. Thus no rings no D peak. In NCD/UNCD it is sometimes broadened due to the small grain size of the crystals.

(ii) G peak (1560-1590 cm^{-1}) - due to bond stretching of all sp^2 atoms in both rings and chains.

(iii) Micro crystalline Diamond peak (1332 cm^{-1}) - an increase of this peak with respect to the 1580 cm^{-1} peak would indicate an increase in the microcrystalline component of the films.

(iv) T peak (1060 cm^{-1}) - only seen in UV excitation and is due to vibrations of the sp^3 C-C bonds.

(v) Trans-polyacetylene peak at 1150 cm^{-1} (and its second order at 1450-70 cm^{-1}) - these peaks are seen whenever there is UNCD although they are due to sp^2 sites; they invariably can be taken as a sign of UNCD. Some researchers however believe that these peaks are due to confined phonon modes **[26, 27]**. To date there are still debates among the research community about the origins of these peaks.

While we cannot directly determine the sp^3 content using visible excitation we can indirectly deduce the approximate percentage of sp^3 sites using the position of the G peak and the ratio of intensity I (D)/I (G) [**25].**

For Graphite _ G peak must be at 1580 cm^{-1} and I(D)/I(G) = 0

For NC-graphite _ G peak must be at 1600 cm^{-1} and I(D)/I(G) = 2.0

For a-Carbon with approximately 20% sp^3 _ G peak must be 1510 cm^{-1} and I(D)/I(G) = 0.25

DLC with 85% sp^3 _ G peak must be at 1570 cm^{-1} and I(D)/I(G) = 0.

NB. The peak positions might slightly vary due to different wavelengths of excitation.

Besides using the data above there is an alternative way of identifying DLC films i.e. using the multi-wavelength Raman spectra and measuring the G dispersion.

G dispersion (cm^{-1}/nm) = G pos (x nm) – G pos. (514.5 nm) / (514.5 –x) nm, DLC films have the largest dispersion compared to all other carbon forms. (Typical values 1690 cm^{-1} at 229 nm excitation)

(b) X-ray Diffraction (XRD)

Raman spectroscopy is a good characterization technique but it is however not very sensitive to crystalline particles like diamond, it is more sensitive to graphitic substances. In HFCVD synthesis we meet weak crystalline substances and these can be detected using XPS or XRD which are more sensitive to such substances. Below are the common peaks for CVD nanodiamond films on XRD spectrum

(i) 43.8^o peak due to (111)

(ii) 75.6^o peak due to (220)

(iii) 91.5^o peak due to (311)

(c) Scanning Electron Microscopy (SEM)

This technique is used to investigate the surface morphology of the nanodiamond films. With the help of the high spatial resolution in imaging of this instrument we get an insight into the crystal structure of the films.

(d) Atomic Force Microscopy (AFM)

Just like the SEM, it is used to investigate surface morphology and can also help to determine film thickness by making use of areas where there is no deposition.

(e) Transmission Electron Microscopy (TEM)

It is used to investigate the nanodiamond microstructure and measure accurately the crystal sizes; it can also help to shed light on the growth mechanism. The spatial resolution of this instrument can be approximately 0.2 nm [**28**]. TEM characterization on films grown on quartz or silicon requires some rigorous sample preparation which needs high precision and accuracy.

2.7 Electron transport in mesoscopic systems

To understand the electron transport properties in nanodiamond films we need to take a brief look at this subject in mesoscopic systems (i.e. materials which bridge the gap between the macro and the micro scale) in general. There exist three main regimes for which our discussion will be based. These regimes are determined by four characteristic lengths.

(a) The mean free path (L_m) which is the maximum distance that an electron travels before it is scattered.

(b) The phase relaxation length (L_φ) is the maximum distance that an electron travels without a significant change in its phase. Below is an illustration of the mathematical definition and the mechanisms in phase coherent regions. In a phase coherent region, elastic scattering is the main scattering mechanism. As a result we have multiple scattering processes in which the phase is preserved although the momentum is lost.

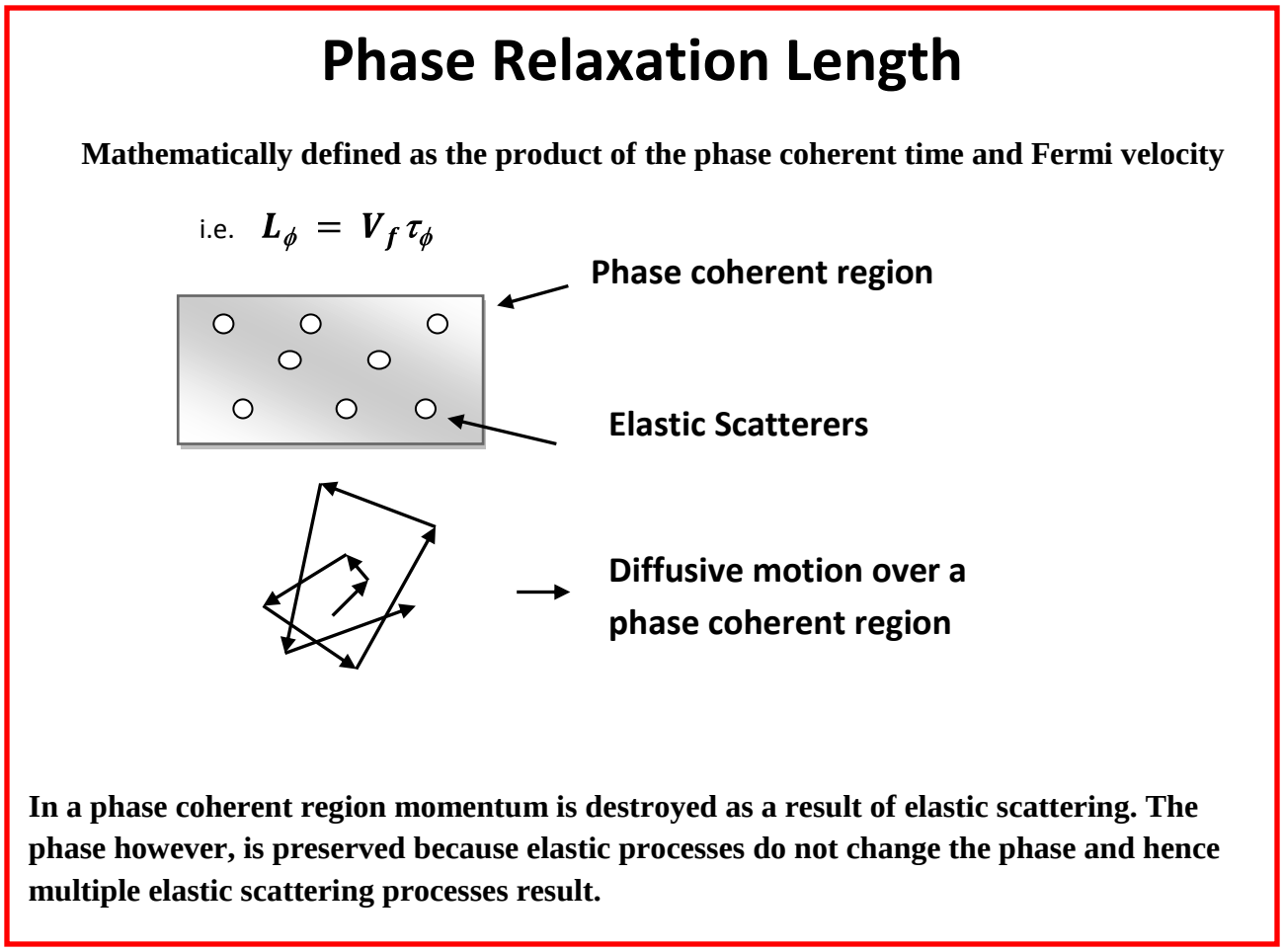


***Fig 2.7**: An illustration of phase relaxation length in a phase coherent region, the scattering mechanism is elastic and the electron motion is diffusive [**29**].*

(c) The localization length (L_c) is the average distance in which an electron is localized or trapped in an orbital.

(d) Lastly (L) is the length of the material.

The relative comparisons of these lengths, determine in which regime we are in and hence the transport mechanism (see Fig 2.9). Below are the regimes and the characteristic electron transport together with the factors that affect the relevant mechanism.

(1) **Classical:** This is the common regime which is observed in many materials. It is observed when the following condition is met $\mathbf{L_\varphi < L_m < L.}$ This is the regime in which Ohm's law and other classical laws are obeyed. It is affected by factors such as lattice vibrations, impurity scatters, material imperfections etc.

(2) **Localized regime:** It is observed under this condition $\mathbf{L_m < L_\varphi < L}$. Under this condition electron states become trapped in wells or defects and as such become localized. There are two stages of localization.

When $\mathbf{L_\varphi < L_c}$ we are in the **weak localization** regime and in this regime electron transport is diffusive. The transport mechanism is affected by quantum effects such as interference, spin interactions and magnetic impurities.

When $\mathbf{L_\varphi > L_c}$ electrons are **strongly localized** and the transport mechanism is mainly hopping of electrons from one localized site to an unoccupied site. The graphs below illustrate in terms of energy the hopping mechanism and the distribution of density of states for a strongly localized system. Hopping can be from a state of lower energy level to one with higher energy level after the absorption of a phonon or it can be within states of the same energy and results in tunneling, see Fig 2.8. In this regime, quantum effects affect the transport mechanism as in weak localization but not in the same manner.

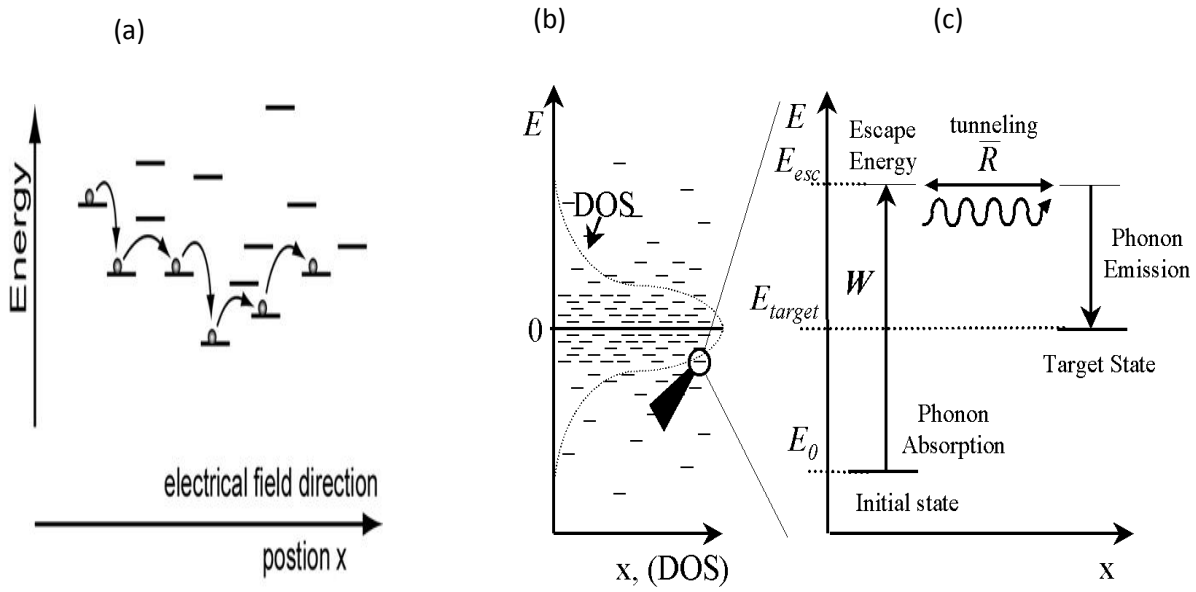


Fig 2.8: *(a) An illustration of hopping mechanism which can be from one energy level to another or same level through tunneling. (b) Distribution of density of states (c) shows the excitation of electrons from a lower energy level to a higher energy level (W) and tunneling route (R) [**30**].*

(3) **Ballistic:** This condition is observed when the following condition is met $\mathbf{L_m > L_\varphi > L}$. Under this condition the electron transport is ballistic meaning that there is no scattering and hence the material behaves like a super conductor with no resistance to the electron flow. See the illustration below Fig 2.9 (c). If the mean free path is comparable to the phase coherence length or the separation between contacts the conduction is quasi ballistic. There have been some reports of ballistic conduction at room temperature in single carbon nanotubes for both single walled (SWNT) and (multiwalled) MWNT **[31]**. The diagram below illustrates the transition from diffusive to ballistic conduction.

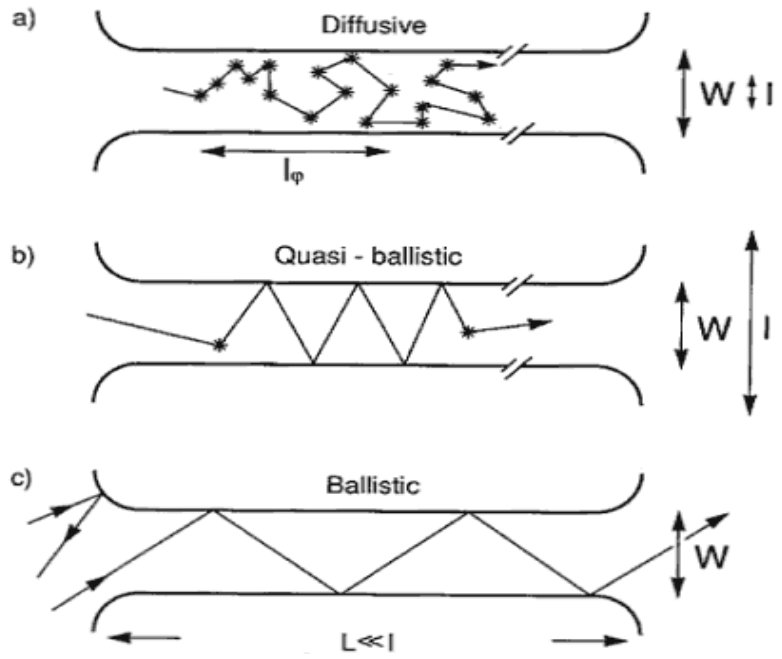


Fig 2.9: *A illustration of the transition from diffusive to ballistic conduction (a) when the separation between contacts (W) >> mean free path (l) the conduction is diffusive, if (W)≈(l), the conduction is quasi ballistic, if (W) <<(l) the conduction is ballistic. [**32**].*

In small and disordered materials such as nanodiamond films and carbon nanotubes, the small dimensions of these materials makes quantum mechanical effects and confinement to have a significant contribution to the Drude conduction model [**33**]. The quantum effects shall be explained in Chapter 5, but here we give a brief introduction to the Drude model which is a classical approach to understanding electrical conduction in metallic materials.

2.7.1 The Drude Model

This model was proposed by Paul Drude in 1900 to explain the transport properties of materials [**34**]. The model assumes the existence of free electrons in constant motion bouncing off heavier in-mobile positive ions. In essence it is an application of the kinetic theory of matter. The equation of motion for these electrons is therefore given by equation (1),

$$\frac{d}{dt}p(t) = qE - \frac{p(t)}{\tau}, \qquad (1)$$

where *t* is the time and *p, q , τ* and *E* are respectively the momentum of the electron, charge, mean free time between collisions and the electric field. From this equation (1), Drude showed that there is linear dependence between the current density (J) and the applied electric field.

$$J = \left(\frac{nq^2\tau}{m}\right)E, \qquad (2)$$

here *n* and *m* are the number density and mass of the electrons respectively.

It is from this linear relationship that explains why Ohm's law must be true. The Drude model is a good approximation to electrical conduction mechanism in the macro-scale. In the micro and nano- scale however, it is not sufficient to explain some observed phenomenon such as negative magnetoresistance. This is because of the assumptions made, namely

(a) It assumes many free electrons i.e. delocalized electrons, which might not be the case in disordered systems.
(b) It ignores long interactions between electrons and ions, which can be significant in low dimension systems.
(c) It ignores electron-electron interactions.
(d) It treats both electrons and ions as solid particles but in quantum mechanics this assumption is not very correct, the wave nature of electrons has to be taken into consideration.

As result of the above assumptions the Drude model has to be modified by incorporating some corrections to account for weak localization and electron-electron interactions in nano-materials. More details on these corrections shall be elaborated in chapter 5 and 6.

Chapter 3

Experimental

3.1 HFCVD synthesis of nanodiamond films.

The HFCVD method was used in this research to synthesize the nanodiamond films. The diagram below gives a schematic of the CVD chamber.

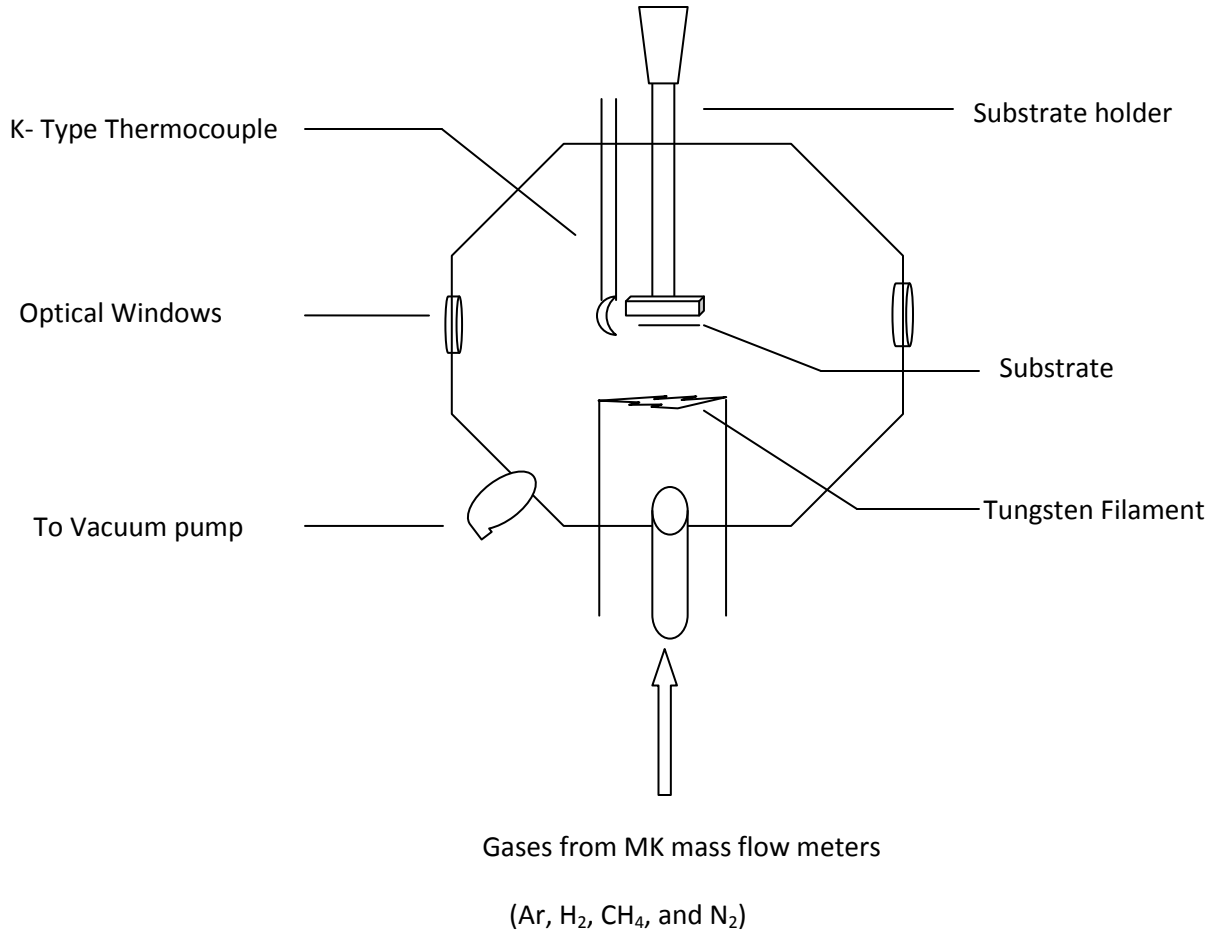


Fig 3.1: *Schematic diagram of the CVD chamber.*

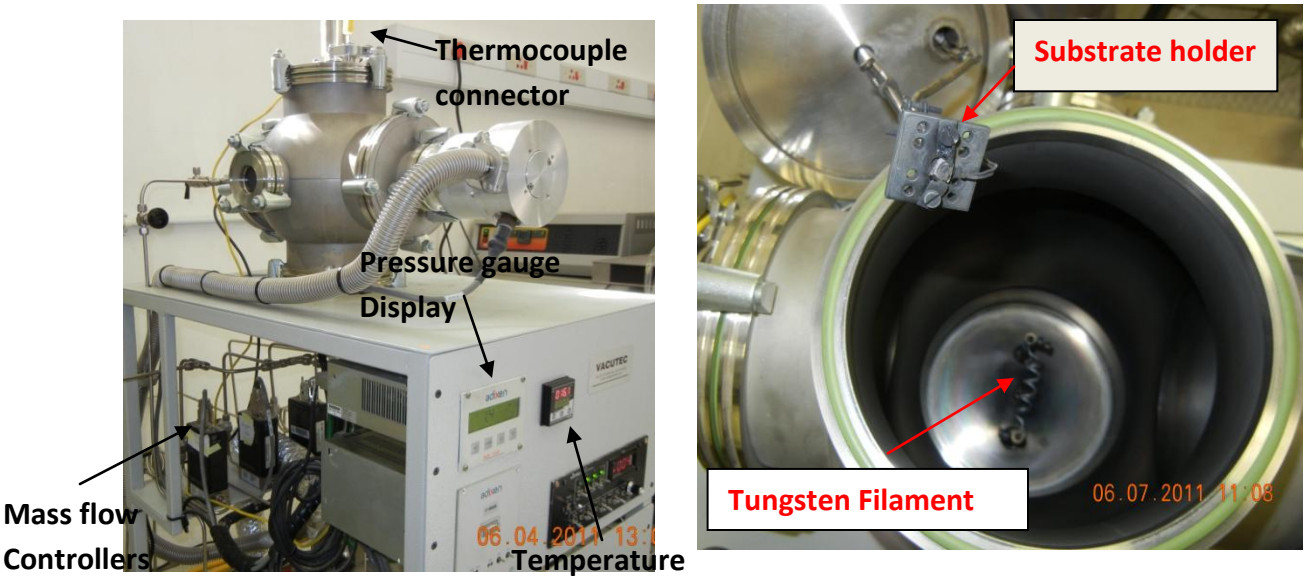


Fig 3.2: *Pictures of the actual CVD chamber which was used for the synthesis (a) Shows the front panel and (b) Top view of the CVD chamber showing inside filament and the substrate holder. The system is custom designed by S. Bhattacharyya and made by Vacutec.*

The Synthesis process of nanodiamond films using the HFCVD is a two stage process, which are namely the nucleation (seeding) and the actual growth process in the CVD.

(a) Nucleation:

It is a pretreatment of the substrate to create some nuclei from which the nanodiamond films grow. The process begins by first cleaning and etching the substrate using the procedure outlined below.

1) Firstly the substrate is degreased by an ultrasonic bath using a detergent for 5 minutes.
2) Secondly the substrate is rinsed in deionised (D.I) water for 5 minutes in an ultrasonic bath.
3) This is followed by another ultrasonic bath for 5 minutes in a 50-50 mixture of ethanol and acetone to get rid of any stubborn organic substances.
4) The substrate is rinsed in D.I. water and then dried using nitrogen gas.

5) After this the substrate is etched using (HF – HNO_3 in 1:3 ratio) acid by dipping in the solution for 60 seconds so as to reduce all oxides and expose the silicon.

After the cleaning process the substrate is finally put into diamond slurry (1 micron diamond powder in acetone) and sonicated/agitated for 60 minutes. The above pretreatment method ensures that we do not damage the substrate but instead ensures fair nucleation density.

b) Diamond growth:

As indicated above the synthesis was done using the CVD chamber shown. A tungsten wire 150 mm long and 1 mm diameter powered by a high current, low voltage DC source was used to activate the precursor gases. The high purity tungsten was wound into a coil of 7.5 mm diameter and 50 mm long. As shown in the schematic diagram Fig 3.1, the substrate holder was held 4 mm above the filament and this distance was obtained after optimization. The optimization process considered a number of variables such as the gas concentrations (Methane, Hydrogen), substrate temperature, filament temperature, the chamber pressure, the distance between the filament and the substrate, and lastly, the seeding time.

The substrate temperature was monitored using a K- type thermocouple mounted on one corner of the substrate. And the substrate itself was mounted on top of silica beads to reduce heat loses due to conduction from the stainless steel holder. The filament temperature was measured using a commercial optical pyrometer. A power dissipation of 325 W (Voltage x Current) during the reaction on the filament ensured that the temperature of the filament was approximately 2105 ^{o}C.

3.2 Electrical transport measurements

These were done using the Cryogenic free measurement (CFM) system from Cryogenic (UK) see picture below Fig 3.3 (a). The instrument is a fully computer automated system, whose program runs on Lab view. The low temperatures are achieved by the forced rapid expansion of helium gas which circulates in two closed loops. The main loop is pumped by a compressor which drives helium through two stages, the 40 K and 4 K of the cold head. The second loop is pumped by an oil free pump driving helium through a needle valve this allows the temperatures of down to 1.8 K to be achieved. Fig 3.3 (b) shows a schematic diagram of the second loop. Section 3.3 gives an outline on how the sample is mounted into the variable temperature insert (VTI) and how it is discharged.

The resistance – temperature dependence measurements were done from 2.5 K to 300 K with and without a magnetic field using a Keithly 2400 as a constant current source and a Keithly 2182A nano-voltmeter to measure the voltage across the sample. A current of 10 μA was supplied to the sample which is low enough not to cause significant heating but high enough to give high signal to noise ratio. The in-built filter of the nano-voltmeter was an added advantage that enabled good quality measurements to be made. The magneto-resistance measurements were done from 0 to 12 T at variable temperatures. The average nanodiamond film thickness was about 300 nm deposited on quartz substrates. For these measurements the van der Pauw configuration was used on a rectangular area with contacts on the four corners. See the picture Fig 3.3(iii), of the sample holder.

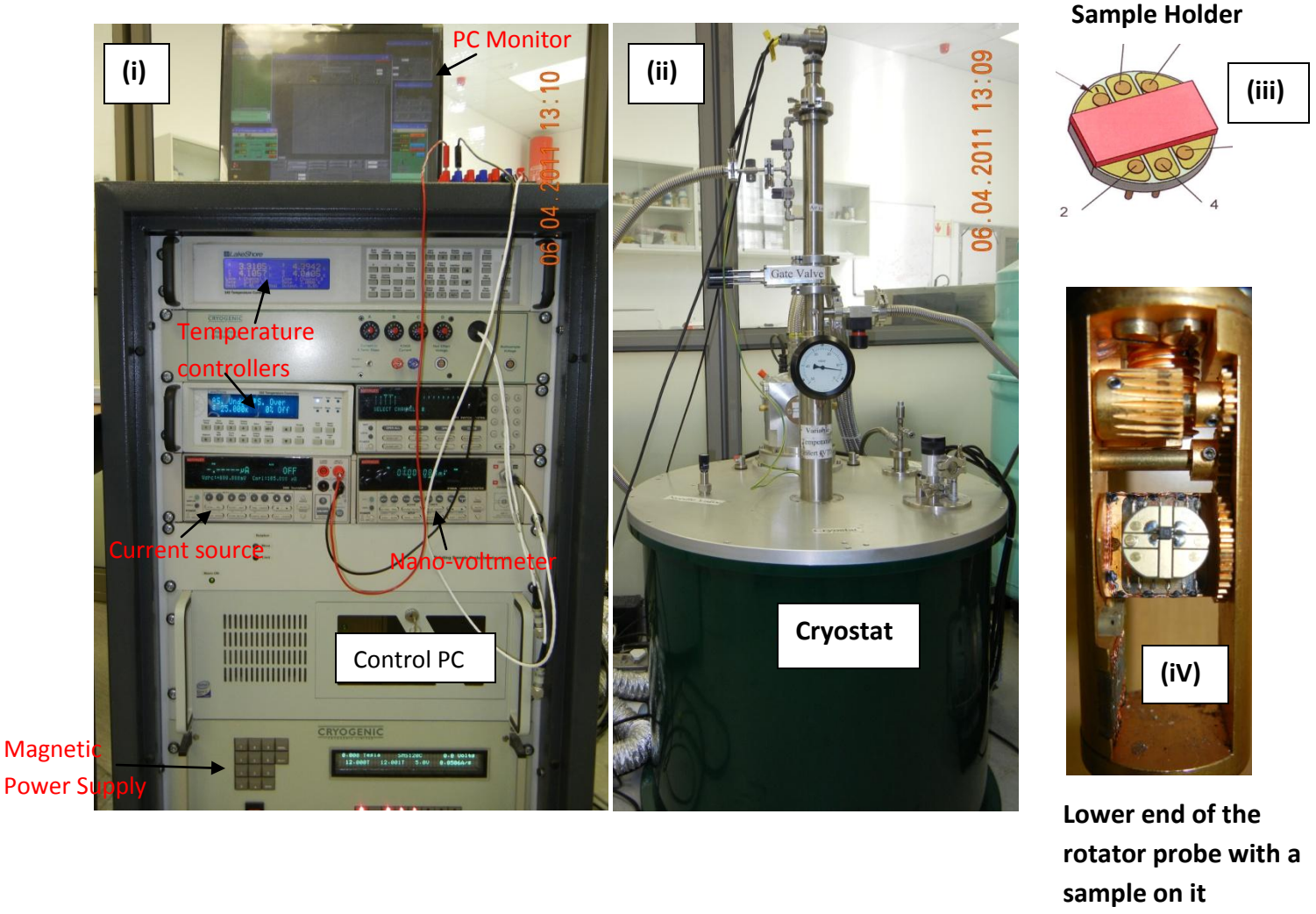


Fig 3.3: *A photograph of the cryogenic free measurement system (i) the control rack, (ii) the cryostat, (iii) the typical sample holder, (iv) the lower end of the rotator probe with a sample mounted on it.*

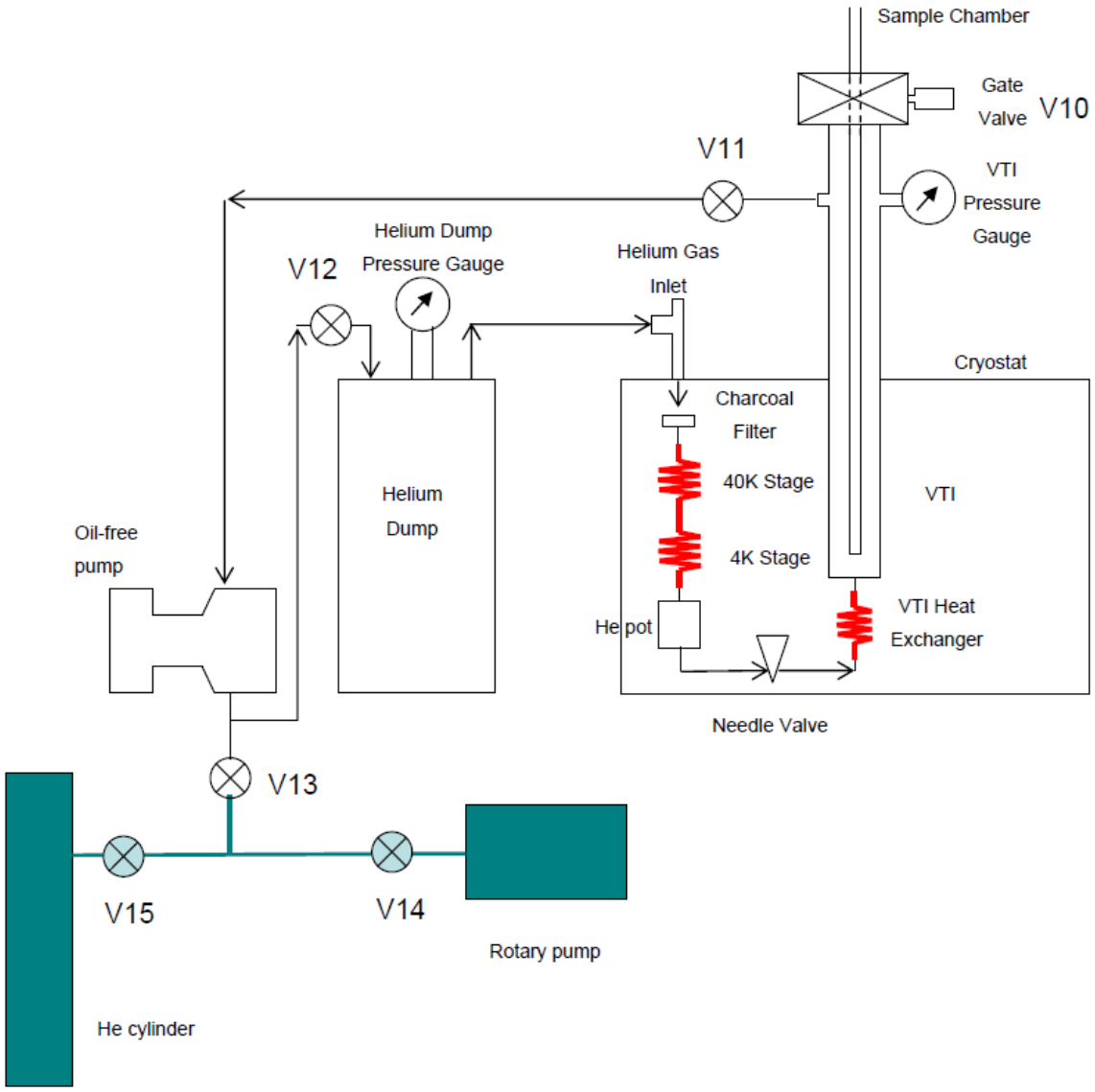


Fig 3.4: *A schematic diagram of the VTI cooling stage i.e. the second Helium loop where the sample is mounted. The Helium flow is in the direction shown by the arrows.*

3.3: Sample mounting and discharging from the VTI

Mounting the sample into the VTI

1. Place the sample to measured into the sample holder shown in Fig 3.3(iii), ensure the contacts are firm
2. Mount the sample holder on to the appropriate probe e.g. the one shown in Fig 3.3 (iv).
3. Using O-rings clamps, secure the probe on the VTI inlet and open the two valves of the airlock.
4. Turn on the rotary pump to evacuate the airlock for about 5minutes, after that flash the airlock with helium gas from the He cylinder; evacuate the airlock again for about 3 minutes.
5. Close the **bottom VTI valve**; leave the rotary pump **ON** and the top valve open. Open the gate valve and slowly lower the probe until its oil ring is onto the VTI inlet. Close this O-ring with a clamp.
6. Close the **top VTI valve** and turn **off** the rotary pump.
7. Allow the VTI temperature to cool down to base temperature and then set the sequence to be executed on the Labview virtual instrument Sequence Editor.
8. Finally press the Execute sequence button to start the measurement.

Discharging the Sample from the VTI

1. Stop the sequence by pressing the Terminate sequence button.
2. Open the **top VTI valve** and turn **ON** the rotary pump, keep the **bottom** valve **closed**.
3. Slowly lift the probe until the sample is **above** the gate valve and then **close the gate valve**.
4. Close the **top VTI valve** and turn **off** rotary pump.
5. Allow the sample to warm up to room temperature with **both** VTI valves **closed**.
6. Finally the sample can be removed after venting the airlock.

N.B. The Gate valve and the Bottom VTI valve should never be open at the same time otherwise air will rush into the VTI, freeze and block the system.

3.4: Sample preparation for TEM

The preparation of samples for TEM is a rigorous process that requires great precision and accuracy. We briefly give a short outline of how it was done. The substrate was first grinded to about 180 microns which is then followed by dimpling it a further 80 microns. The substrate is then polished and this would deepen the dimple by another approximately 5 microns. Finally the substrate is ion milled using dual 5 kV ion guns for 30 minutes so as to leave about 10 microns to the film.

Chapter 4

Results and Discussions

4.1 Effect of substrate pretreatment

As indicated in chapter three, the synthesis of nanodiamond films is a two stage process and the first stage is the pretreatment (seeding) of the substrate. During this research, this parameter was investigated as a function of both time and the concentration of the diamond powder slurry. The SEM images below show the different nanodiamond films which were synthesized after different pretreatment methods.

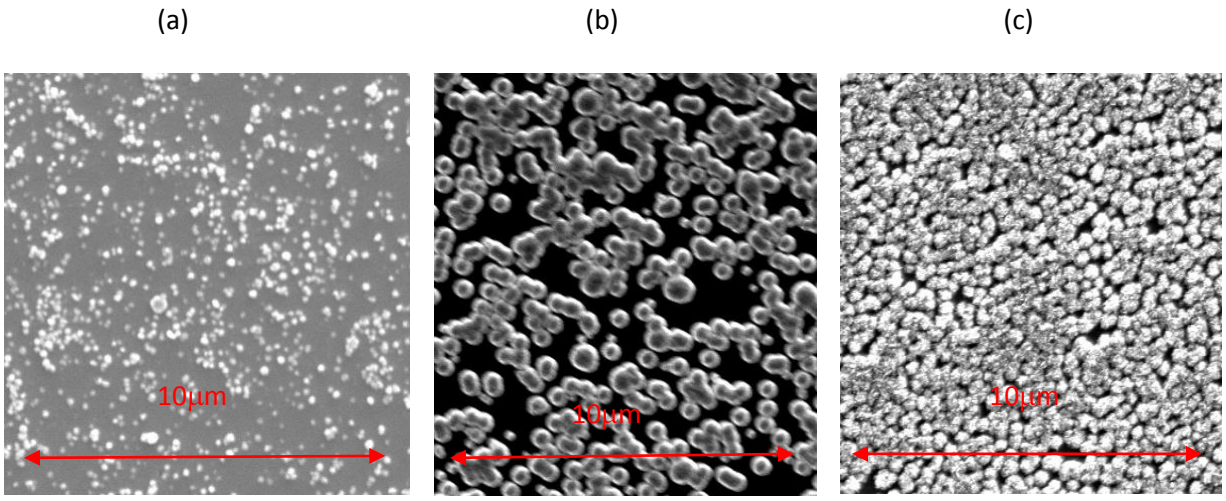


Fig 4.1: *SEM micrographs of nanodiamond films which were pretreated differently. (a) The substrate was sonicated for 15 minutes with 0.2 mg/cm^3 of diamond slurry. (b) The substrate was sonicated for 30 minutes with 0.4 mg/cm^3. (c) Substrate sonicated for 60 minutes with 0.4 mg/cm^3.*

The figure above shows us that the best seeding was obtained after sonicating for one hour with a concentration of 0.4 mg/cm^3 of the diamond powder in acetone. For our research purpose this kind of seeding is sufficient.

After achieving the kind of seeding shown in the last image in Fig 4.1 (c) we were thus able to start nitrogen incorporation with the aim of improving the conductivity of the films. The "undoped" films were found to be very insulating and thus could not be measured to investigate their electrical properties. Below are some AFM images of other films with excellent seeding.

(a) (b)

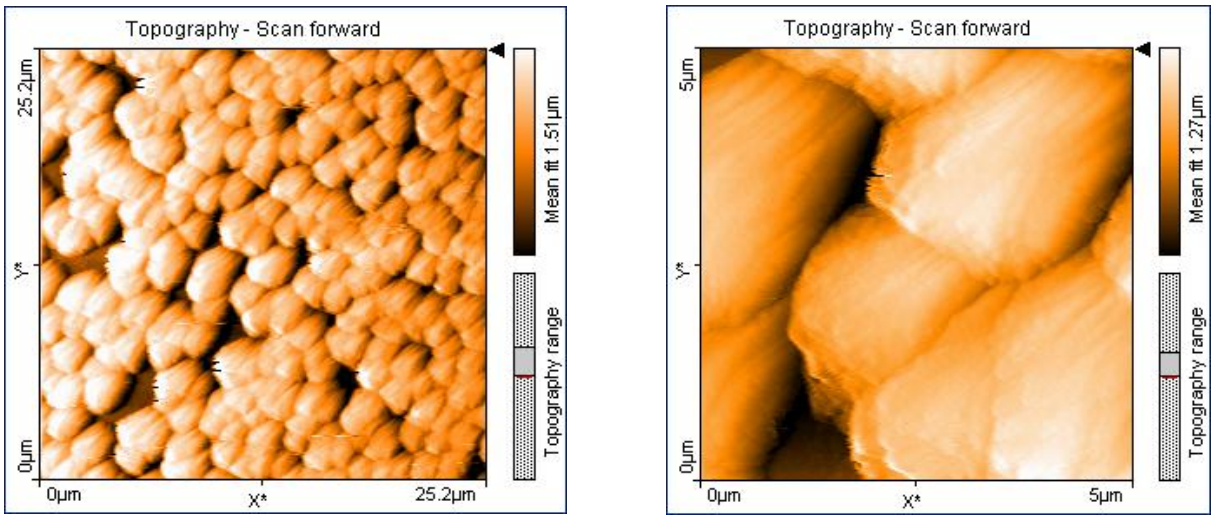


Fig 4.2: *Low and high magnification - AFM images of films prepared at pressure of 74 mbar and substrate temperature of 850^{o}C showing the microstructure.*

The AFM images above (Fig 4.2) provide us with extra information besides the good seeding. A closer look at the high magnification images shows us columnar elongated structures in the nanodiamond clusters which suggest a columnar growth mechanism from the base of the substrate upwards. It is also evident we have grain boundaries (GB) with different widths and this introduces some complexicity when we try to understand the contribution of these GBs in the electronic properties of the films. The images also show us that the nanodiamond films are made of crystal clusters of varying shapes with sharp grain edges. This is clearly shown in the SEM image below Fig 4.3.

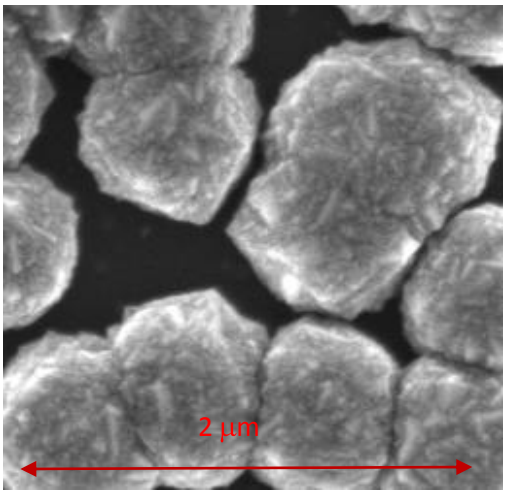


***Fig 4.3**: SEM micrograph showing sharp grain edges of nanodiamond films prepared at a pressure of 74 mbar and a substrate temperature of 850°C.*

(a) (b)

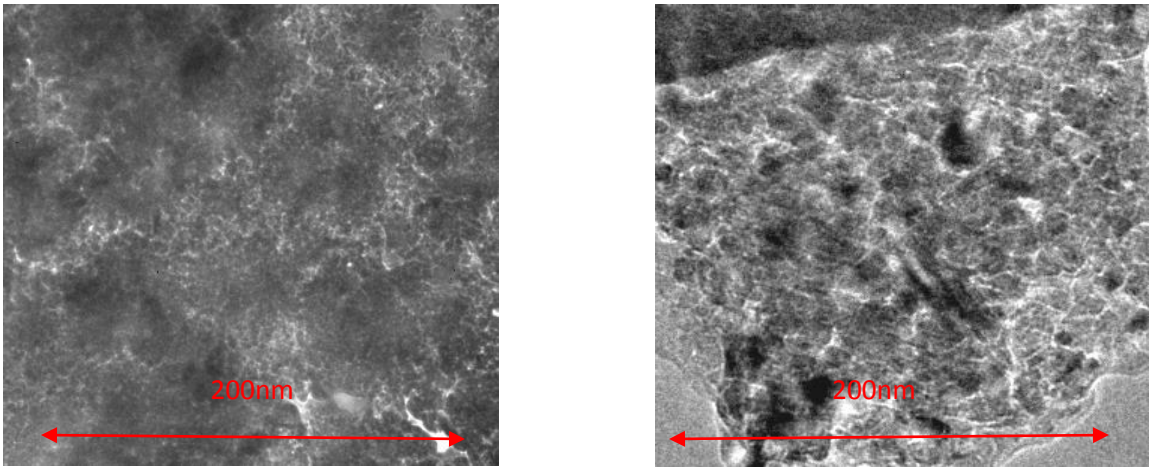


***Fig 4.4**: TEM micrograph of films prepared at a substrate temperature of 750°C (a) is a thicker film (b) is a thinner film.*

From the TEM images one outstanding fact is the continuity of the grain boundaries, and as indicated earlier, the widths of these GBs vary. This is the biggest challenge for these films in electronic applications. We are unable at present to determine the crystal size of our films because this requires high resolution TEM. We will now turn our focus to the optimization of various parameters during the synthesis.

4.2 Optimization of the synthesis process

a) Effect of substrate temperature on the quality of nanodiamond films.

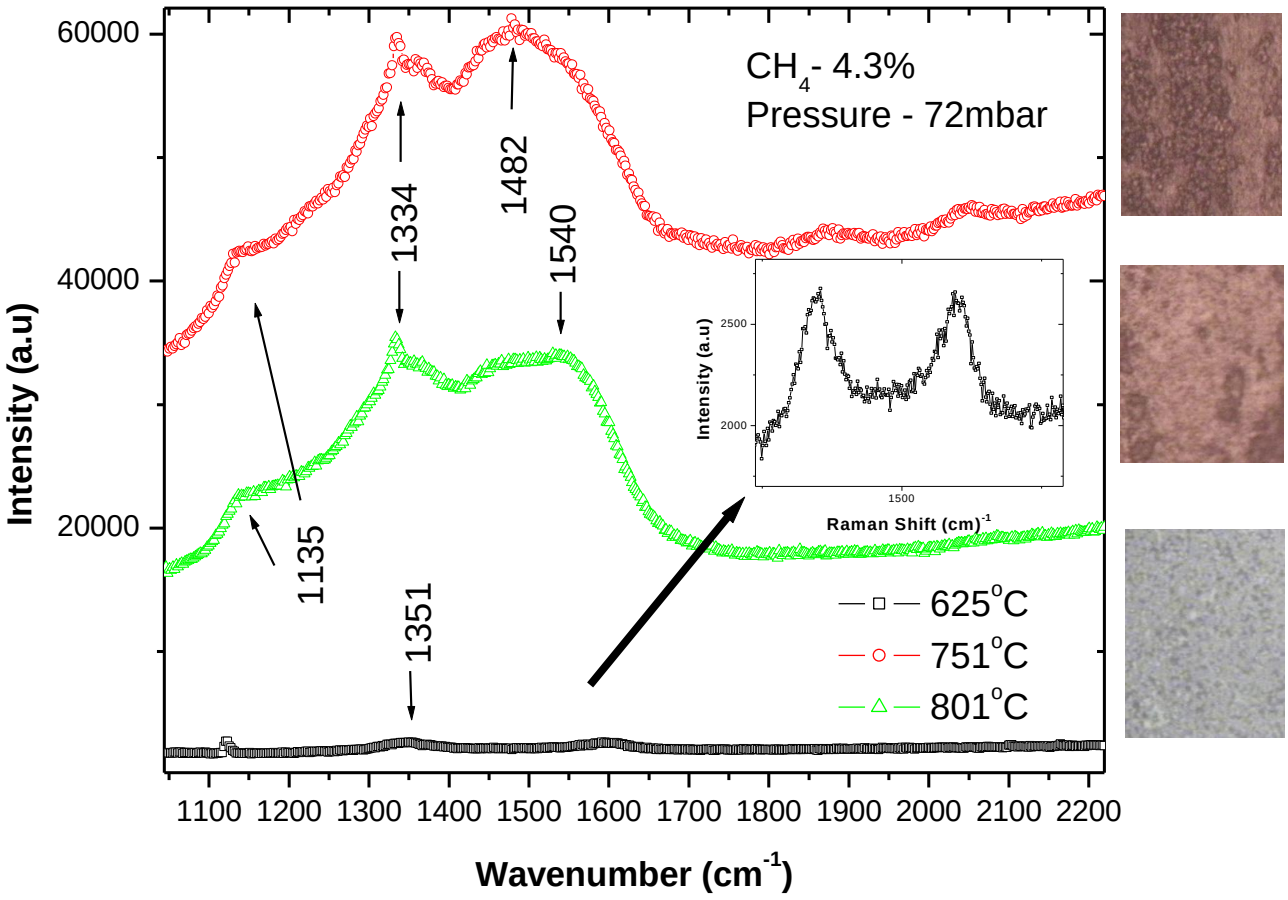


Fig 4.5: *Raman spectra for three samples deposited at different temperatures, the pictures on the right outside the graph, are the optical images from where the spectra were obtained. The bold arrow points at the insert of the magnified black spectrum.*

From the above (Fig 4.5) Raman spectra it can be seen that to deposit nanodiamond films using the described setup a minimum substrate temperature above 625 ^{o}C is required. The samples prepared at or below this minimum have very broad D and G bands with no clear crystalline diamond peak (see insert of Fig 4.5) indicating disordered and graphitic carbon deposition. Increasing the substrate temperature to 800 ^{o}C favors the deposition of better phase pure diamond films as indicated by a less pronounced and broad G band for the sample prepared at

this temperature (triangles- spectrum). The relative intensity of G band to the crystalline diamond in 750 ^{o}C sample is significant when compared to 800 ^{o}C samples, implying more graphitic phases in the grain boundaries.

In addition to that we also observe a pronounced 1482 cm^{-1} peak in the 750 ^{o}C films. This peak has been debatably assigned as the second order peak of trans-polyacetylene with the first order at 1135 cm^{-1}. Whether it is trans-polyacetylene or not, the important fact to note here is that it is due to an sp^2 phase and these two peaks have been taken as a signature of UNCD [**25**]. At higher temperature these peaks are less pronounced suggesting that, higher temperature favors decomposition of sp^2 phases but the sp^3 phase is more stable. Another possible reason could be that the morphologies of the two films are different which would result in different grain boundaries and hence different relative amounts of sp^2 phases. This is supported by the SEM images (see fig 4.6) which show slightly bigger grain sizes for the 800 ^{o}C films. The SEM image for the 750 ^{o}C films shows bigger spaces between clusters which might have more sp^2 phases.

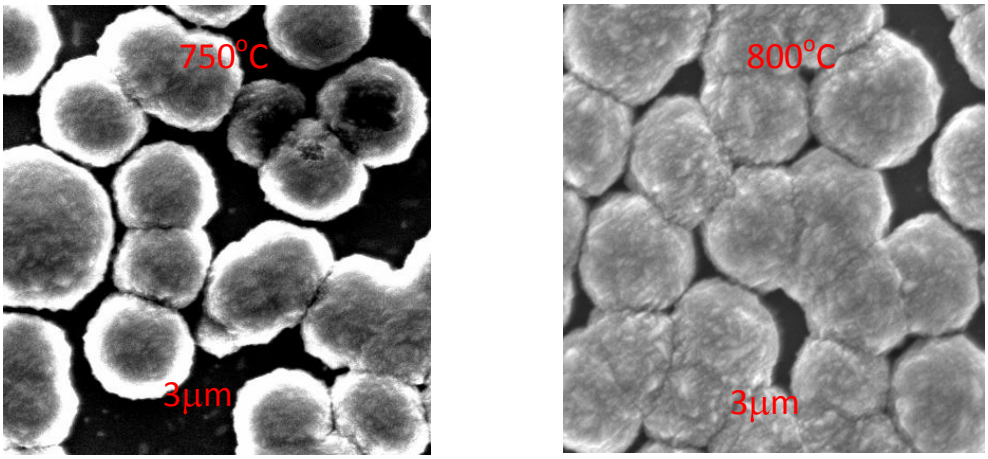


Fig 4.6: *SEM micrographs of the 750^{o}C and 800^{o}C films showing the differences in cluster sizes.*

From the SEM analysis, and comparing the film thickness it was observed that higher temperature promotes the growth rate. The films grown at 800 ^{o}C are thicker than those

prepared at 750 ^{o}C with a thickness of approximately 357 nm which implies a growth rate of 86.8 nm/ hour. On the other hand, the 750 ^{o}C films have a thickness of approximately 243.5 nm which gives a growth rate of 60.8 nm/hour since the films were all grown for four hours. These measurements were done by scanning the samples at the boundary edge between the deposited area and non deposited area where the samples were held by the holder. This might not be surprising because a higher temperature would mean more reactive radicals close to the deposition surface and hence a better growth rate.

b) Effect of pressure on the quality of nanodiamond films.

Another important parameter to consider in nanodiamond synthesis is the effect of pressure. It affects the film morphology because it determines the amount and type of reacting species around the deposition area. From the literature it is known that lower pressure favors smaller nanodiamond grains, which is attributed to secondary nucleation processes and a faster growth rate [**35**]. Contrary to theoretical predictions, high pressure has been found to increase the hydrogen radicals near the deposition area resulting in more etching away of sp^2 phase and hence the formation of microcrystalline diamond [**36**]. The Raman spectra below show the results obtained for samples prepared at 754 ^{o}C with 3.9% methane but different pressure. Some reports have also reported a transition from MCD to NCD as the pressure is decreased [**35**].

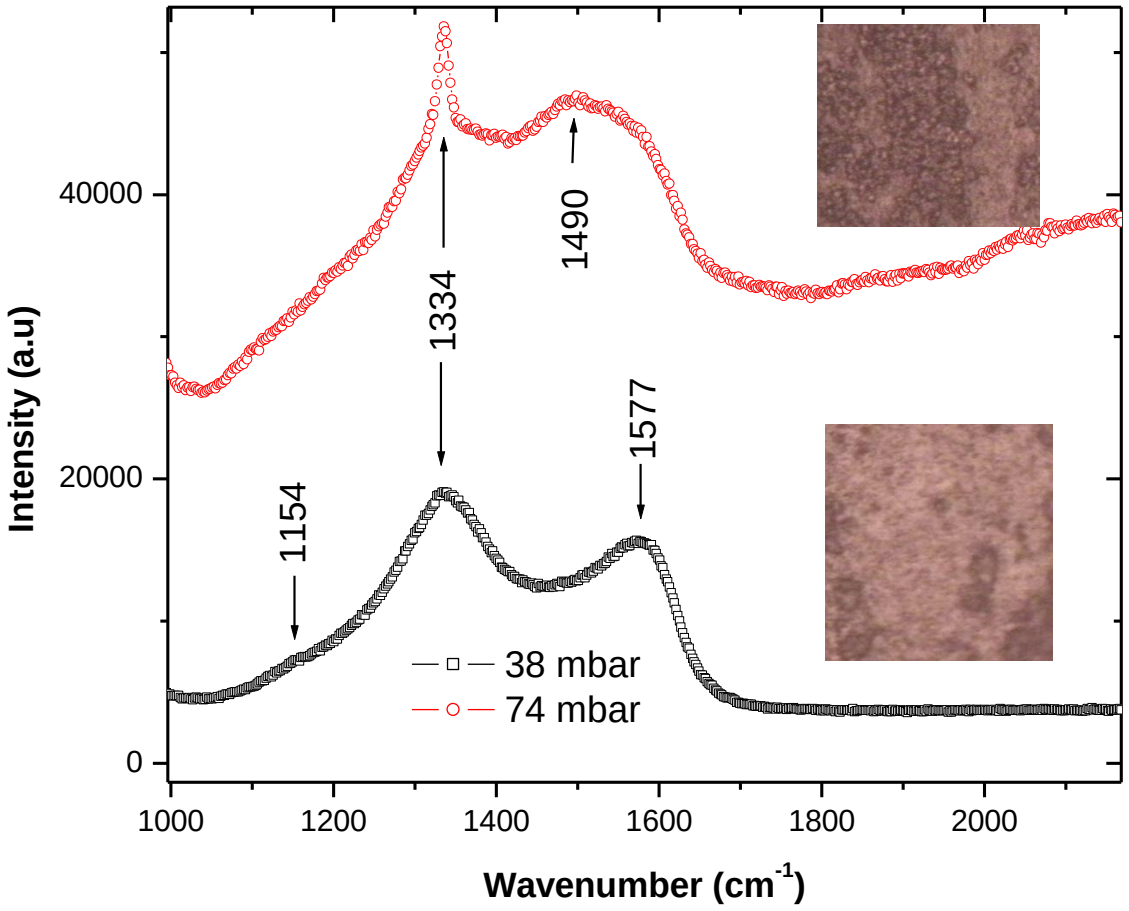


Fig 4.7: *Raman spectra of nanodiamond films showing the effect of pressure, the insert pictures are the corresponding optical images.*

A look at the spectra reveals that the sample prepared at higher pressure has a strong diamond peak, which might be an indication of a stronger microcrystallinity. This supports reports by other researchers as alluded to earlier [**35**]. High pressure is also known to introduce more defects in the film however we could not confirm this report because this argument is based on the 1488 cm^{-1} Raman band which is not an sp^3 phase [**36**].

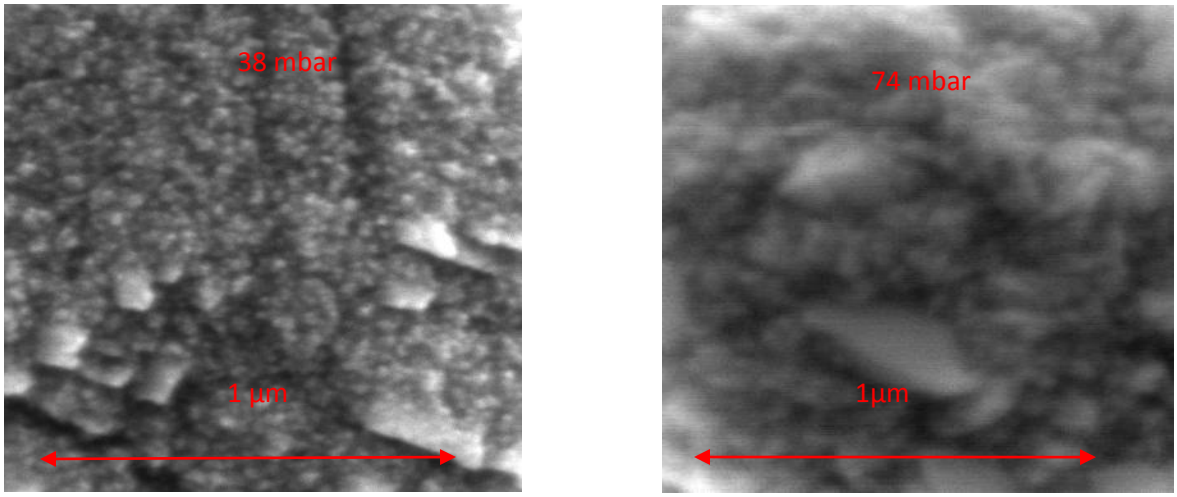


Fig 4.8: *SEM micrographs showing the effect of pressure on the grain sizes.*

From the SEM images above (Fig 4.8) we can see that the nanodiamond films prepared at lower pressure show smaller diamond grain sizes compared to those at higher pressure. This probably explains why the diamond signal is stronger for the film prepared at higher pressure. A simple possible explanation for the difference in morphology is that higher pressure tends to keep the reacting radicals near the deposition surface and this will enhance faster growth resulting in bigger diamond grains.

c) Effect of filament- substrate distance on the film quality.

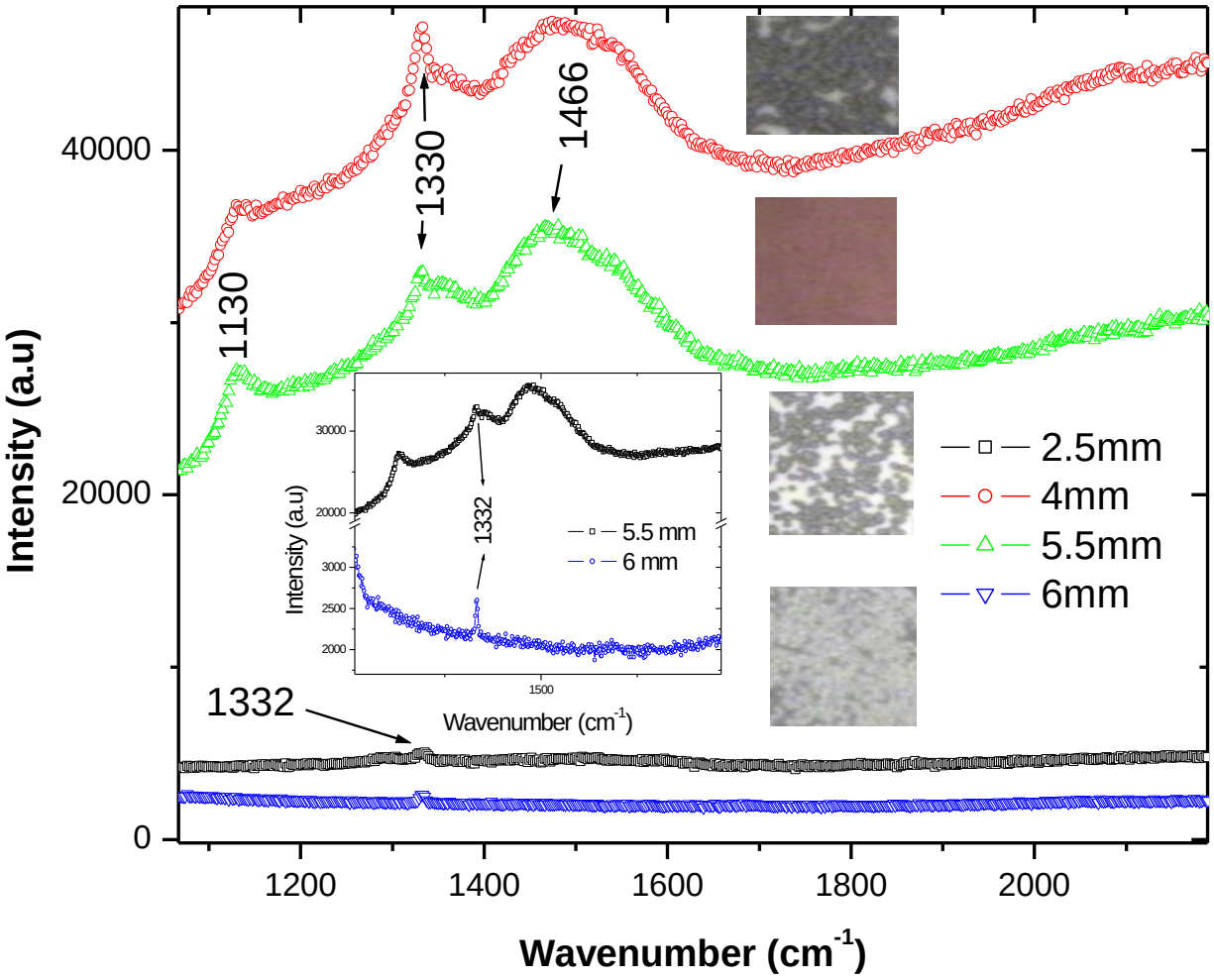


Fig 4.9: *Raman spectra of nanodiamond films to show the effect of filament distance from the substrate. The insert pictures show the corresponding optical images and the magnified bottom two spectra.*

The Raman spectra on the above (Fig 4.9) clearly shows that too close or too far away from the filament results in very little or no deposition. As indicated by the black and blue spectra, it is evident that these two have very weak diamond peaks at 1332 cm^{-1} and the D and G bands are also so weak that they can hardly be noticed.

From a closer inspection of the spectra for 4 mm and 5.5 mm films, it is clearly seen that the 4 mm films have better phase pure diamond compared to the 5.5 mm films. This is indicated by the relative ratios of the diamond peak to the G band which are the 1330 cm^{-1} peak and 1547cm^{-1} respectively. Both samples indicate very close similar, pronounced peaks at 1130 cm^{-1} and 1466 cm^{-1}. This might be an indication of the uniformity of the conditions under which they were prepared with the only difference being the filament distance. Such reproducibility in a CVD system is highly desirable. The explanation for the observed result is that as the distance from the filament is increased, the number of diamond reactive radicals varies. Too close to the filament we have a low concentration of the essential radicals necessary for diamond growth because of the high temperature which is close to filament temperature. The same can be said when the distance is greater. As highlighted in the literature review, diamond deposition is very sensitive to relative ratios of the reactive radicals such as $–CH_3$, -H and $-C_x$. The relative percentages of these vary greatly with distance from the filament according to their thermal stabilities. Detailed studies of the relative amounts of these radicals can be done using in situ absorption spectroscopy which was not available during our research.

We further observed that the diamond peaks appeared at 1330 cm^{-1} on the 4 mm and 5.5 mm samples. While on the 2.5 mm and 6 mm samples the diamond peak is at 1333 cm^{-1}. The explanation for this at present is not understood. It can however be concluded that for this experimental setup the optimum filament distance from the substrate is 4 mm (4×10^{-3}m). This is only possible provided the filament dimensions are as specified in chapter 3 on the experimental set-up of the CVD i.e. a diameter of 7.5 mm and 50 mm in length.

c) The effect of methane concentration on the film quality.

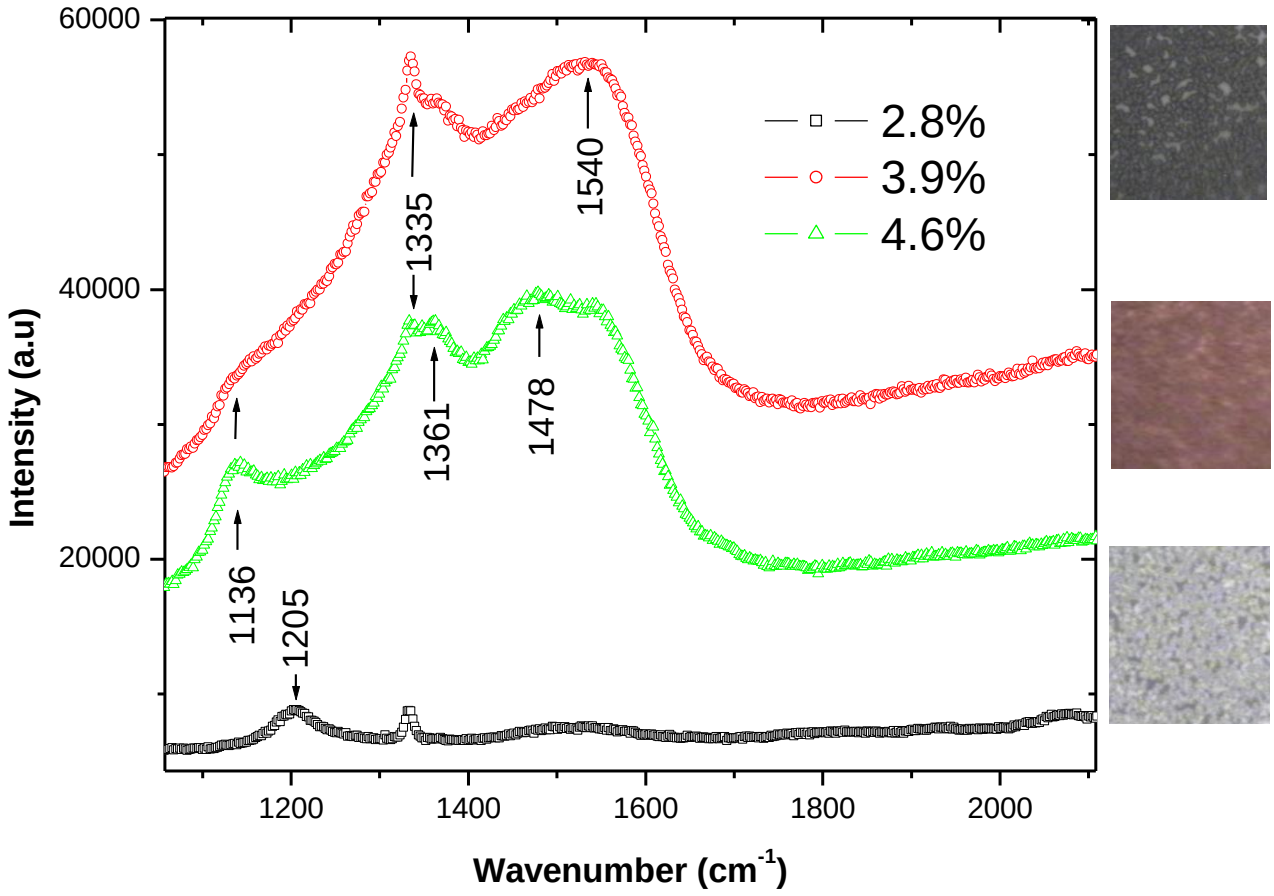


Fig 4.10: *Raman spectra of nanodiamond films showing the effect of methane concentration. It also shows the corresponding optical images which are outside the graph.*

Some interesting results were observed here as indicated by the Raman spectra Fig 4.10. It should be pointed out before we discuss the results that nanodiamond deposition has a narrow range of conditions under which it can be deposited (see Fig 2.6). This is because in low pressure CVD, diamond is deposited under non equilibrium conditions, while graphite is stable under equilibrium conditions. Rapid cooling of the system and the fact that at high pressure diamond is more stable than graphite ensures that we prevent the breakdown of our films into graphite after the synthesis.

The non-equilibrium synthesis of nanodiamond films poses a great challenge to set these conditions as all systems try to attain equilibrium. Confined by the limitations of our mass flow meters e.g. the methane MKF is not sensitive at flow rates less than 7 sccm and the maximum for the argon MKF is 200 sccm. We could not have less than 2.8% methane. Higher concentrations, greater than 5.5%, resulted in soot being deposited. From the spectra above it is quite evident that less methane in the chamber promotes the growth of better nanodiamond films. As shown from the low overall intensity of the black spectrum, this quality comes with a price of very low growth rate. There is also an unidentified peak so far, at 1205 cm^{-1} for this black spectrum. The 3.9% sample has the highest intensity with sharp diamond and G band peaks, indicating an improvement on the growth rate with a better diamond quality. The sample prepared with 4.6% methane in gas has the worst quality compared to the other two nanodiamond films and this is supported by the suppressed diamond peak and a more pronounced 1478 cm^{-1} peak, 1361 cm^{-1}(D band) and the 1136 cm^{-1} which are due to sp^2 phases most probably in located in the grain boundaries.

One of the most important facts that can be obtained from these results is that the methane percentage radically changes the ratio of the sp^3 and sp^2 phases in a big way. As can be seen from the results, when we have 2.8% methane, the G band is very broad and the D band is almost non-existent implying the absence of ring sp^2 phases. Increasing the methane concentration brings both rings and chains in the sp^2 phase as indicated by presence of both the D and G band peaks. Further increase of methane begins to suppress the crystalline diamond peak meaning a significant change in the sp^3 to sp^2 ratio.

Since electron transport in diamond films is believed to be affected greatly by the grain boundary phase purity, it can be suggested that that the above samples would have different transport mechanisms, if they were doped. If this is true, it therefore means that the methane concentration has to be accurately controlled to ensure uniformity of the films. The conclusion from this is that the best compromise methane percentage will be 3.9% which has better quality diamond with a significant growth rate.

e) Effect of hydrogen concentration on the film quality.

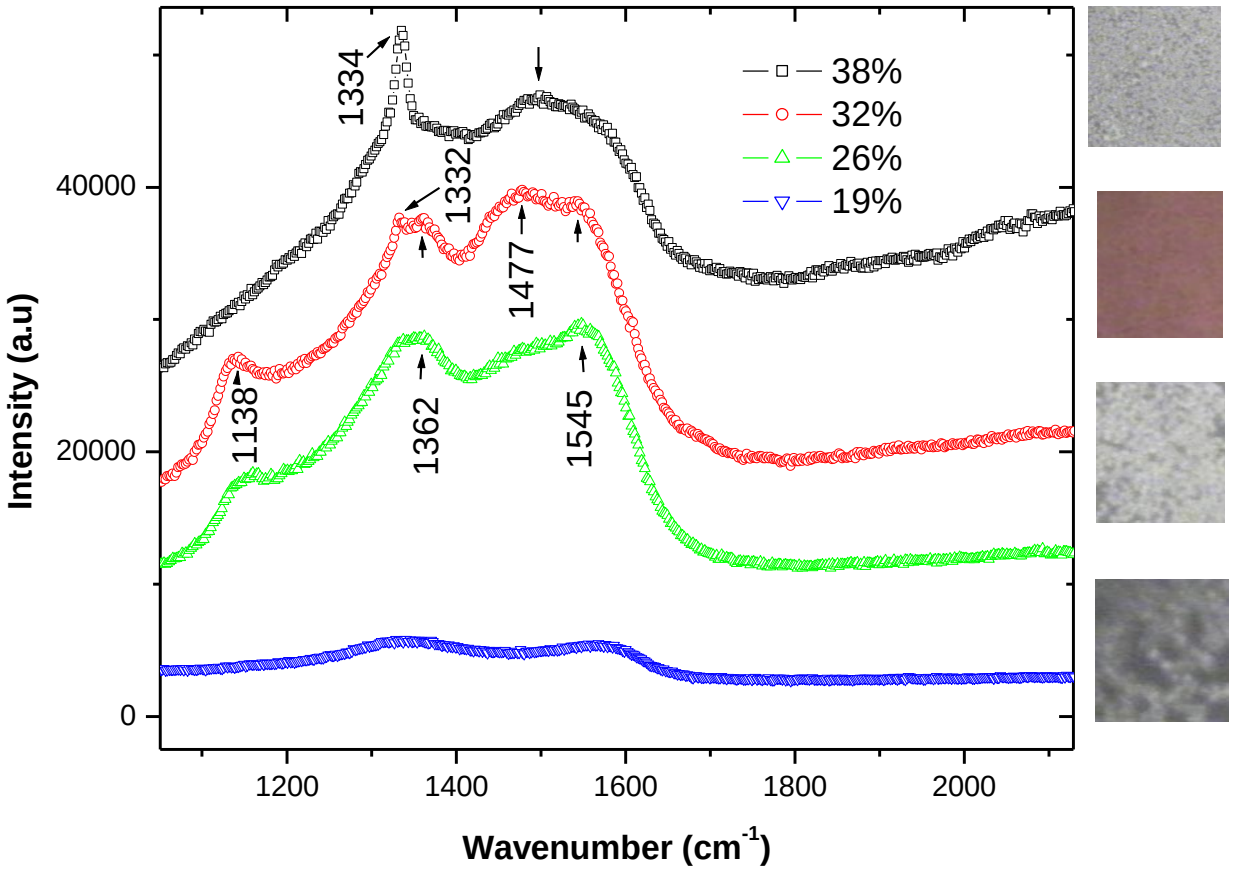


Fig 4.11: *Raman spectra of nanodiamond films showing the effect of hydrogen concentration and the corresponding optical images are outside the graph.*

The above Raman spectra, Fig 4.11, clearly show how hydrogen concentration affects the diamond film quality. The trend is clear and simple; more hydrogen improves the quality of the films as indicated by the results above (squares- spectrum), which has a sharp and more pronounced diamond peak which is clearly higher than the G band peak. As the amount of hydrogen is reduced, the diamond peak becomes reduced and broad indicating an increase in the sp^2 phase. It would therefore mean that hydrogen reduces the amount of sp^2 phases as suggested by other researchers [**22**]. As indicated from the results we can also see that when

there was 38% hydrogen, the 1138 cm^{-1} peak was greatly suppressed. If this is taken as a signature of UNCD, it would imply that increased hydrogen radically changes the diamond morphology. In this case it would mean that we have either NCD or MCD diamond by increasing the hydrogen concentration.

f) Effect of substrate type on the quality of nanodiamond films.

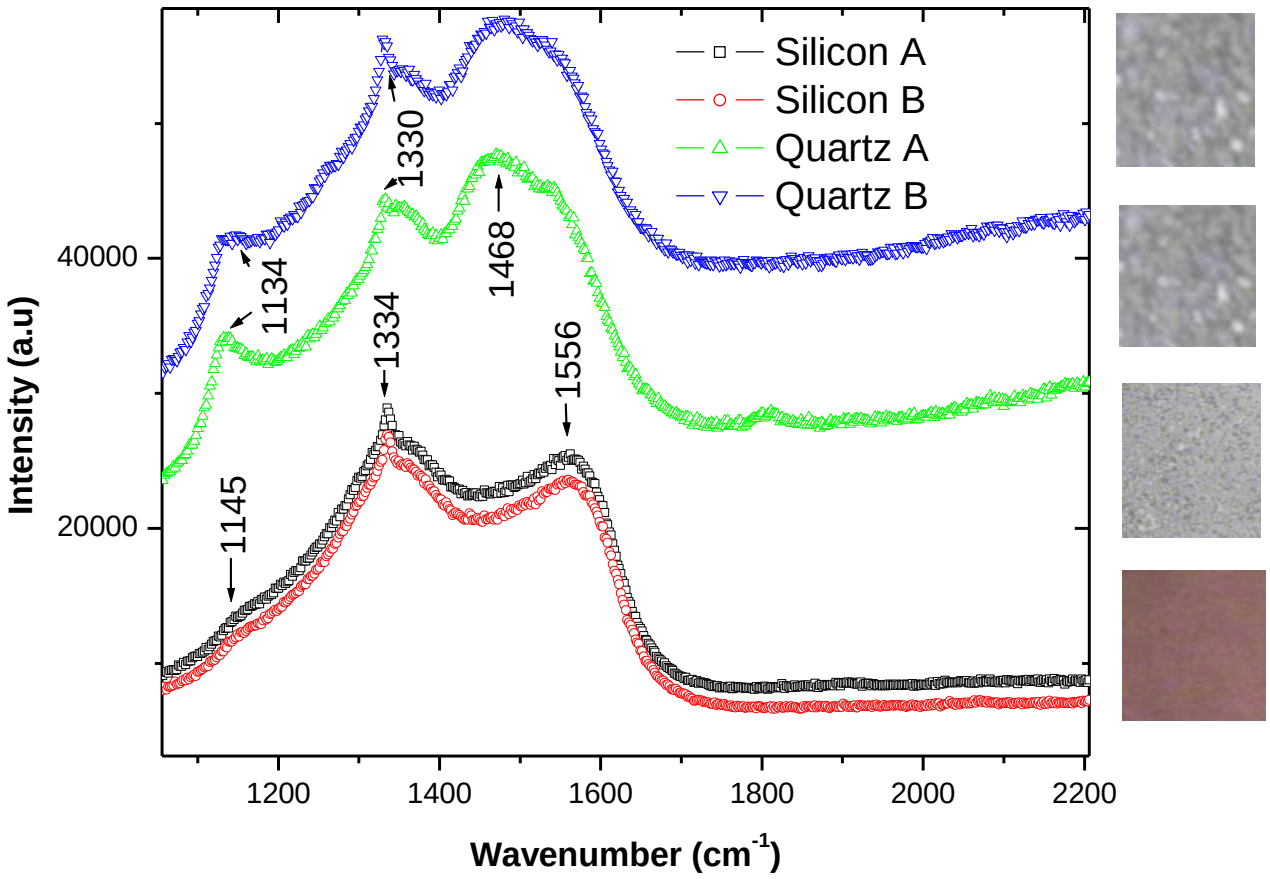


Fig 4.12: *Raman spectra of nanodiamond films showing the effect of substrate type and the corresponding optical images are outside the graph.*

From a non-scientific point of view, one would not expect a difference in the diamond film quality if we change the substrate type. The simple, logical thinking would be that, if the conditions are the same, then the film quality must follow suit.
This kind of thinking however is not correct. As indicated in chapter two, the diffusion coefficient of the material on which the deposition is done is an important factor in determining both the growth rate and film morphology.

The results Fig 4.12 indicates that the films deposited on silicon have better phase purity compared to those on quartz. This is not surprising because the diffusion coefficient of carbon onto silicon is higher than it is on quartz (ß- SiO_2). The early stages of diamond formation begin by the formation of a SiC layer; therefore for quartz this process is not as rapid as it is in silicon. We thus observe more sp^2 phases in the samples prepared on quartz than those prepared on silicon.

g) Effect of nitrogen incorporation in the reaction chamber on film quality.

One of the main objectives of this project was to improve the conductivity of nanodiamond films. This was done by synthesizing the films with some percentage of nitrogen gas in the plasma. From hence forth we shall refer to the films prepared with 10% nitrogen in the gas as the 10% doped films. The same shall be said for the 20% and 22% films. However we point out that this does not necessarily mean we have 10%, 20% or 22% nitrogen in the nanodiamond film. It is important though to mention that the relative change in the nitrogen percentage in chamber is proportional to the atomic percentage in the films at lower percentages. At higher percentages of nitrogen in the chamber the atomic percentage in the films saturates (see Fig 1.1). All we are interested in at present is to see relative change of electrical properties of nanodiamond films for different nitrogen percentages in the chamber.

The HFCVD films synthesized with less than 20% nitrogen in the chamber were highly resistive and hence could not be measured; the 20% films (20% HFCVD-N_2) are highly resistive at very

low temperatures making the measurement difficult at these temperatures. However the 22% HFCVD-N_2 and microwave (10% and 20% MWCVD) synthesized films are all conductive, demonstrating the effect of more nitrogen in the films. The challenge in nitrogen incorporation using HFCVD is to efficiently dissociate the nitrogen gas so that it can take part in the reaction with other diamond forming species. The nitrogen heat of dissociation is approximately 8.8 Volts (849.35 KJ), on heated tungsten filament this is reduced to almost half depending on the pressure of the chamber. Nevertheless this still is a lot of energy and this explains why more nitrogen is required in the chamber than it is for the MWCVD [**37**, **38**].

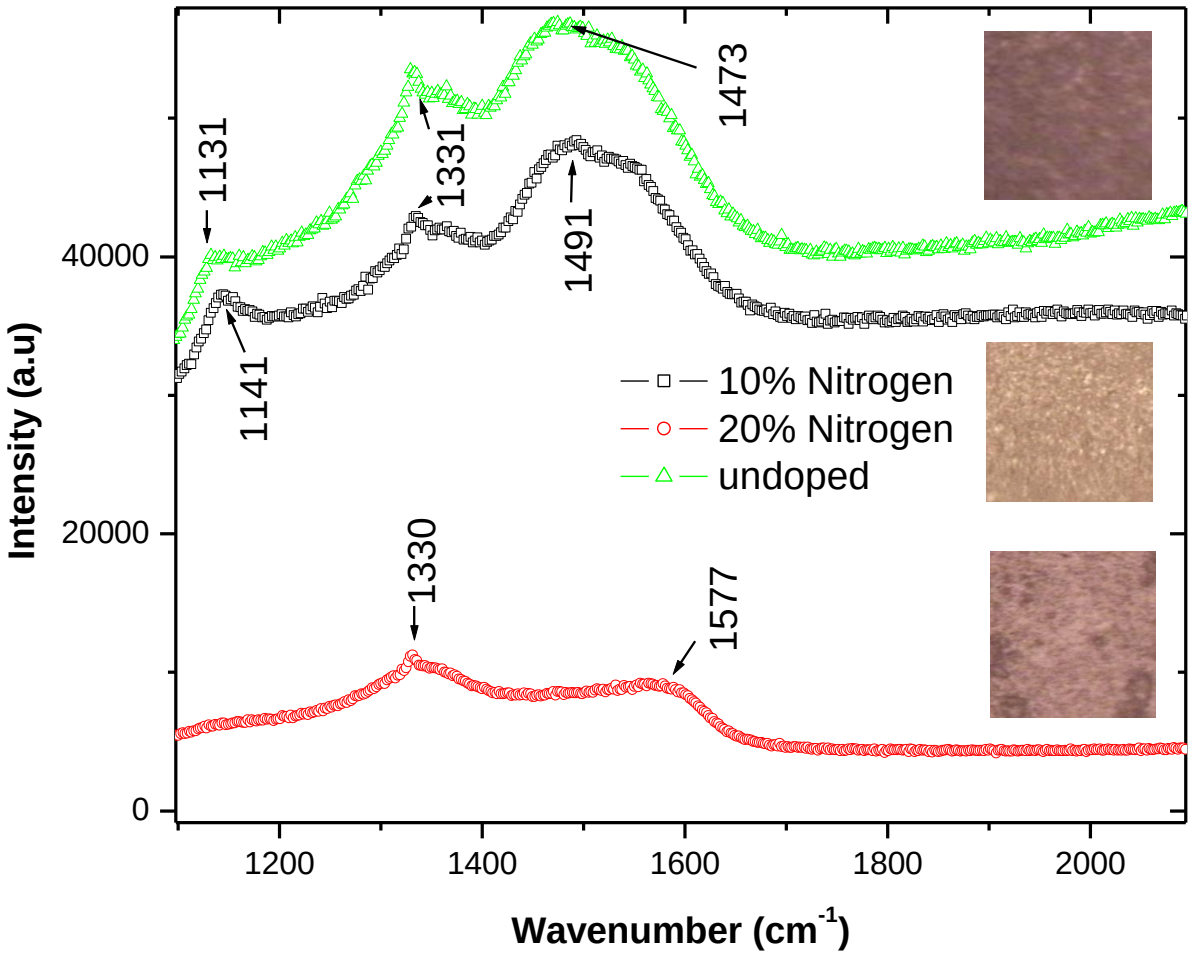


***Fig 4.13**: Raman spectra for nitrogen doped and undoped films prepared using the HFCVD method.*

The spectra above Fig 4.13, do not give any clear differences between doped and undoped films. We however can notice a small drift of the diamond peak for the film prepared with 20% nitrogen in the atmosphere which might be due stresses introduced by nitrogen defects. In addition to that there is a pronounced G band and the 1131/41 cm^{-1} peak of trans-polyacetylene for both the non conducting film (10%) and the undoped film. This is not the case for the conducting films which have very broad sp^2 band phases. From this kind of spectrum it is logical to conclude that in the nitrogen doped films we have more of disordered carbon phases or diamond like carbon. This implies a different transport mechanism in these films to that of graphitic materials.

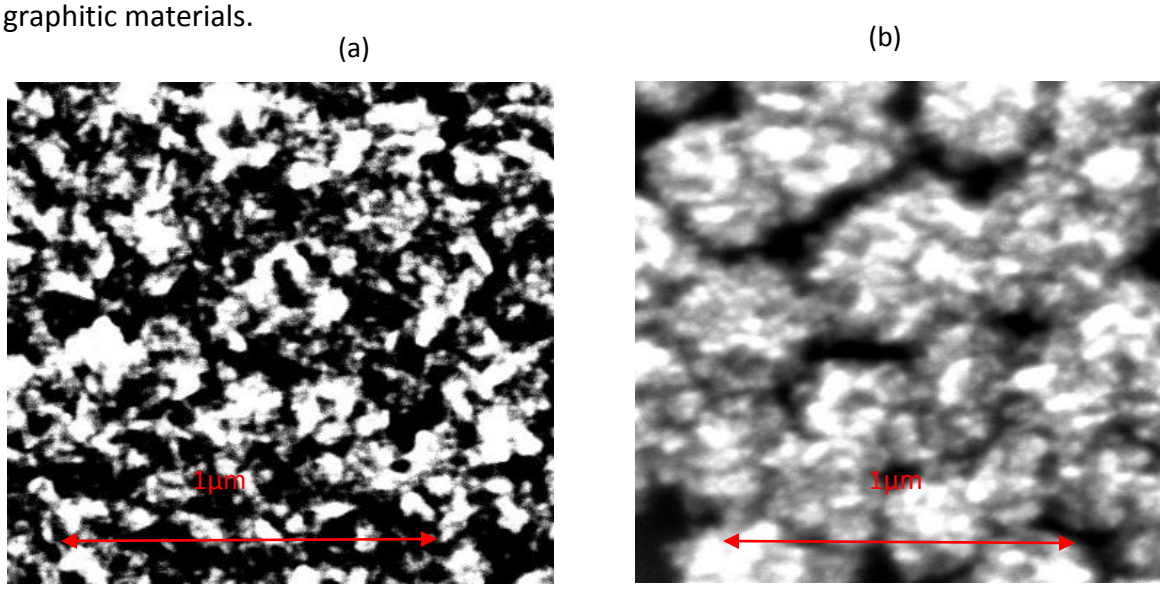


Fig 4.14: *High magnification SEM micrographs of nitrogen doped films prepared with different methane concentration but the same temperature and pressure. (a) CH_4- 4.2% (b) CH_4 – 3.1%.*

The micrographs Fig 4.14 clearly show a change in the crystallinity of the nanodiamond films with the introduction of nitrogen. The clusters become fragmented and smaller taking non uniform and irregular shapes. More methane in the chamber produces smaller clusters as compared to having less methane this is most probably due to the fact that we have more C_2 dimers in the chamber and this is known to enhance renucleation, thus the growth of larger grains is inhibited [**23**].

4.3 Synthesis of doped and undoped nanodiamond films - Conclusion

As we end this chapter on the synthesis, we would like to reflect on the main observations made this far. Efficient and uniform deposition of nanodiamond films requires an effective seeding process and we have shown that ultrasound sonication with 0.4mg/cm^{-3} of diamond slurry for 60 minutes is adequate to achieve good seeding. This is however subject to proper cleaning of the substrate.

For our CVD chamber, whose volume is approximately 9 900 cm^3 we have observed that with 5 cm long single filament at the centre of the chamber a minimum substrate temperature of 625^{o}C is required to achieve significant nanodiamond deposition. The optimum filament to substrate distance is 4 mm. This is definitely applicable when the filament diameter is 1 mm and has been wound into a coil of 7.5 mm in diameter.

The growth rate of the films has been observed to be dependent on the substrate temperature (T_s). High temperature favors high growth rate with a maximum growth rate of approximately 0.204 μm/h achieved at 825 ^{o}C. This is in the case of the undoped films; introduction of nitrogen lowers the growth rate as the nitrogen takes away some reactive carbon radicals forming CN_x compounds and this also reduces the probability of renucleation. A columnar growth mechanism was shown by some of our AFM images.

Further to the above observations we have noted that high pressure favors the formation of microcrystalline films, which was evidenced by the Raman and SEM micrographs. We attributed this to the increased hydrogen radicals near the deposition surface which enhances the etching away of sp^2 phases. TEM micrographs showed continuous grain boundaries of different widths which would possibly result in different transport properties.

Lastly, we also observed that the methane and hydrogen concentrations significantly affect the film morphology. A high percentage of hydrogen reduced the sp^2/sp^3 ratio. While increasing the methane concentration did the opposite. We thus limited our methane concentration to 3.9% and the hydrogen concentration to 38% for undoped films while for the doped films we used 20% and 22% hydrogen.

Chapter 5

Electronic Transport in Nanodiamond films

Earlier in chapter 2 we gave a brief introduction to electronic transport. In this chapter we present in greater detail models used by other researchers to explain electronic transport in nitrogen doped nanodiamond films. We will then discuss our results testing some of these models.

5.1 Activated and hopping conduction in nanodiamond films

Electronic transport in nitrogen doped ultrananocrsytalline diamond films has generally been explained using three different mechanisms namely (a) activated conduction (b) Hopping conduction and (c) weak localization. These mechanisms are strongly dependant on the amount of the nitrogen in the films, resulting in different density of states giving different electronic structures. Bhattacharyya et al [**10**] showed that heavily doped UNCD films with 10% to 20% nitrogen were metallic, moderately doped films with 5% to 8% were semi-metallic and films with less than 5% nitrogen were semiconducting see Fig 5.1 and Fig 5.2.

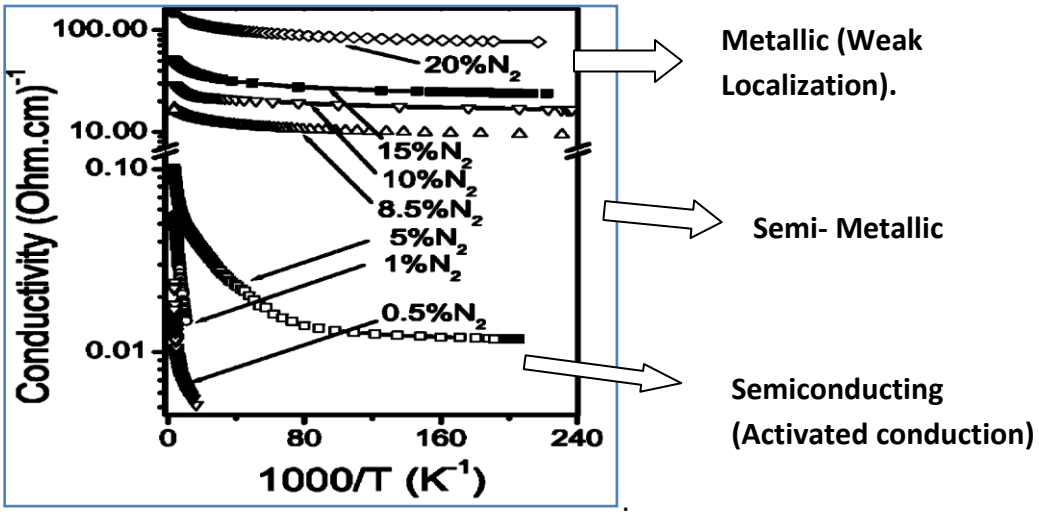


Fig 5.1: *Conductivity vs. inverse of temperature for different MWCVD UNCD films with different nitrogen percentages showing the different electronic properties obtained [**10**].*

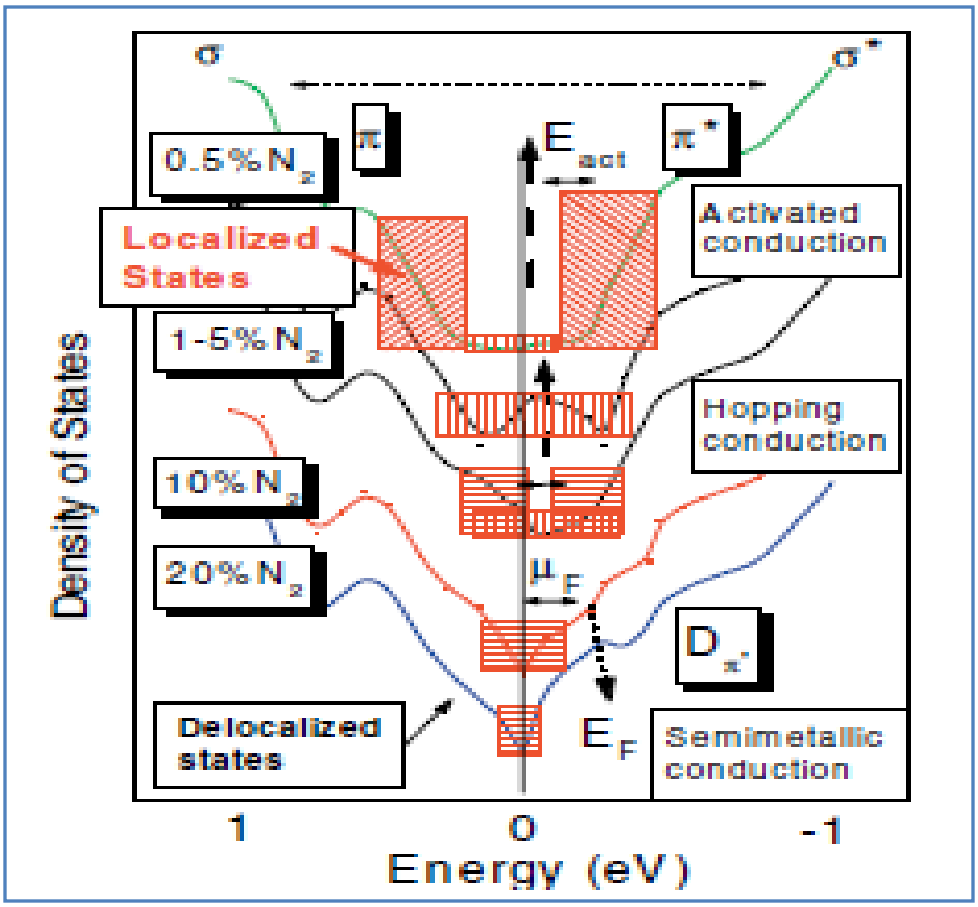


Fig 5.2: *An illustration of the variation of density of states with nitrogen percentage [**38**].*

Theoretical work by other reseachers attempted to explain the above experimental data using a computational program such as the Amsterdam density functional (ADF 2003) program [**39**]. The model is based on determining the electronic stuctures of several nitrogen centres (defect centres) in nanodiamond films and then predicting the contribution of the centre in conductivity. From the results, the conductivity in nanodiamond films was explained using three types of nitrogen centres formed in the grain boundaries, namely complex structures of nitrogen with dangling bond (N-DB), complex structures of nitrogen and π bond (N-π) and lastly nitrogen- vacancy complexes (N-V). The last structures were predicted to form shallow donors, while N-DB and N-π complexs are the compensation centres which do not contribute directly to

the conductivity. This is because they lie deep in the band gap. It is the shallow donors (N-V centres) that are activated into the conduction band and hence increase conducitivity see Fig 5.3 below which illustrate this model. However, Zapol et al [**40**] through tight binding studies indicated the formation of new electronic states associated with carbon π bonds and dangling bonds being introduced into the band gap and forming unoccupied states near the Fermi level and thus contributing to the conduction.

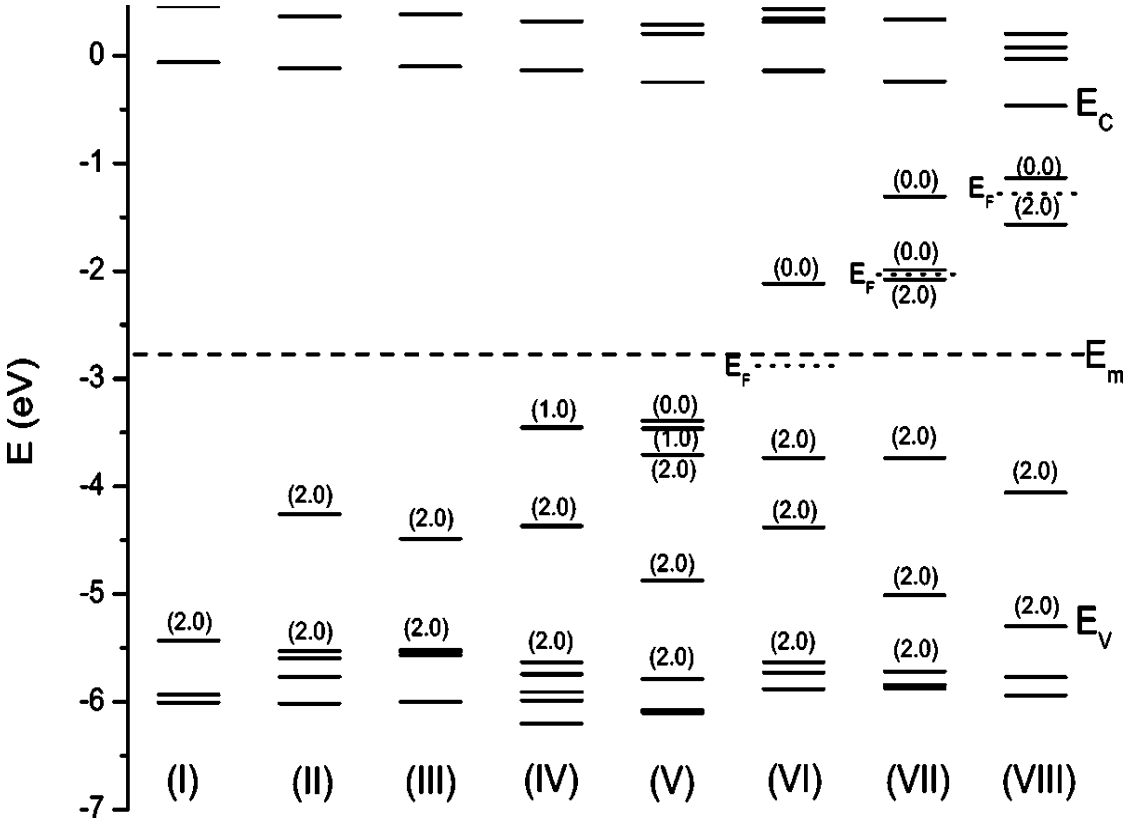


Fig 5.3: *Electronic structures of various N-centres formed in NCDs iii & iV are N-DB complexs, V & Vi are N-π while Vii & Viii are N-V complexs. E_c is the bottom of the conduction band, E_m is the middle of the band and E_v is the top of the valence band.*

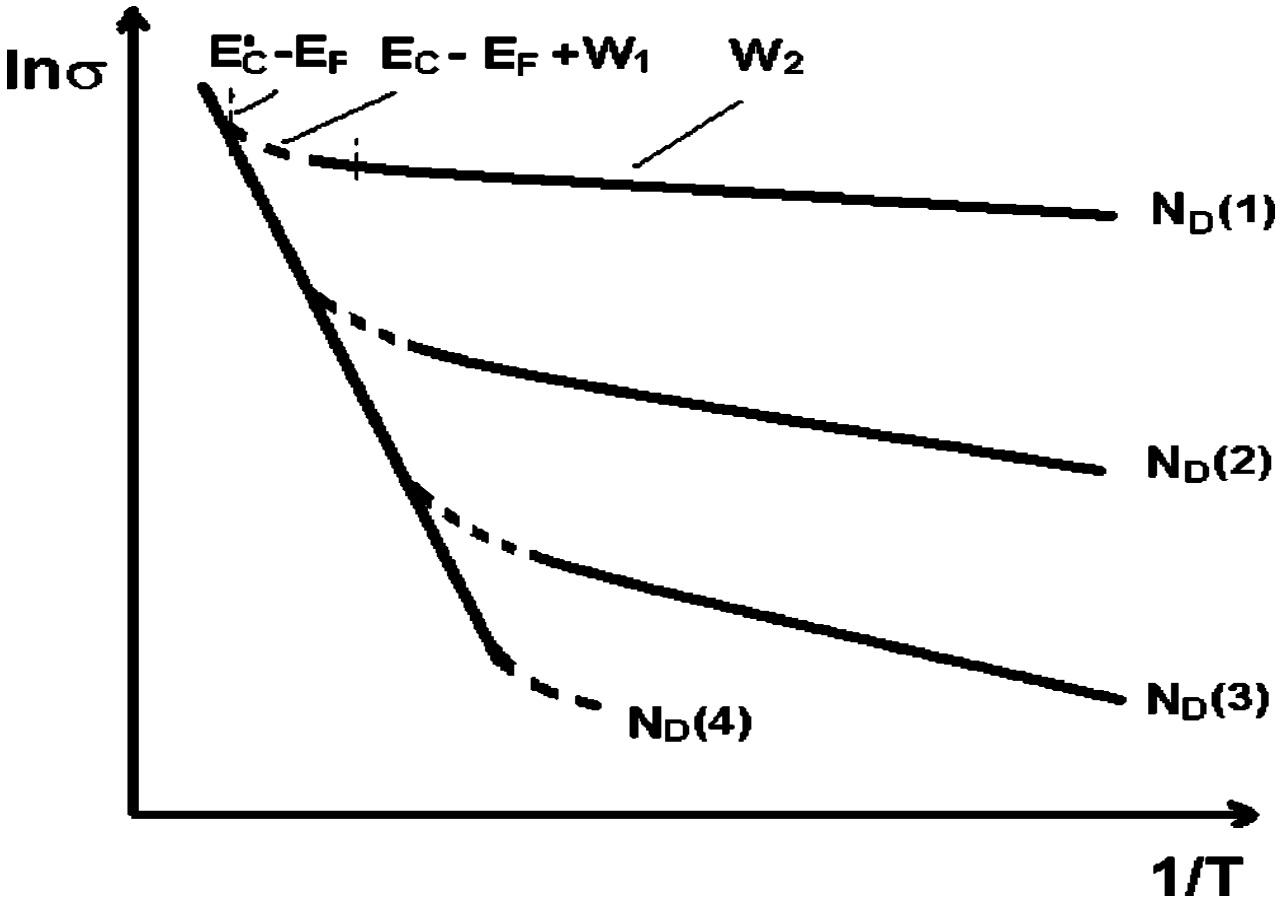


Fig 5.4: *Illustration of the temperature and nitrogen concentration depences of conductivity expected on model of Fig 5.5. W_1 and W_2 are activation energies. $ND_{(1)-(4)}$ are films with different nitrogen concentrations, with $ND_{(1)}$ having the highiest concentration [**39**].*

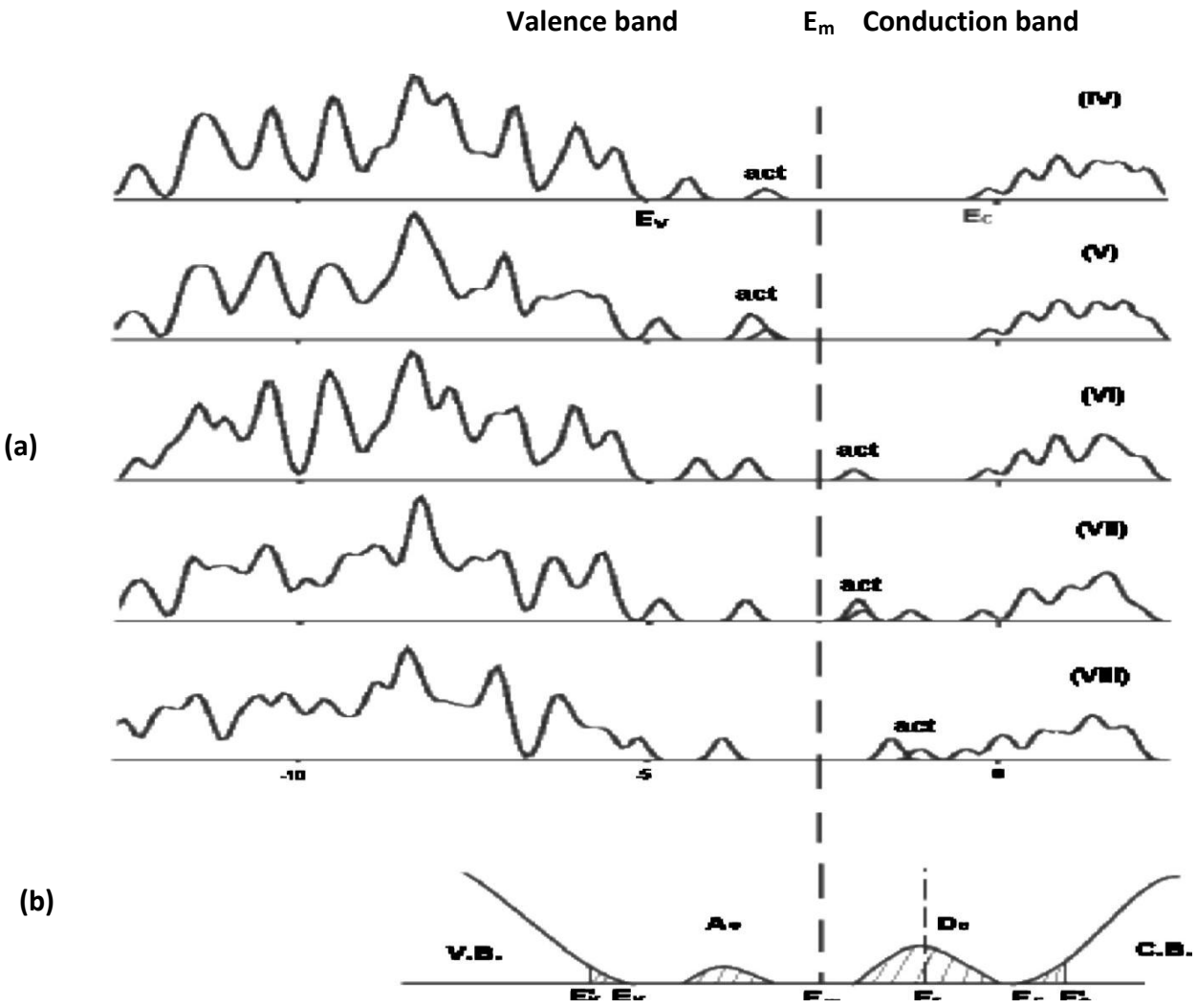


Fig 5.5: *(a) Schematic of the DOS of clusters in the conduction and valence band. N-V complexs have donor and acceptor sites (act) near the middle of the band gap.(b) Shows the effective donor & acceptor band for an n-type uncd film [**40**].*

The schematic diagram (Fig 5.5) of the density of states obtained from the ADF program shows that in films where we have N-V complexes, we have acceptor and donor sites (marked as "act" in Fig 5.5) in the middle of the band gap. The size of this impurity band determines the transport properties in the films. In semiconducting films the impurity band (act) is close to the conduction band and therefore activated conduction mechanism is predominating as shown in Fig 5.2 for 0.5% and 1% samples nitrogen [**10**]. When the impurity band (act) is very close to the conduction band, the hopping mechanism dominates. Lastly when there is a significant

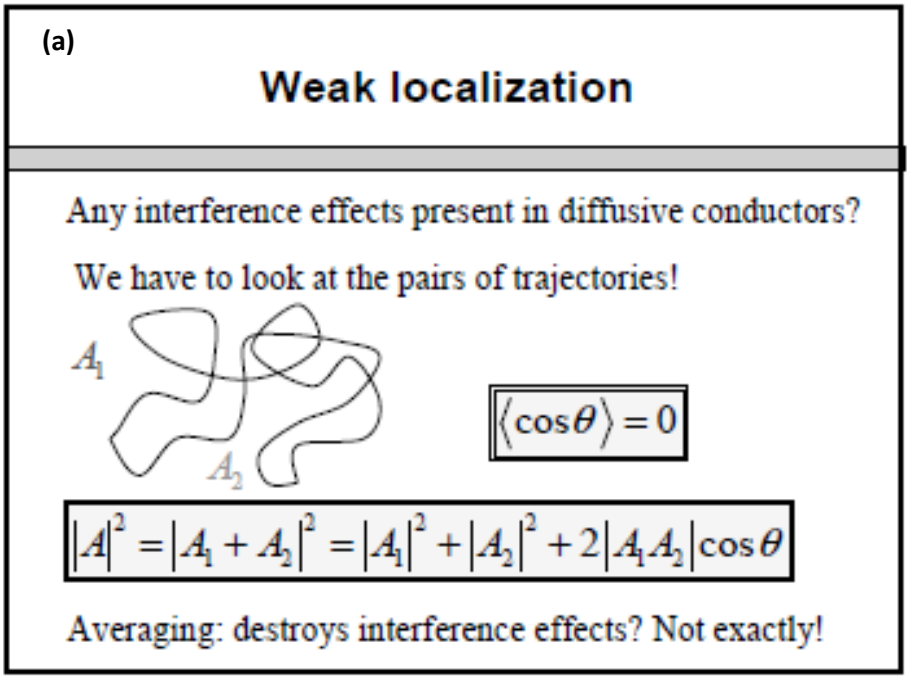
overlapping of the impurity band and the conduction band, a state known as delocalization, we have weak localization being the dominate mechanism (e.g. in semi-metallic/metallic films).

5.2 Weak localization in nanodiamond films

Heavily doped nanodiamond films have been found to be metallic as indicated earlier. In these materials weak localization becomes the dominant process and the conduction is diffusive. We will therefore first explain the concept of weak localization (WL) and the associated phenomenon of negative magnetoresistance and end with the different WL models.

According to Drude's model, the resistance of a material increases linearly with the number of electron scatterers and consequently the length of the material. In this context at high temperatures the phase relaxation length of the material is always less than the mean free path. The picture is however, different at low temperatures and in low-mobility materials; the phase relaxation length can be longer than mean free path. And thus the material can be viewed as a series of phase coherent units with elastic scatterers as was indicated in Fig 2.7. Interference between different scattering events of an electron's time reversed path results in enhanced back scattering and thus the electron becomes weakly localized. See illustration below Fig 5.6 (a) which shows the interference of two wave trajectories with probability amplitudes A_1 and A_2 and a phase difference, φ which depends on the angle of the magnetic field (Φ) to the material under investigation. This localization can be one dimensional if it is within the same layer of the lattice, otherwise it can be two or three dimensional.

The effect can however, be destroyed by a small field - typical values of such a field can be 100 G see Fig 5.6 (b). When this happens, it results in what is called negative magneto-resistance i.e. the conductance decreases with increase in magnetic field. Because this effect is very sensitive to phase relaxation length, unlike other transport mechanisms it can be used to measure phase relaxation length. It hence gives us a bird's eye view into quantum activities at the molecular scale getting us closer to the atomic scale.



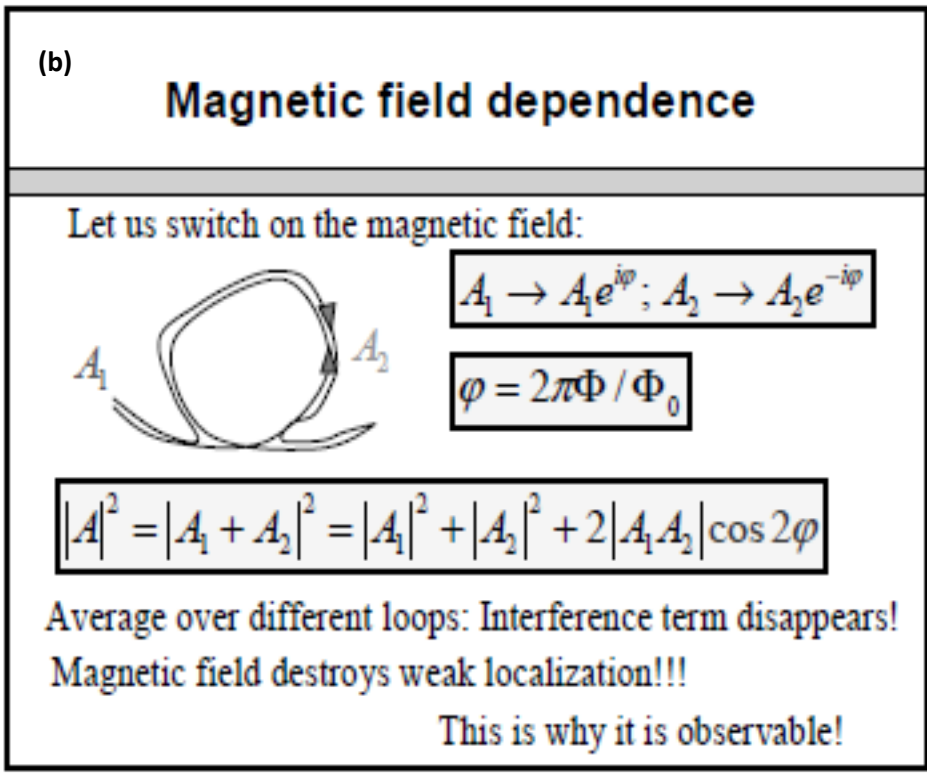


Fig 5.6*: An illustration of weak localization (a) without magnetic field (b) with a magnetic field.*

5.3 Two dimensional weak localization in nanodiamond films

In disordered materials the total conductivity in conventional isotropic systems is given by equation (3), below in which the first term represents the Drude conductivity, the second term is the correction due to weak localization and the last term represents the correction due to electron- electron interactions [**41**].

$$\sigma(0,T) = \sigma_o + \Delta\sigma(0,T)_{WL} + \Delta\sigma(0,T)_{e-e} \quad \text{in 2D or 3D.} \qquad (3)$$

In 2D, the weak localization part is given by

$$\Delta\sigma_{WL}(0,T) = \frac{e^2}{\pi\hbar}\ln\left(\frac{1}{L_{Th}}\right) = Bln(T) \qquad (4)$$

And the electron-electron interaction component is given by

$$\Delta\sigma_{e-e}(0,T) = \left(\frac{e^2}{4\hbar\pi^2}\right)\left(2 - \frac{3}{2}F\right)ln\left(\frac{\pi k_B T}{\hbar}\right) \qquad (5)$$

Where F, τ and k_B represent electron screening factor in 2D, the relaxation time for the e-e interactions and the Boltzmann constant, respectively [**42- 43**]. To test the applicability of this model we check for ln T dependence of the conductance. This was found to be not appropriate for all our nanodiamond films which shall be shown in the subsequent sections of this chapter.

5.4 Three dimensional weak localization in nanodiamond films

In conventional 3D weak localization isotropic model the conductivity is governed by the equation (6) below [**41**],

$$\sigma(0,T) = [G_o + a_1 T^{0.35} + a_2 T^{0.5}]\frac{l}{s} \qquad (6)$$

Where σ is the conductivity, the ratio ℓ/S is the sample geometrical conversion to conductivity with S being the cross sectional surface area and ℓ is the length of the sample (See Appendix A), a_1 and a_2 are defined in equation (7) and (8) respectively [**41**].

$$a_1 = {e^2}/{2\pi^2 \hbar L_\phi} \quad \left(\frac{C^2}{kg}\frac{S}{m^3}\right) \tag{7}$$

$$a_2 = \left(\frac{e^2}{4\hbar\pi^2}\right)\left(\frac{1.3}{\sqrt{2}}\right)\left(\frac{4}{3}-\frac{3}{2}F\right)\sqrt{{k_B}/{\hbar D}} \quad \left(\frac{C^2}{kgm^4}\frac{s}{k^{0.5}}\right) \tag{8},$$

where *D* is the diffusion coefficient and *F* is the electron screening factor, the rest of the standard symbols have their usual meaning.

Recent studies however, have shown that nanodiamond films have some anisotropic behavior. This behavior has been explained in terms of a propagative fermi surface (PFS); the model was originally developed to explain transport in disordered artificial superlattices and was recently used to explain the unusual transport in nano-crystalline silicon films considered as artificially formed superlattice [**43**]. In these anisotropic materials the magnetoresistance $(\Delta\sigma(B))$ behavior is governed by equation (9) below.

$${\Delta\sigma(B)}/{\sigma(0,T)} = \alpha\left[\sigma(0,T)\left(\frac{e^2}{2\hbar\pi^2}\right)\left(\frac{eB}{\hbar}\right)1^{0.5}\right] f_3\{{h}/{4D\tau_\phi eB}\} \tag{9}$$

The function f_3 is the Kawabata function proposed as

$$f_3(x) = \sum_{N=0}^{\infty}\{2[\,(N+1+x)^{0.5} - (N+x)^{0.5}] - \left(N+\frac{1}{2}+x\right)^{-0.5}\} \tag{10}$$

where *N* is the Landau quantum number (i.e. the discrete energy levels occupied by cyclotron orbits of the electrons in a magnetic field) [**44**]. The coefficient α describes anisotropic transport in 3D and the other symbols have their usual meanings. This function predicts a B^2 dependence at low fields and a $B^{1/2}$ at high fields. The isotropic model is described by the same equation without the α - the anisotropic coefficient which is a ratio of the diffusion coefficient parallel and perpendicular to the film.

We now begin our discussion on the results with the transport measurements for the nitrogen doped nanodiamond films which were prepared by two different methods HFCVD and MWCVD.

All discussions begin with the analysis of the resistance- temperature dependence (R-T) which is consolidated with that of magneto-resistance measurements. The doping was achieved by synthesis of nanodiamond films in an argon rich CVD with 10%, 20% or 22% nitrogen in the gas atmosphere.

5.5 Results and analysis of the 20% HFCVD-N_2 nanodiamond films

In this section we present the results for the nanodiamond films which were synthesized by the HFCVD technique with 20% nitrogen in the chamber. This however, should not be taken as the amount of nitrogen in the films. As highlighted earlier one of the objectives of this research was to synthesize high quality conducting nanodiamond films with semiconducting properties unlike the metallic behavior common to heavily doped MWCVD-N_2 nanodiamond films. Several attempts to get meaningful conducting films using 10% or less nitrogen in the chamber were not successful; this we attributed to the low power of the method when compared to the microwave technique. It is common knowledge that dissociation of nitrogen gas and incorporation into diamond films is not an easy task; it requires a lot of effort. However, increasing the nitrogen to 20% and above helped to improve the conductivity which, shall now be discussed.

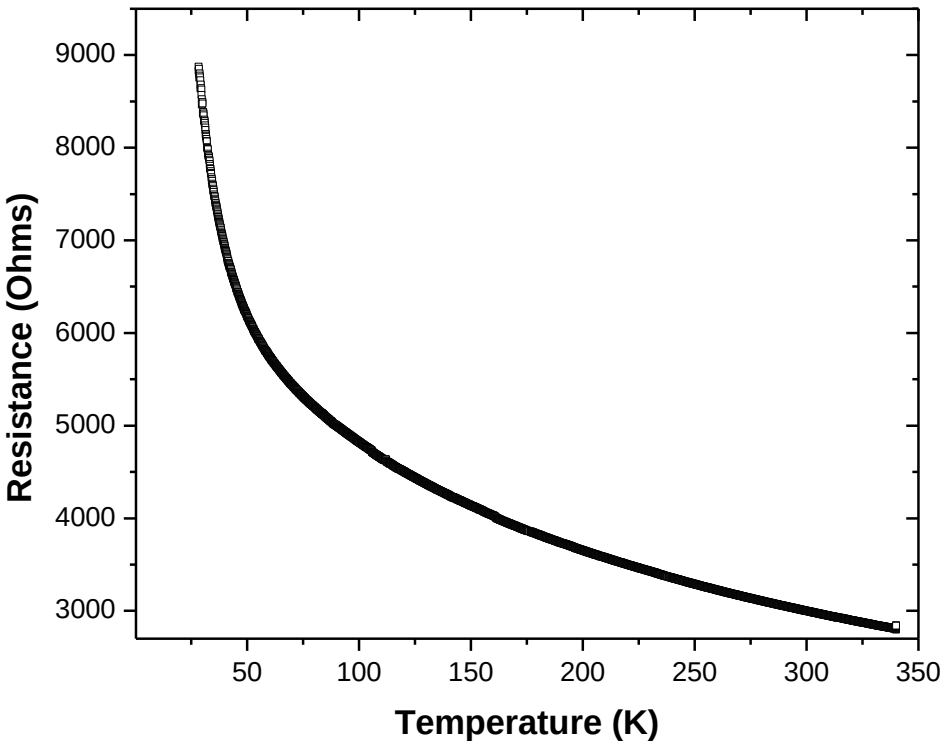


***Fig 5.7**: Resistance-Temperature dependence of 20% HFCVD-N_2 nanodiamond films showing a rapidly decreasing resistance with temperature.*

The graph, Fig 5.7 shows the rapidly decreasing resistance with temperature, a behaviour common in typical semiconducting materials. This is observed in the intermediate temperature range from 28 K to 89 K. In the lower temperature region these films were found to be very resistive making the measurement difficult with our system. The room temperature conductivity was measured to be 18.5 $\Omega^{-1}cm^{-1}$, a value much lower than 143 $\Omega^{-1}cm^{-1}$ reported by Bhattacharyya et al in MWCVD ultrananocrsytalline films [**10**]. This large discrepancy is an indication of the different nitrogen doping levels in the films. Therefore a different mechanism in 20% HFCVD-N_2 films is expected other than that observed in MWCVD-N_2 films. Furthermore, MWCVD-N_2 films and 22% HFCVD-N_2 were found to be conducting even down to 2.3 K. A possible explanation to this is the different nitrogen level in the films.

The fact that the conductivity of 20% HFCVD-N_2 was measurable from 28 K up to room temperature would suggest some thermally activated conductivity. We thus check for this kind of conduction mechanism.

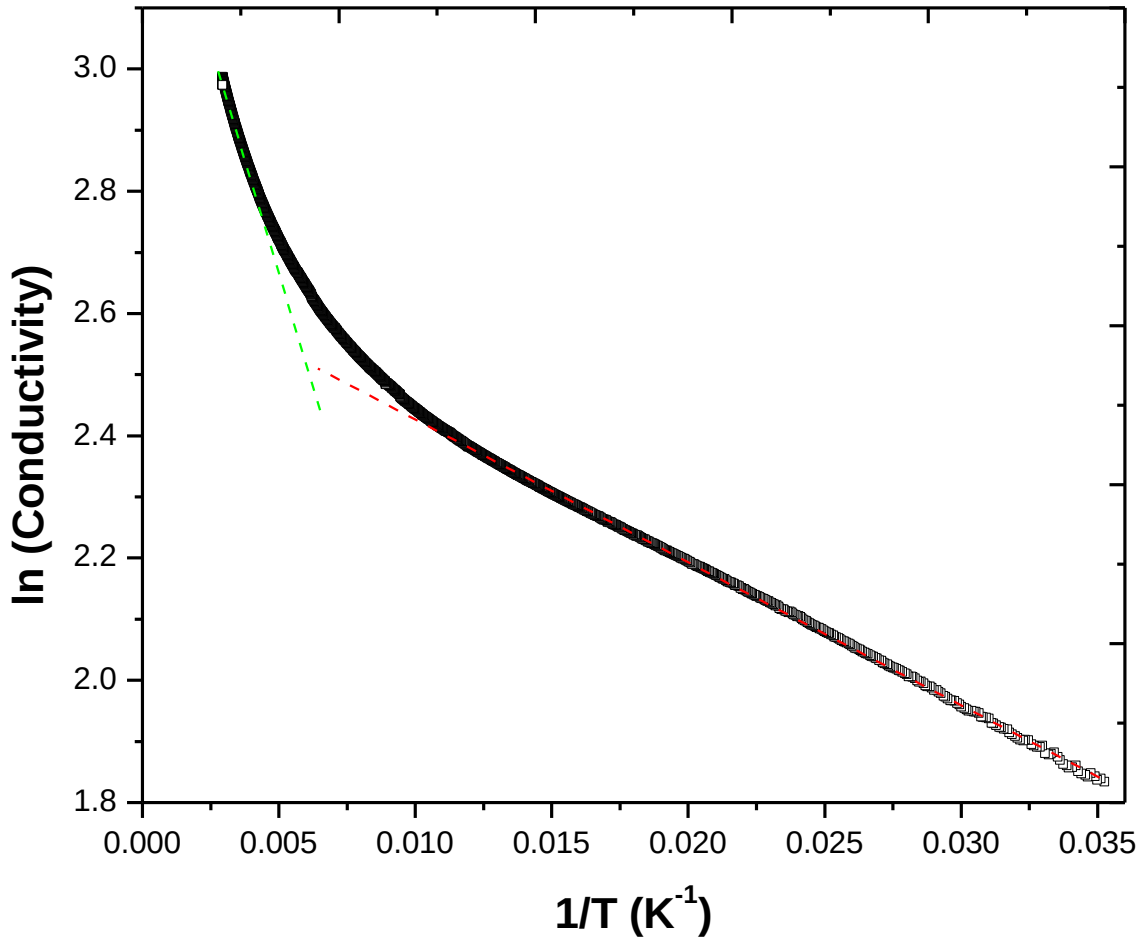


***Fig 5.8**: Arrhenius plot for the conductivity of the 20% HFCVD-N_2 films to check for activated conduction mechanism. The dotted lines are to guide the eyes.*

At high temperatures thermally activated conduction is normally expressed in the form of Arrhenius equation (11) [**45**].

$$\sigma(0,T) = \sigma_o e^{-\Delta E/kT} \qquad (11)$$

where ΔE is the activation energy $\sigma(0,T)$ and σ_o are the conductivities at temperature (T) and absolute zero respectively.

From the Arrhenius plot, Fig 5.8, the linearity of this plot in the range from 28 K to 89K indicates that we have activated conduction in this temperature region. The activation energy calculated from the plot is found to be approxiamtely 18.2 meV. The low activation energy and the non-arrhenius behaviour at higher temperatures suggests the presence of an impurity conduction band slightly below the conduction band which implies that at higher temperatures the electrons are excited into the conduction band and thus we observe a semi-metallic behaviour at high temperatures.

Since we are investigating polycrsytalline materials which normally have amorphous componets in the grain boundaries, and hence possible contributions from hopping, we can consider the Variable Range Hopping (VRH) model put forward by Mott [**46**]. Under this model the R-T variation is governed by the equation (12) below

$$R(0) = R_o e^{(\frac{To}{T})^{1/d+1}} \qquad (12)$$

where R_o is the characteristic resistance, which may depend weakly on temperature and *d* has a value depending on the nature of the hopping process i.e. the dimension of the hopping. T_o is the characteristic temperature coefficient which depends on the density of states {N (E_F)} at the Fermi level. The same equation is applicable in the presence of a Coulomb gap with a change in the value of *d* as suggested by Efros-Shklovskii [**47**].

$$T_{o,Mott} = {}^{18}/_{k_B L_c{}^3 N(E_F)} \qquad T_{o,ES} = {}^{2.8e^2}/_{k_B L_c \varepsilon} \quad \text{In 3D} \qquad (13)$$

k_B is the Boltzmann constant, L_c is the localization length, ε is the dielectric constant of the material and *e* is the elementary charge of an electron [**46**].

To check these models we plot ln R vs T^{-x} where x can be 2, 3 or 4 for 1D/ (ES), 2D or 3D hopping respectively.

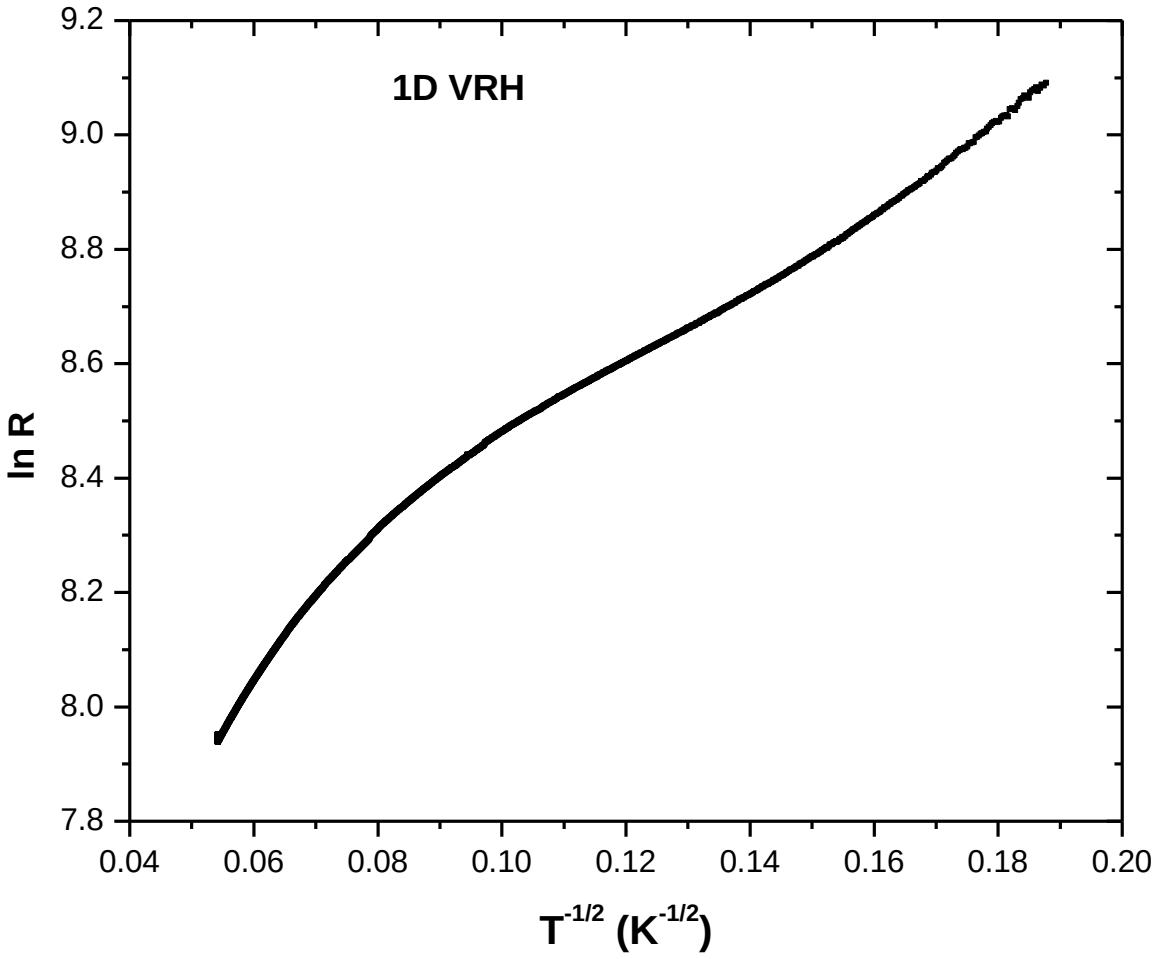


***Fig 5.9**: ln R vs. $T^{-1/2}$ graph to check for 1D or ES VRH in the 20% HFCVD-N_2 films.*

The graph above, (Fig 5.9) shows that this mechanism (1D) is not applicable for our material as indicated by the non linearity of the graph on a significant temperature range.

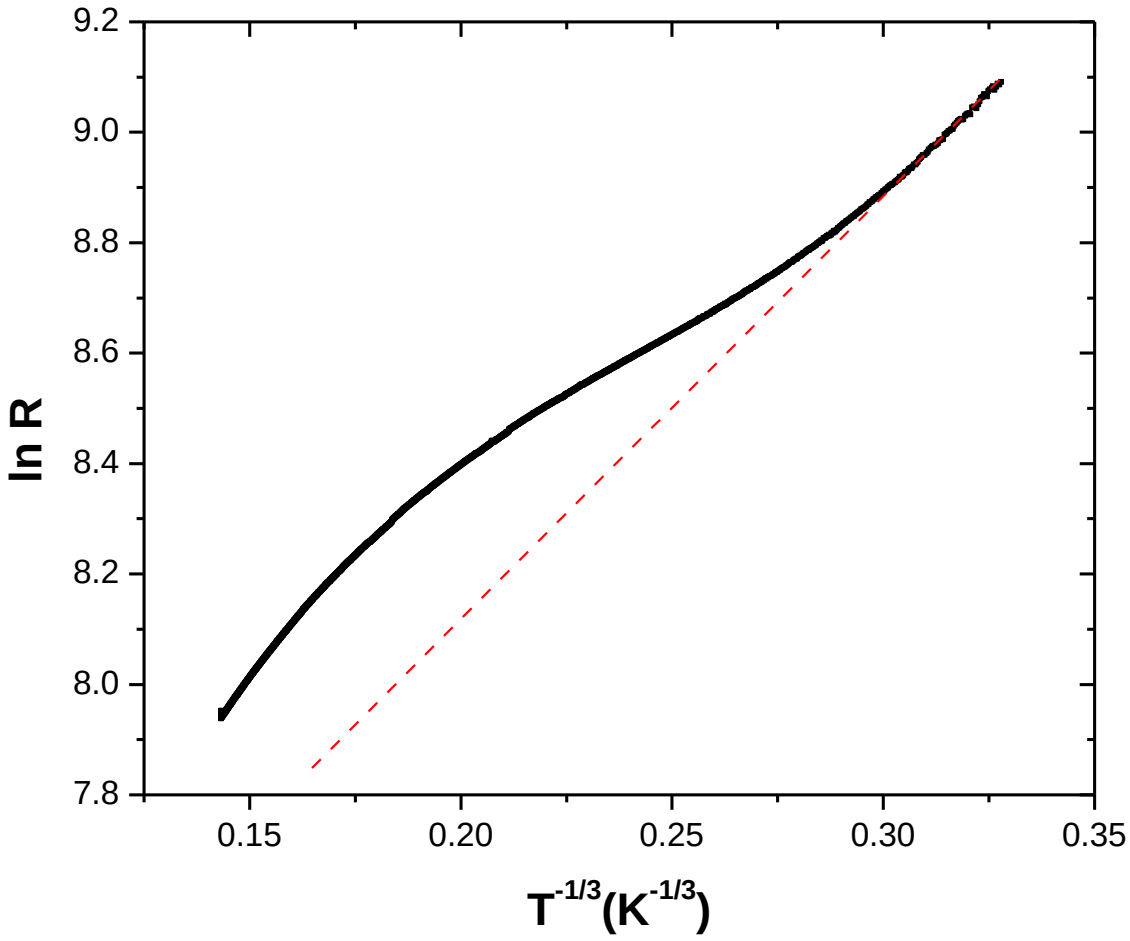


Fig 5.10: *ln R vs. $T^{-1/3}$ to check for 2D VRH in the 20% HFCVD-N_2 films.The dotted line is to guide the eyes.*

From the graph, Fig 5.10 we observe non linearity on a wide temperature range. There is some linearity for a small temperature range (28K- 33K). This is not a significant temperature range and as such we can rule out 2D VRH as major contributor to the conduction in the 20% HFCVD-N_2 films.

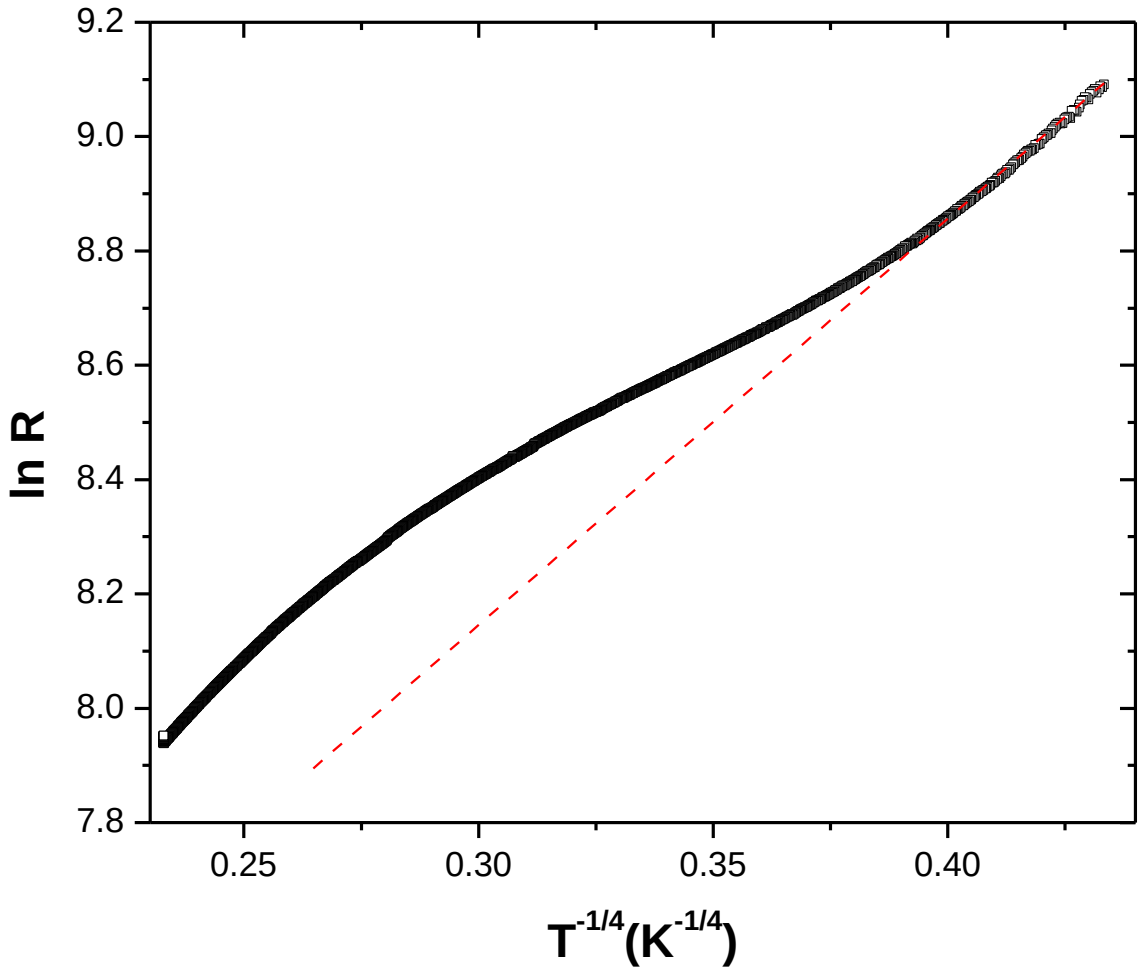


Fig 5.11: *ln R vs. $T^{-1/4}$ plot to check for 3D VRH mechanism in the 20% HFCVD-N_2 films.*

The fitting in Fig 5.11 seems to suggest 3D VRH hopping in our system in the temperature range from 28 K to about 90 K. We will therefore extract some parameters from this fit and that of magnetoresistance to try and confirm the mechanism. From the graph, Fig 5.11 we obtain the Mott characteristic temperature as 3.11 K. A fit of the MR data using the hopping equation (17) in chapter 6, gave us the localization length L_c to be 11.9 nm which implies a hopping distance of 6.75 nm. The density of states has been found to be 3.98 x 10^{22} $eV^{-1}cm^{-3}$. This figure for the density of states is unrealistically too large for strongly localized states and this means that the hopping mechanism is not appropriate for our films and therefore the fit above (Fig 5.11) is misleading. We therefore need further investigations.

We have seen that at higher temperatures we do not observe hopping mechanism or activated conduction we therefore check for band conduction mechanism such as weak localization which is observed in metallic/semi-metallic materials. The conductivity has been found to be governed by the equation (3) given earlier in both 2D and 3D isotropic systems.

The total conductivity is a sum of the classical Drude conductivity, weak localization and electron-electron interactions corrections. We observe logarithmic behavior in conductance for a very small temperature range (from 28K to 42K) see insert of fig 5.12 and this eliminates 2D WL mechanism as major contributor to the conduction and thus we consider the 3D WL mechanism.

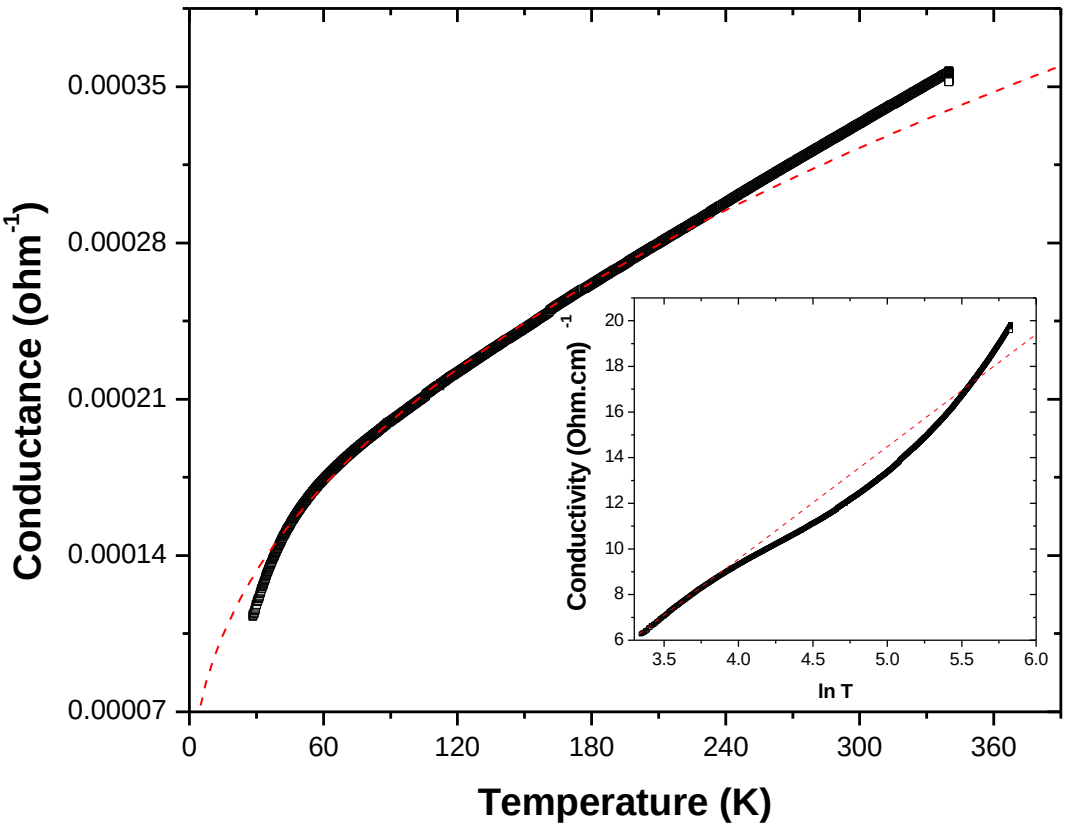


***Fig 5.12**: Conductance- Temperature graph with 3D WL fit (dotted line) for the 20% HFCVD-N_2 films. The insert is a graph of Conductivity vs. ln T plot to show the insufficiency of the 2D WL model in the 20% HFCVD-N_2 films.*

In 3D the conductivity is given by equation (6) as indicated earlier. From the fitting of conductance-temperature graph (Fig 5.12) using equation (6) we can see that the model approximates the material behavior well at intermediate temperature range (40- 180K). The analysis in the high temperature region becomes complex because so many factors come into play, such as phonon interactions and lattice vibrations. The fitting equation is however slightly modified with the temperature dependence of the weak localization component being $T^{-0.33}$ and not $T^{-0.35}$. The fitting parameters are

$$a_1 = 2.4 \times 10^{-5} \left(\frac{C^2}{kg}\frac{S}{m^3}\right)$$

$$a_2 = 9.3 \times 10^{-4} \left(\frac{C^2}{kgm^4}\frac{s}{k^{0.5}}\right)$$

$$G_o = 1 \times 10^{-4} \ (Ohm^{-1})$$

Using the fitting parameters and equations (7) and (8), and taking *F* to be 0.3 as reported by other researchers [**43**] we get the Diffusion coefficient $D = 3.22 \times 10^{-8} m^2 s^{-1}$

And the temperature dependence of $L_\phi = 1.12\ x\ 10^{-8} T^{-0.33} (m)$ obtained from equation (7) and using the fitting parameter a_1.

The diffusion coefficient for these samples was found to be a little lower than, the microwave samples. This could possibly be due to increased impurity scattering in the film. From the R-T measurements of the 20% HFCVD-N_2 we have observed 3D weak localization corrections to the classical Drude conductivity and we have some contribution from electron-electron interactions. We shall compare these with those of microwave films in the subsequent subsection, but before that, we will now turn to the MR analysis of these (20% HFCVD-N_2) films.

MR results

At present we cannot make conclusive remarks about transport mechanisms using the R-T measurements only. We need to confirm and cross check some parameters such as dephasing length and its temperature dependence using magnetoresistance measurements. Only if there is a correspondence can we then make a conclusion about the mechanism in the material. It is

against this background that we did some MR measurements on our nanodiamond films. The measurements were done up to 12T magnetic field and a temperature range from 30K to 80K temperature, because from the R-T Measurements this is the range where we observe 3D weak localization. The magneto-resistance is calculated as

$$MR = \frac{R_B - R_0}{R_0}$$

Where R_B is the resistance at a field B in Tesla, R_0 is the resistance when the field is zero.

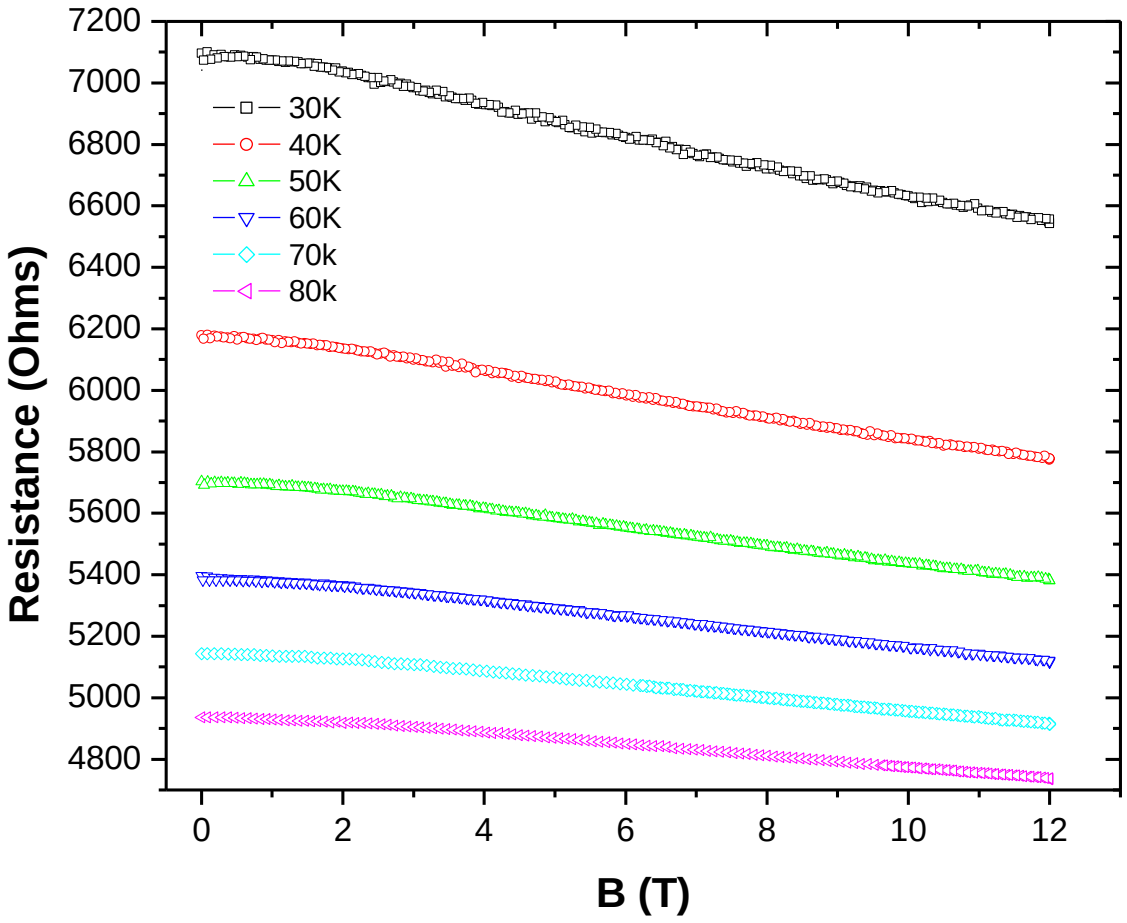


Fig 5.13: *Resistance vs. Magnetic field plot for 20% HFCVD-N_2 nanodiamond films.*

From the graph (Fig 5.13) we observe a parabolic dependence of resistance at low fields and the behavior at high fields is not quite clear using this scale plot. From this plot it appears as if we have a linear dependence of the resistance with B, which would suggest hopping mechanism [**48**], but a plot of the same results using $B^{1/2}$ scale tells us otherwise (see the graph of figure 5.14 and the insert).

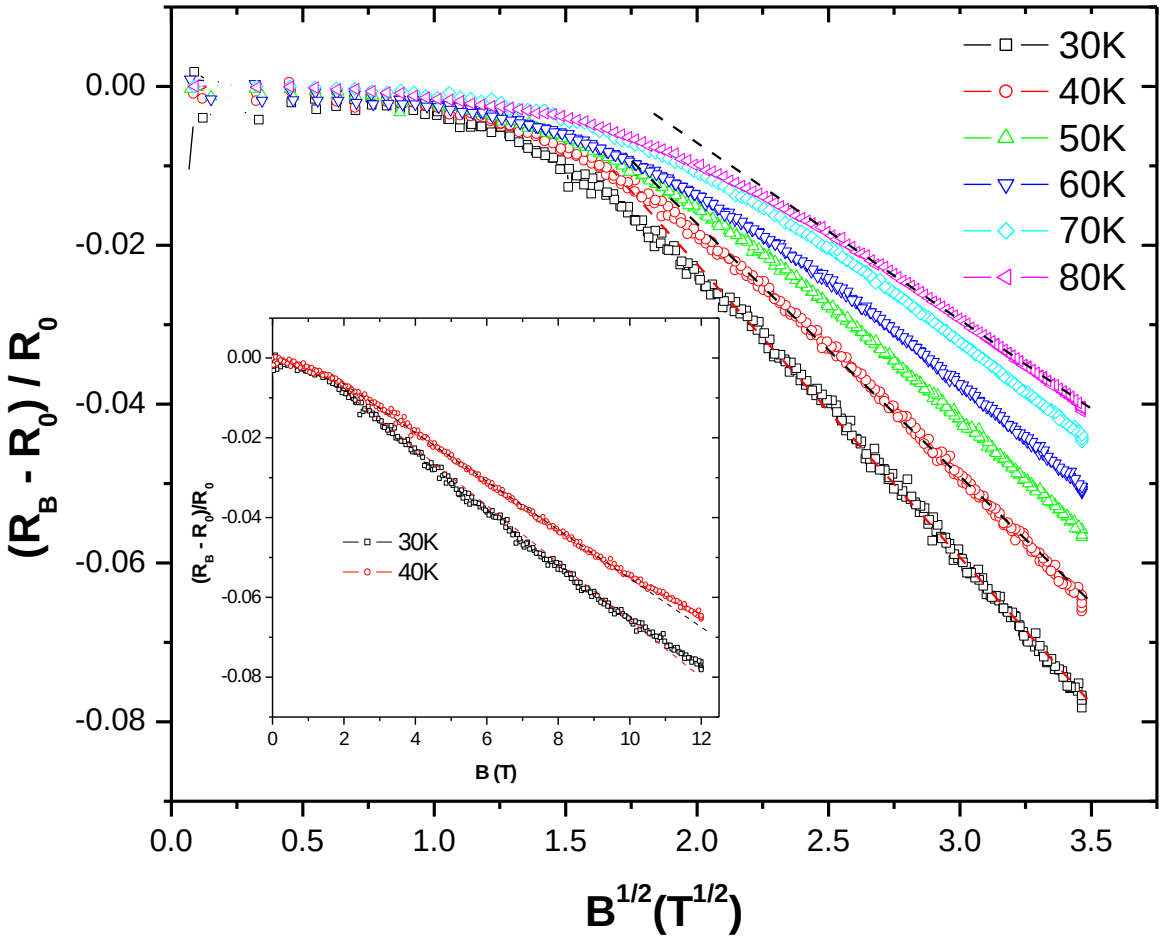


***Fig 5.14**: Shows the $B^{1/2}$ dependence of MR at high fields and the insert shows the non-linear B dependence of MR for 20% HFCVD-N_2 films.*

From Fig 5.14 it is evident that we have a $B^{1/2}$ dependence of the MR and not linear B dependence at high fields as shown by the insert of the graph, such a behavior is not

characteristic of hopping mechanism [**48, 53**]. Since magnetoresistance is more sensitive to the structure of the film than just simple resistance - temperature dependence (R-T). We then can safely rule out hopping mechanism as a major contributor to the conductivity in our films. The 3D VRH fittings which we obtained earlier can be regarded as just some artificial fit with no physical meaning. Since it gave us unreasonable high values for the density of states and furthermore we do not observe a linear B dependence in MR, which is characteristic of hopping mechanism. The $B^{1/2}$ dependence of MR is characteristic of 3D weak localization. This is in agreement with reports by other researchers that have indicated a $B^{1/2}$ or B^2 dependence of MR [**50**]. In addition the MR does not seem to saturate or turn upwards into the positive regime as is the case in hopping when there is wavefunction shrinkage. The magnitude of this MR decreases with an increase in temperature indicating that weak localization effects are suppressed at high temperatures.

Another model we will check is the recently reported 3D WL anisotropic model used to explain conductivity in nanodiamond films [**43]**. In the graphs that follow Fig 5.15 and Fig 5.16 we normalize this data (MR) and fit it with both isotropic and anisotropic model. The graph Fig 5.15 shows the inadequacy of the isotropic model, it clearly shows a pronounced deviation from the MR data as the magnetic field is increased as clearly shown by the insert of the graph.

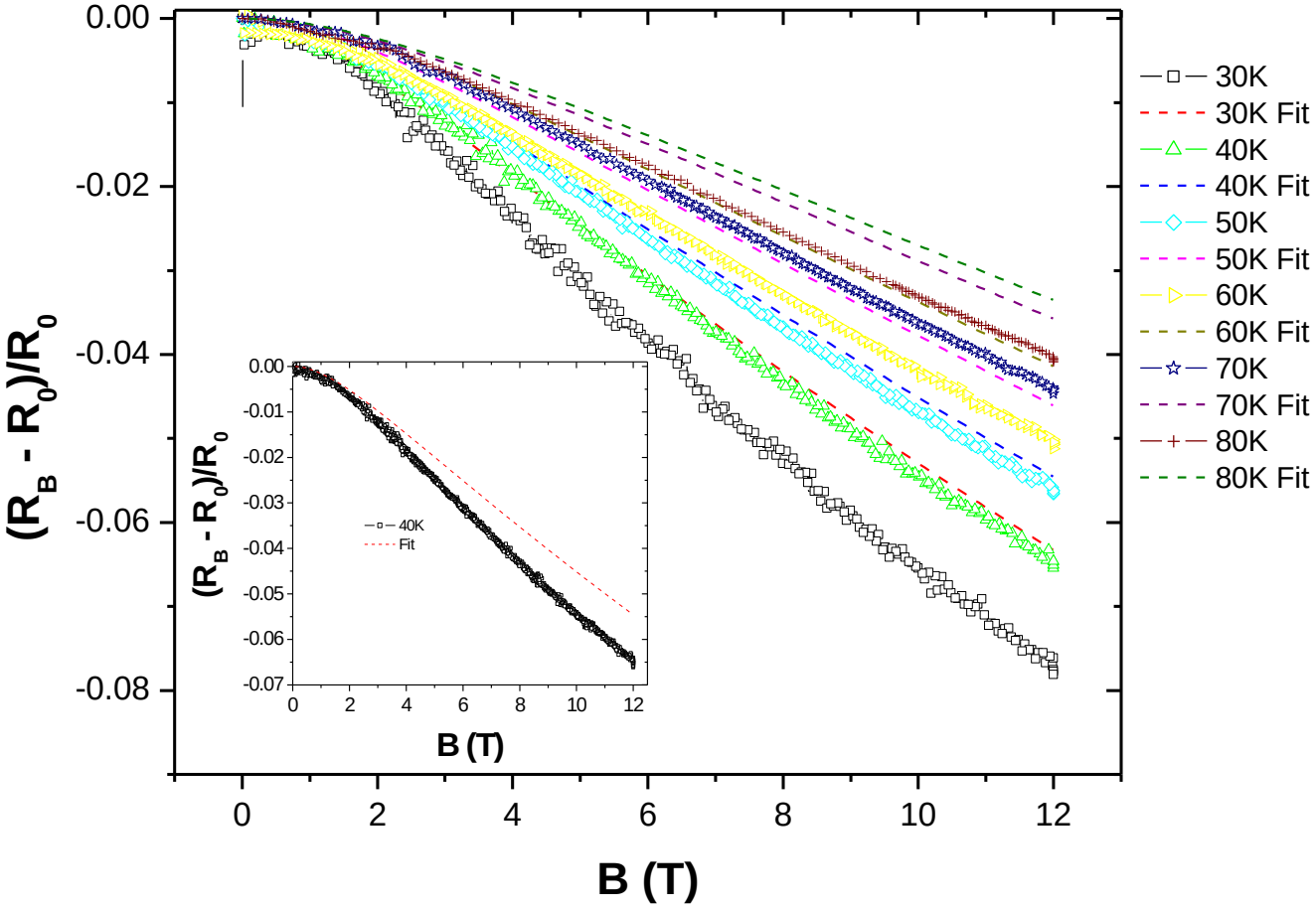


***Fig 5.15**: MR Results with Isotropic fit for the 20% HFCVD-N_2 films. The insert shows the deviation of the fit as the field is increased.*

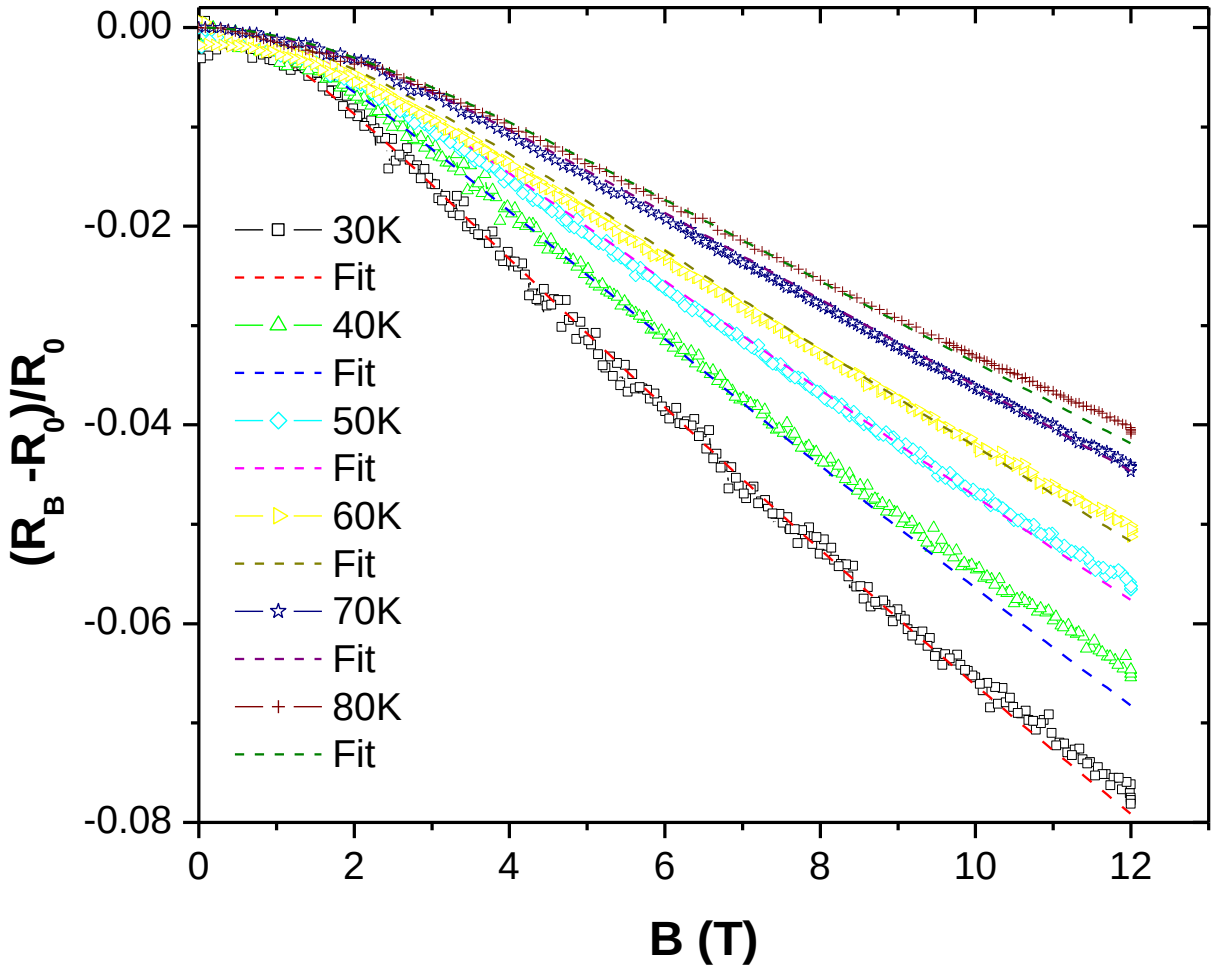


Fig 5.16: *MR results with anisotropic fitting for 20% HFCVD-N_2 nanodiamond films.*

The above fitted data in Fig 5.16, confirms that the 3D weak localization anisotropic model best describes the magnetoresistance behavior for these films. The anisotropic coefficient for this particular film was found to be 1.5. This value is 1.5 less than the commonly reported figure of three which indicates a weak anisotropic behavior in these films. The physical origin of this behavior is not yet fully understood but it might be due to non uniformity of the film during synthesis which results in anisotropic distribution of disorder in the grain boundaries. More

work in this regard is therefore recommended. From the fitting of the data we extract the dephasing length and determine its temperature dependence.

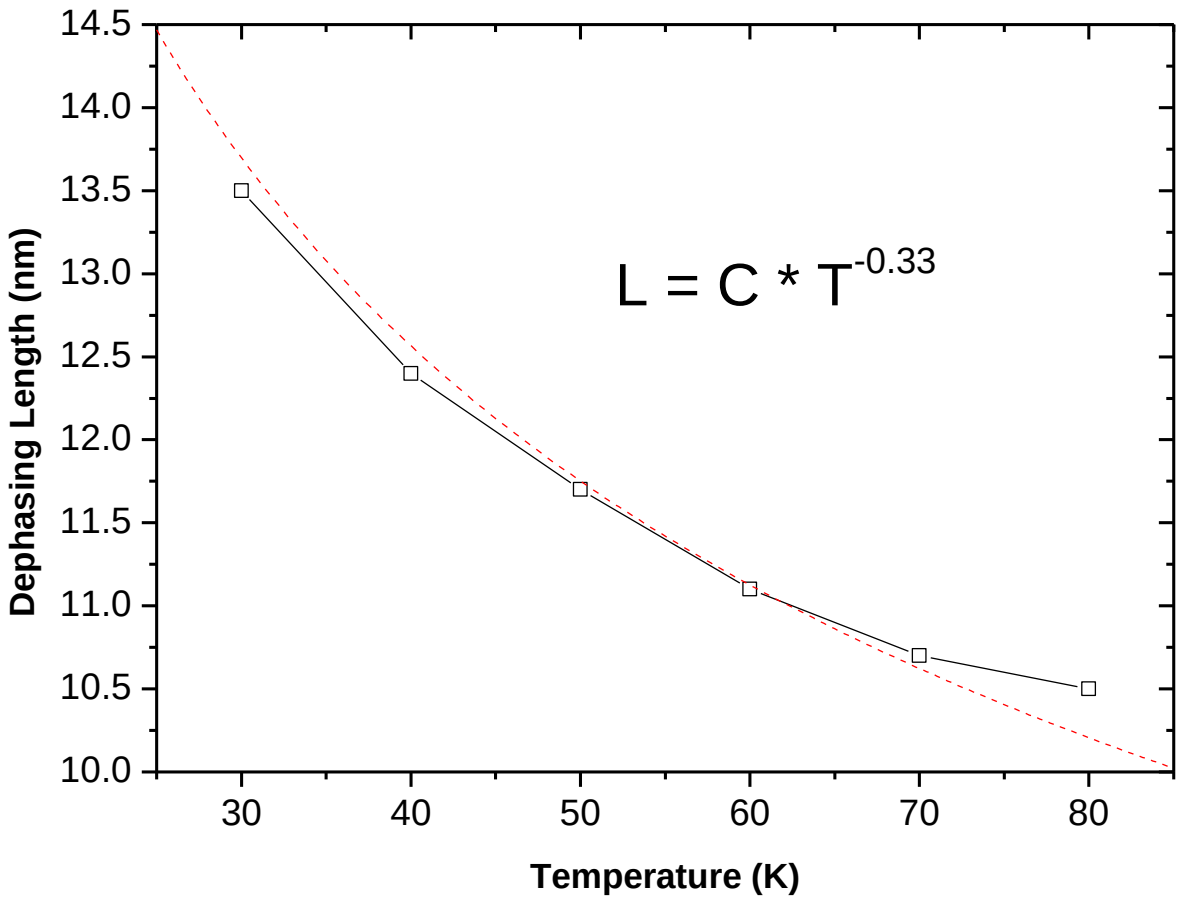


***Fig 5.17**: A graph showing the temperature dependence of the dephasing length for the 20% HFCVD-N_2 films.*

Fig 5.17 indicates that the dephasing length has a temperature dependence that corresponds to that obtained in the R-T analysis. This confirms that this anisotropic weak localization model is appropriate to explain the conduction mechanism in this intermediate temperature range. Overall we observe that the conductivity in 20% HFCVD-N_2 nanodiamond films has low temperature dependence. This would make these films thermally stable electronic devices.

5.6 Results and analysis for the 22% HFCVD-N_2 films

In this section we present the results of the nanodiamond films that were synthesized with slightly more nitrogen in the chamber. A small percentage change in the gas chemistry has shown us to have a significant big change in the electrical properties of the films thereof. Bhattacharyya et al [**10**] indicated that nitrogen doping increases the conductivity in nanodiamond films by 10^4 times, it is therefore not surprising that a small change in the nitrogen percentage would have a drastic change in the film's electrical properties. The graph (Fig 5.18) below shows the R-T results for the 22% HFCVD-N_2 films.

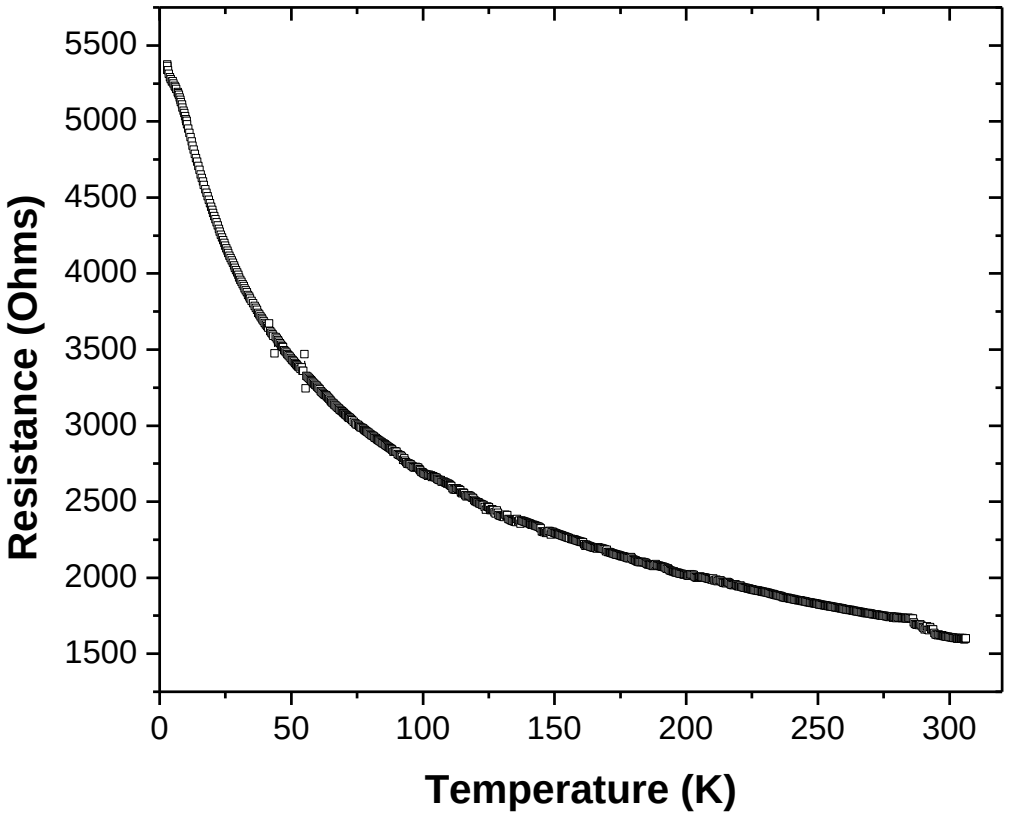


Fig 5.18: *A graph showing the R-T results for the 22% HFCVD-N_2 films.*

From the graph, Fig 5.18 we notice that the 22% films are conductive at very low temperatures of 2.3K which is not the case for the other films. However above 50K the films behavior appears

to be similar. We will now try and establish the conduction mechanism for the 22% films at low temperatures; we have already established activated conduction mechanism for the 20% films. We will now first check for hopping conduction mechanism by plotting ln R vs. T^{-x}.

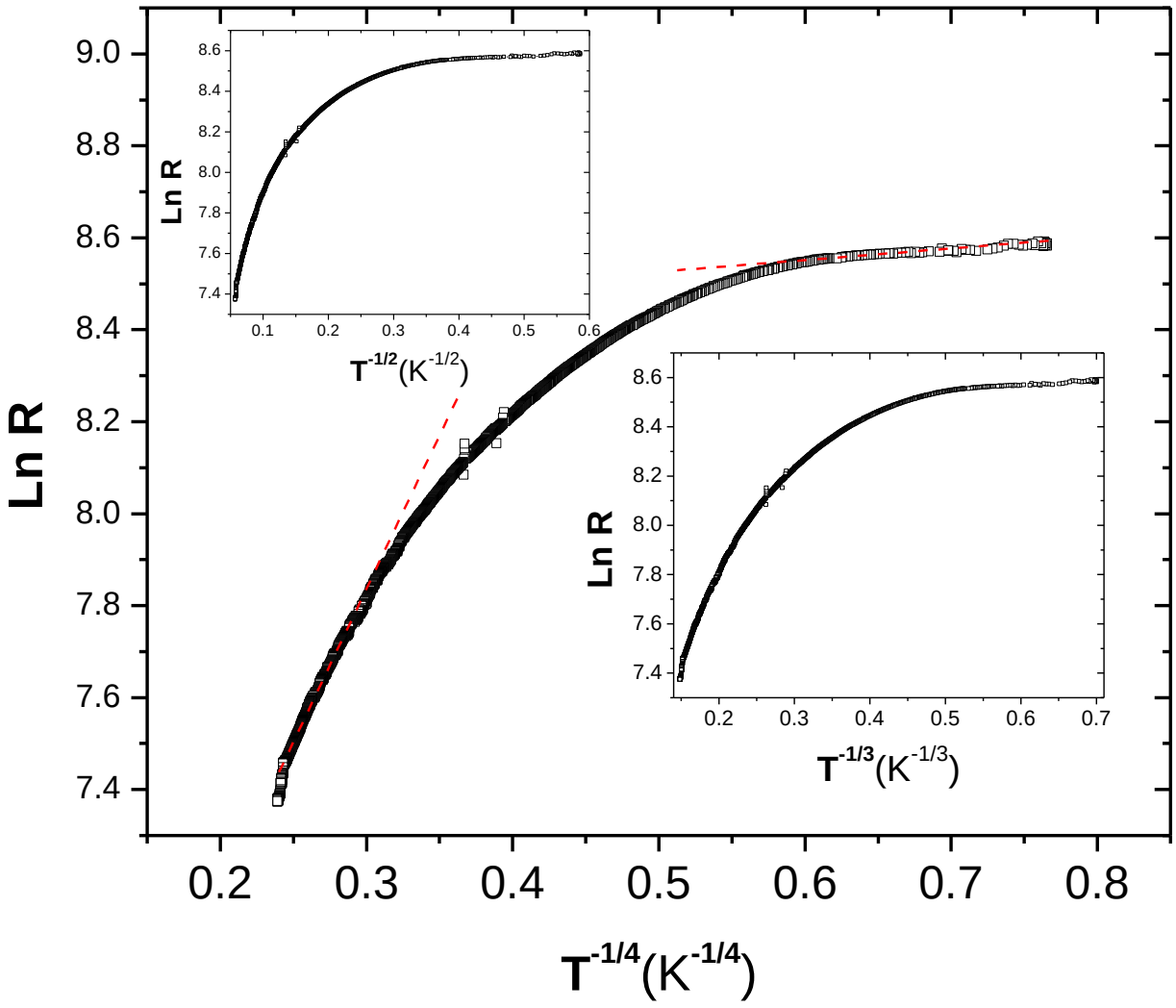


Fig 5.19 *Ln R vs. T^{x} graphs to check for hopping conduction mechanism (1D-top insert, 2D- bottom insert, and 3D- main graph) in the 22% HFCVD-N_2 films.*

The non linearity of the graphs in fig 5.19 clearly, shows that hopping mechanism is not the appropriate mechanism for our films. We therefore check for activated and 2D weak localization mechanisms. The inserts in Figure 5.20 confirms that these two models again

cannot best describe the behavior of our films at low temperatures. This is shown by the non-linearity of the top insert (activated conduction) and the bottom inserts (2D weak localization). The main graph shows the conductance vs. temperature fitted with the 3D Weak localization model. The graph (Fig 5.20) shows that the 3D WL model is the best mechanism to describe behavior of our films in the low and intermediate temperature range. This is typical of semi-metallic behavior reported in highly nitrogen doped ultrananocrystalline diamond films.

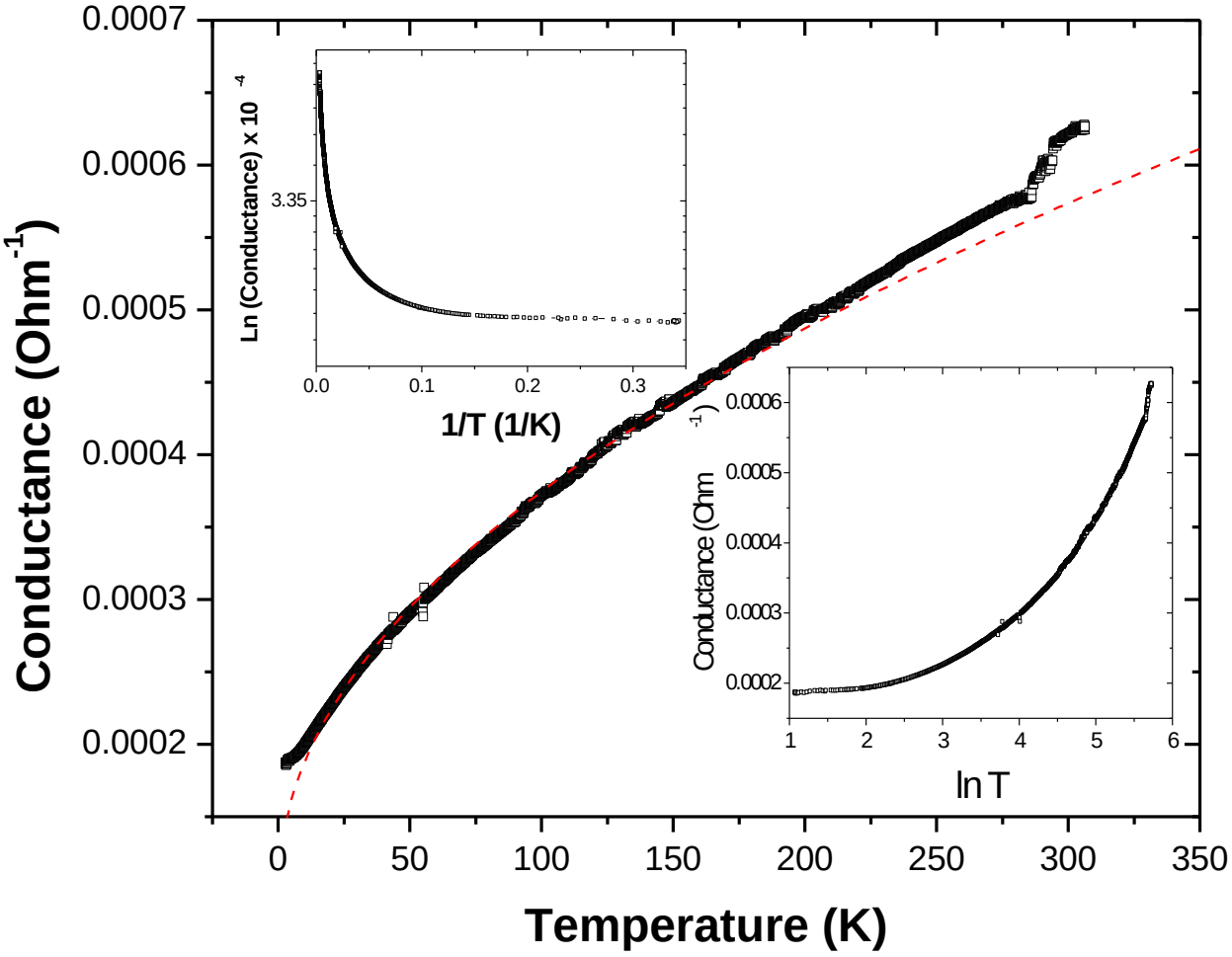


Fig 5.20: *Conductance vs. Temperature graph for the 22% HFCVD-N2 fitted with 3D WL model. The top insert is the Arrhenius plot of the conductance vs. temperature graph to check for activated conduction, while the bottom insert is the conductance vs. ln T graph to check for 2D WL.*

We have thus far established a semi-metallic behavior in the 22% HFCVD-N_2 films, in which 3D weak localization processes, dominates. The fitting parameters are:

$$a_1 = 1.5 \times 10^{-5} = {e^2}/{2\pi^2 \hbar L_\phi} \left(\frac{C^2}{kg}\frac{S}{m^3}\right)$$

$$a_2 = 2.67 \times 10^{-5} = \left(\frac{e^2}{4\hbar\pi^2}\right)\left(\frac{1.3}{\sqrt{2}}\right)\left(\frac{4}{3}-\frac{3}{2}F\right)\sqrt{{k_B}/{\hbar D}} \left(\frac{C^2}{kgm^4}\frac{s}{k^{0.5}}\right)$$

$G_o = 0.0001\ (Ohm^{-1})$

Using the fitting parameters and equation (6) and (7) we obtain the temperature dependence of the dephasing length to be $L_\phi = 3.89 \times 10^{-8}\ T^{-0.35}$

This is a weak temperature dependence although the prefactor is higher than that obtained for the 20% HFCVD-N_2 films. This is due to the differences in film thickness for the two samples. We will now turn to the magnetoresistance measurements to confirm these results. As we have indicated earlier magnetoresistance measurements are more sensitive to the structure of the material and thus can be considered more reliable than simple R-T measurements.

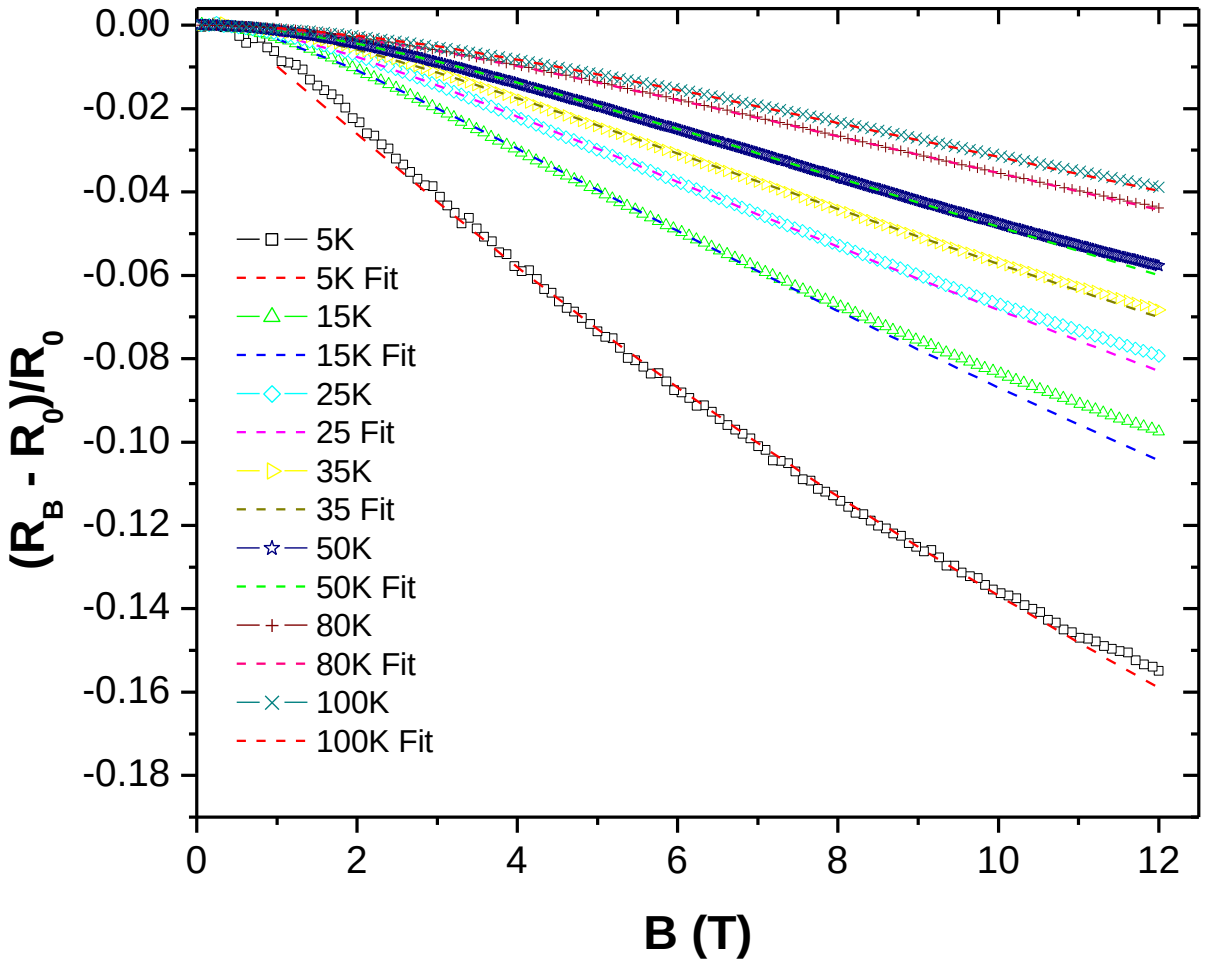


Fig 5.21: *Normalized magnetoresistance data fitted with the anisotropy 3D weak localization model for the 22% HFCVD-N_2 films.*

The above graph (Fig 5.21) indicates that the anisotropic 3D WL model is appropriate to explain the MR behavior of our films at low temperatures. The anisotropy coefficient was found to be 2.1, a value 0.6 more than that we observed for the 20% HFCVD-N_2 films. The explanation to this is due to structural differences in the films since these films have more nitrogen. From the MR measurements we are able to extract the dephasing length and determine its temperature dependence.

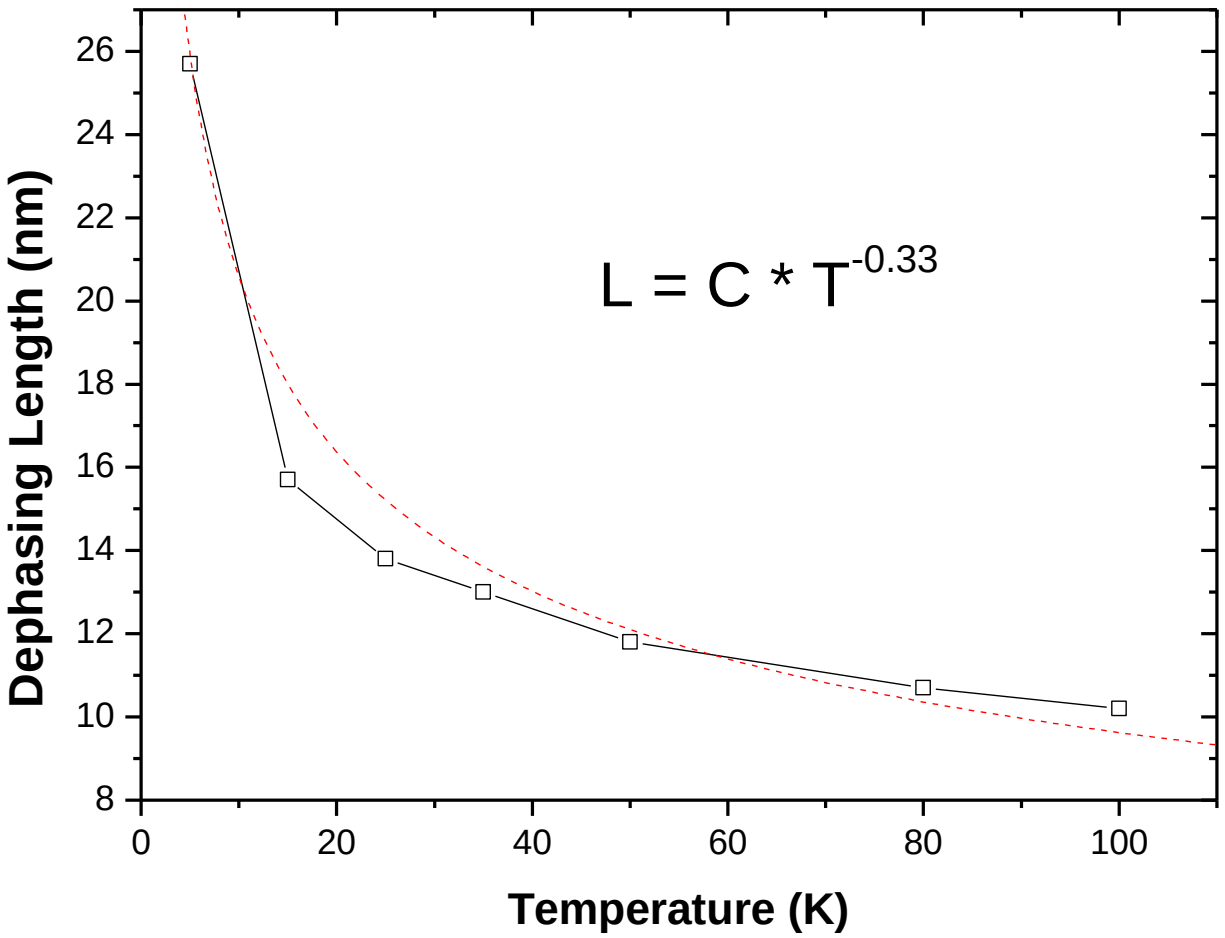


Fig 5.22: *A graph of the Dephasing length vs. Temperature for the 22% HFCVD-N_2 films.*

Figure 5.22 shows that the temperature dependence of the dephasing length is approximately $L_\phi \sim T^{-0.33}$; this is 0.02 less than that obtained during the R-T analysis. Therefore within experimental limits we can thus conclude that 3D weak localization model with anisotropic corrections is appropriate to describe the behavior of our films.

5.7 Results and analysis for the 20% MWCVD-N_2 films

In this section we present the results for the microwave (MWCVD-N_2) synthesized nanodiamond films.

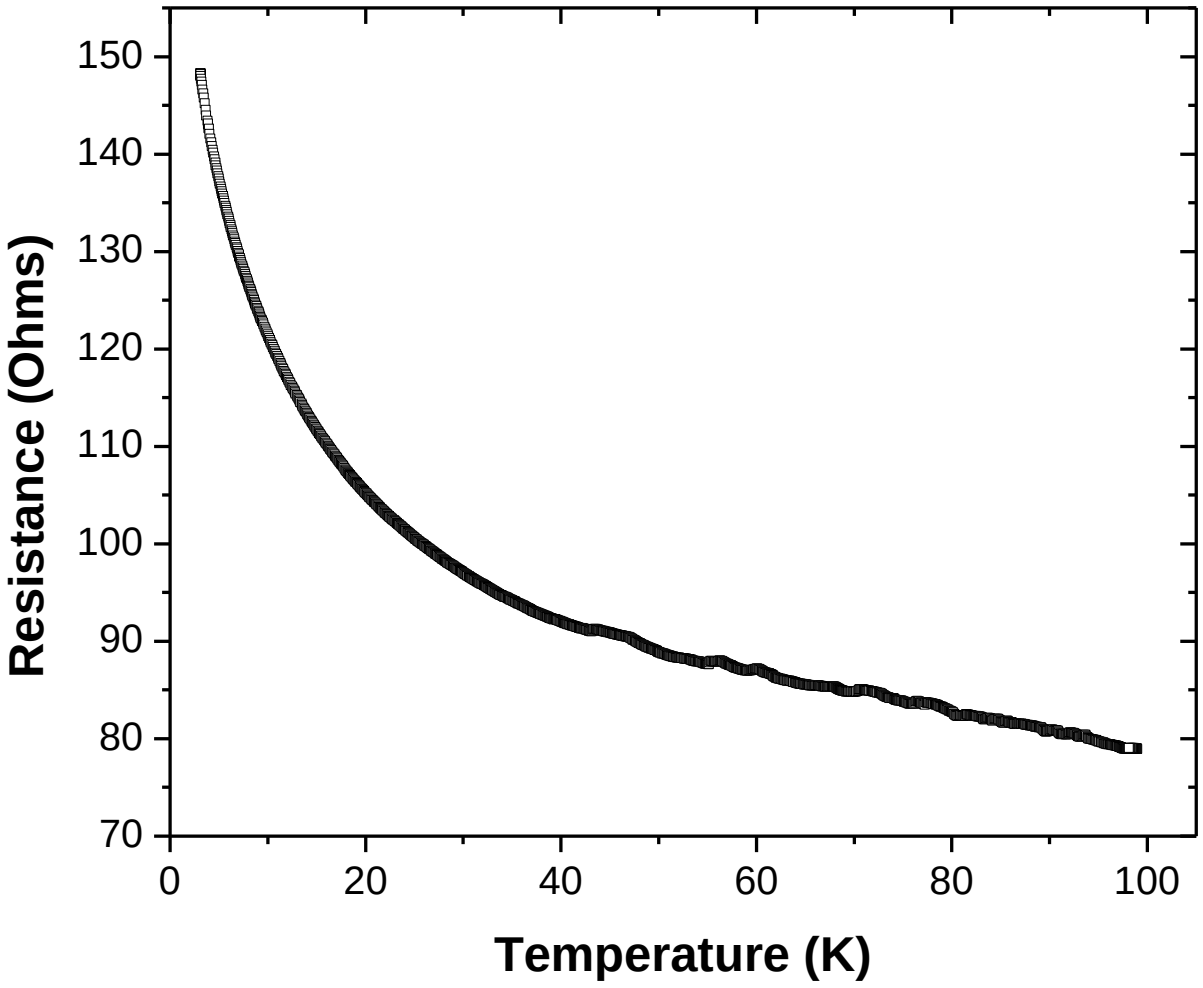


Fig 5.23: *A graph showing the Resistance- Temperature variations below 100K for 20% MWCVD-N_2 films.*

Figure 5.23 shows an increase of resistance with a decrease in temperature and this is expected for a non-metallic or semiconducting material. Decreasing the temperature to values as low as 2.3 K means that we have reduced significantly phonon effects and we might possibly notice wavefunction shrinkage and localization of electron states depending on the level of disorder in the material. All these processes might be possible explanations to the increased resistance at low temperature. However to be able to determine the transport mechanism we need to do an analysis of these results using several transport models as already stated in subsection 5.5 during the analysis of the HFCVD-N_2 films.

In this section we check for the relevance of the variable range hopping mechanism.

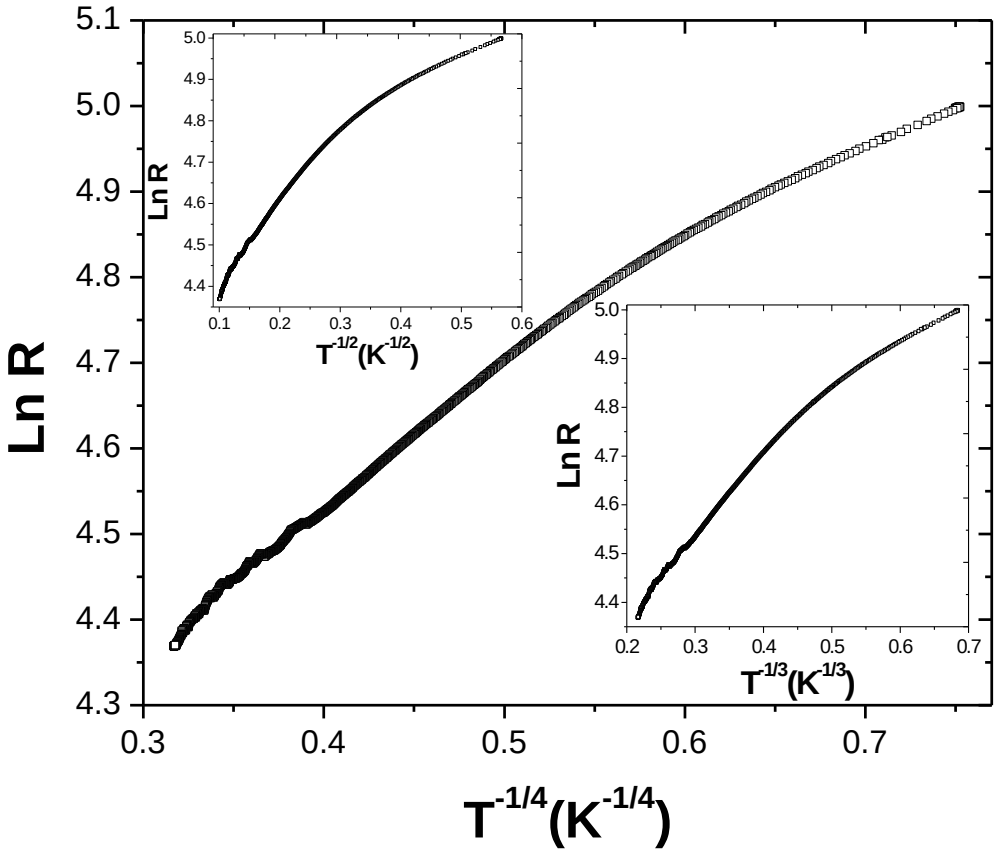


Fig 5.24: *A graph showing the 1D (top-left insert), 2D (bottom-right insert) and 3D VRH fittings for the 20% MWCVD-N_2 films.*

The non linearity in the graph above (Fig 5.24) and the inserts (1D VRH top insert and 2D VRH bottom insert) indicates that VRH is not an appropriate transport mechanism in these nanodiamond films. We observe a deviation which is more pronounced at low temperatures. This indicates that we do not have much strongly localized states in our system (i.e. Hopping) and hence the need to carry out further investigations.

As we have observed earlier, VRH is not an appropriate conduction mechanism. We then try the model on weakly localized transport which is a precursor to strong localization. In weakly disordered systems the conductivity has two quantum corrections (i.e. weak localization corrections and electron-electron interactions) to the classical conductivity as earlier highlighted (see section 5.4). These contributions are in total less than 10% of the classical component; however at low temperatures these contributions are significant and are worth considering. From the insert of Fig 5.25 it is clear that the 2D weak localization model is not an appropriate mechanism for this sample. A linear behavior on a significant low temperature range would have been expected for the material; furthermore we are not in a position to observe electron-electron interactions because the sample length (1.2×10^{-2} m) is far much greater than the Thouless length, (defined as the distance over which impurity scattering is treated coherently, mathematically it is a product of the elastic and inelastic scattering lengths)

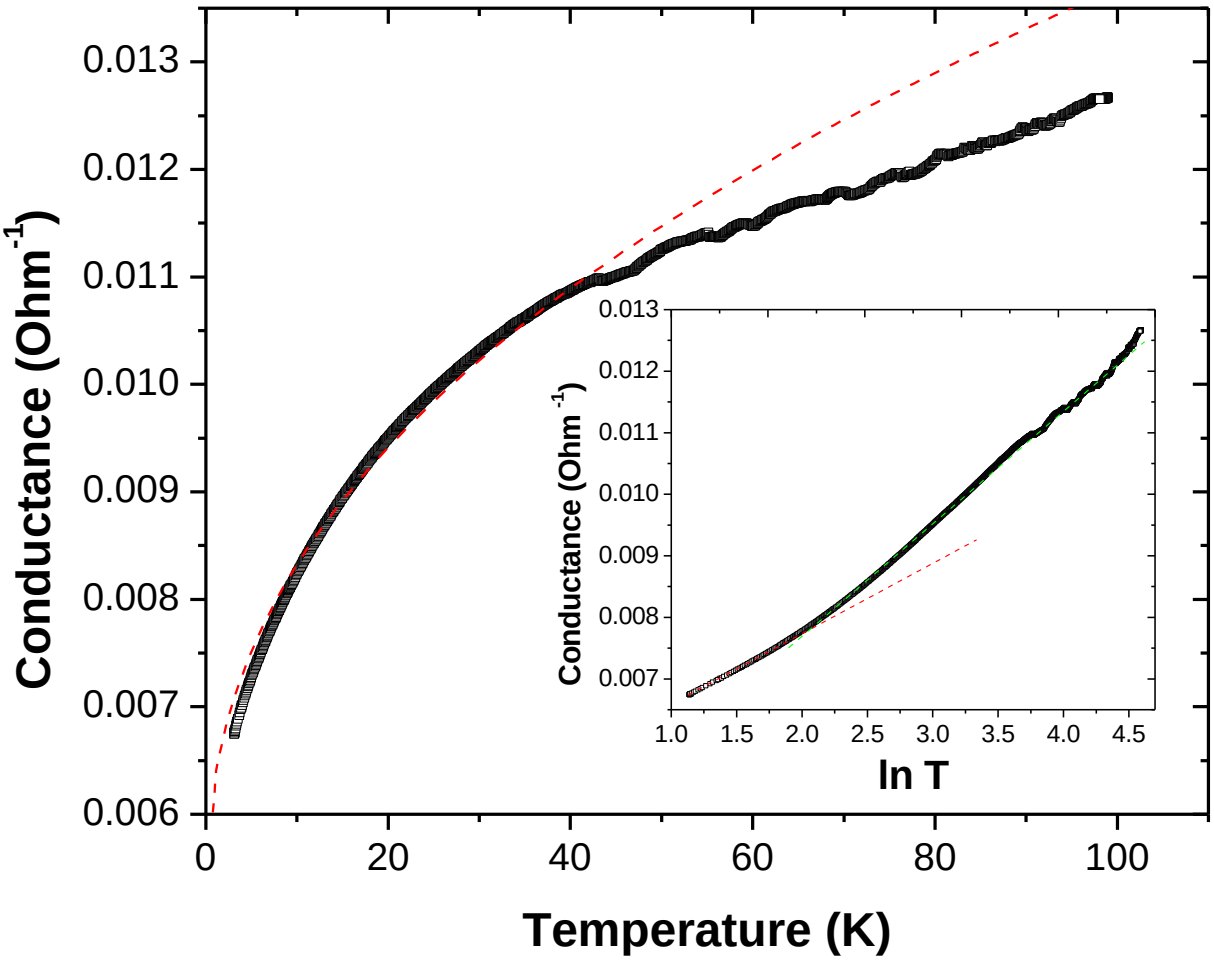


Fig 5.25*: A graph of conductance vs. temperature to verify 3D WL in the 20% MWCVD-N_2 Films. The insert is a graph of Conductance vs. ln T graphs to check for 2D WL in 20% MWCVD-N_2 films.*

Figure 5.25 is the temperature dependence of the conductance which has been fitted with 3D weak localization and electron- electron interaction corrections. It is quite evident from the graph that the model better fits at low temperatures with some deviations as the temperature is increased to above 50K. From the fitting of the graph with equation (4) and using equation (7) and (8) (see section 5.4) we obtain the fitting parameters which are given below. We will thus focus on the low temperature region for now.

$a_1 = 7.5 \times 10^{-4} = {e^2}/{2\pi^2 \hbar L_\phi}$ $(\frac{C^2}{kg}\frac{S}{m^3})$

$a_2 = 5 \times 10^{-4} = \left(\frac{e^2}{4\hbar\pi^2}\right)\left(\frac{1.3}{\sqrt{2}}\right)\left(\frac{4}{3}-\frac{3}{2}F\right)\sqrt{{k_B}/{\hbar D}}$ $(\frac{C^2}{kgm^4}\frac{s}{k^{0.5}})$

$G_o = 0.0051$ (Ohm^{-1})

The fitting parameters above, enables us to calculate the diffusion coefficient (D) and the temperature dependence of the dephasing length (L_ϕ).

$D \approx 5.12 \times 10^{-7}$ m^2s^{-1} if we take F = 0.3 as explained earlier.

The temperature dependence of the dephasing length is given by

$L_\phi \approx 4.87 \times 10^{-9}\ T^{-0.35}$ (m)

An estimation of the localization length can be found using the equation below

$$L_c = ({hD}/{2\pi k_B T})^{0.5} \text{ (m)} \qquad (14)$$

Using the value of D obtained above and taking T at the lowest recorded temperature we get

$L_c \approx 0.44$ nm

This value is very much smaller than the sample length which indicates that 3D electron–electron interactions play an important role in this analysis and cannot be ignored. The 3D weak localization contribution to the conductivity is expressed in another form as

$\Delta\sigma = a_3 T^{P/2}$ the index *P* is an important parameter which depends on the scattering mechanism in the film.

From the temperature dependence of our L_ϕ, it implies that *P* = 0.7, a value less than unity and cannot be explained in terms of 3D WL isotropic case. This value is less than that expected in

bulk dirty metals where p > 1. Such a value has been quoted in superlattice structures where tunnel transport is predominant [**44, 50**].

(b) MR Results for 20% MWCVD-N_2 films

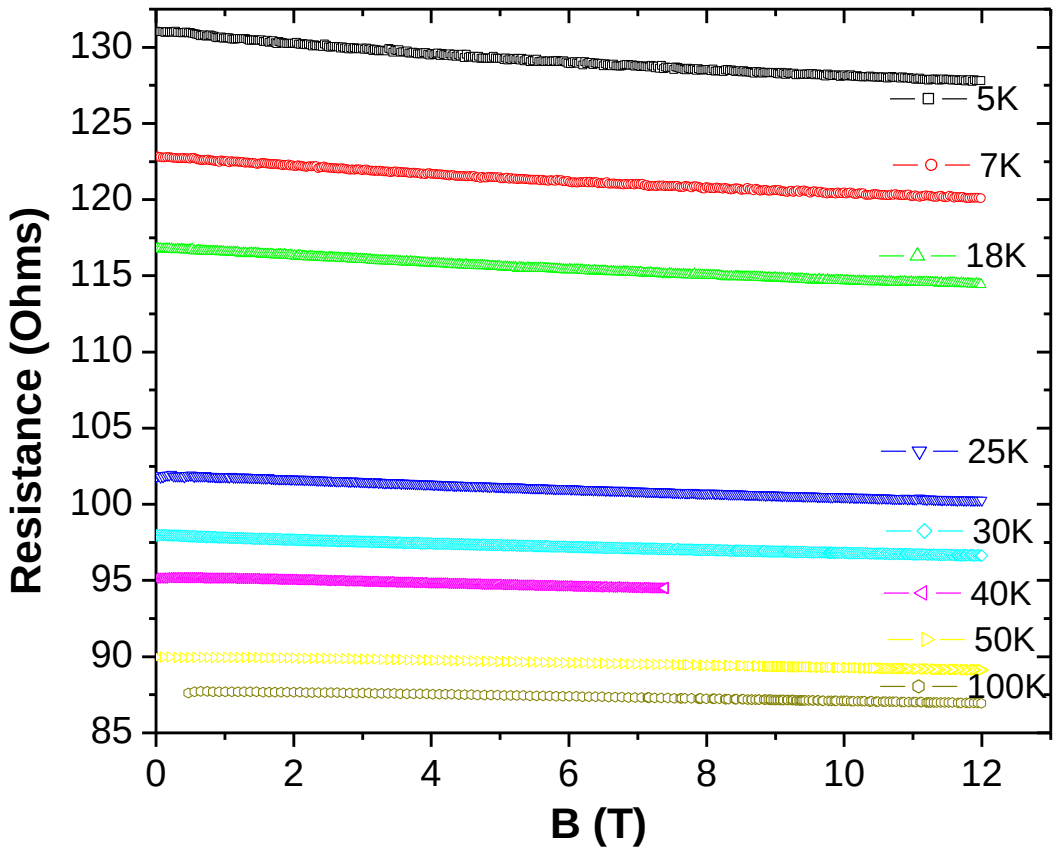


***Fig 5.26**: Resistance vs. Magnetic field plot for 20% MWCVD-N_2 films.*

Fig 5.26 indicates clearly that the magnetoresistance is purely negative and the relative extent of the negativity decreases with the increase in temperature. A negative MR in the whole range suggests a weak localization transport model. The negative MR is probably due to weak localization in our MWCVD-N_2 films. To better analyze our results we normalize the data and extract the resistance from the MR data.

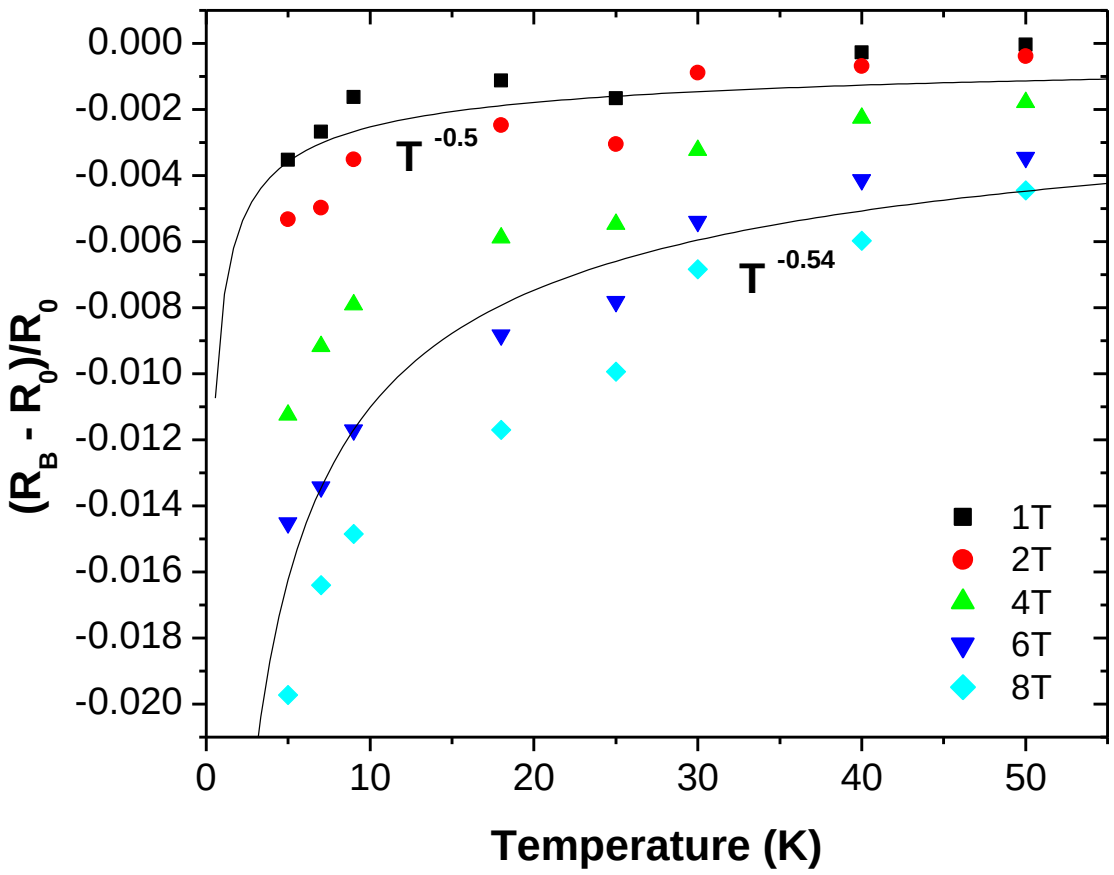


Fig 5.27: *A graph of $\Delta R/R_0$ vs. sample temperature for the 20% MWCVD-N_2 films at various fields.*

Figure 5.27 above shows the temperature dependence of MR at various magnetic fields. As indicated in the graph we observe $T^{-0.5}$ dependence which is still a weak field dependence as was shown in the R-T analysis. The $T^{-0.5}$ dependence is more pronounced at low field than at high field.

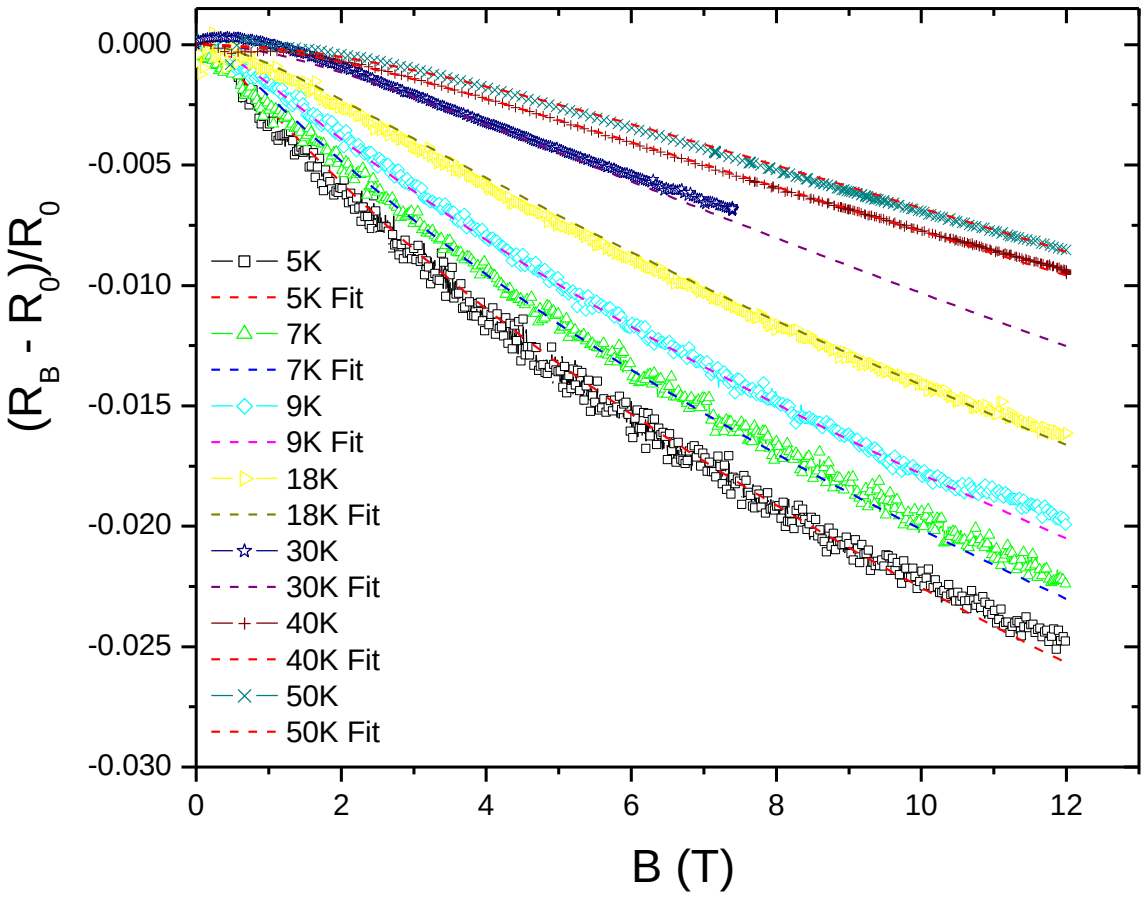


Fig 5.28: *Normalized MR results with the 3D WL anisotropic fitting for 20% MWCVD-N_2 films.*

We now attempt to test the 3D weak localization model in anisotropic systems. The isotropic model was found to be inappropriate. Fig 5.28 shows that the MR data fitted well with the anisotropic model. At low temperatures the anisotropic coefficient for our model is $\alpha = 1.35$, this value is lower than the reported value of 3 [**43**]. This might be due to the fact that the magnitude of anisotropy in materials differs as this is heavily dependent on the film structure, which depends on the synthesis method.

From the fittings of the MR data with the anisotropic model we obtain the dephasing length (L_ϕ) and its temperature dependence is an indication of the main conduction mechanism. The graph below shows the temperature dependence of this parameter.

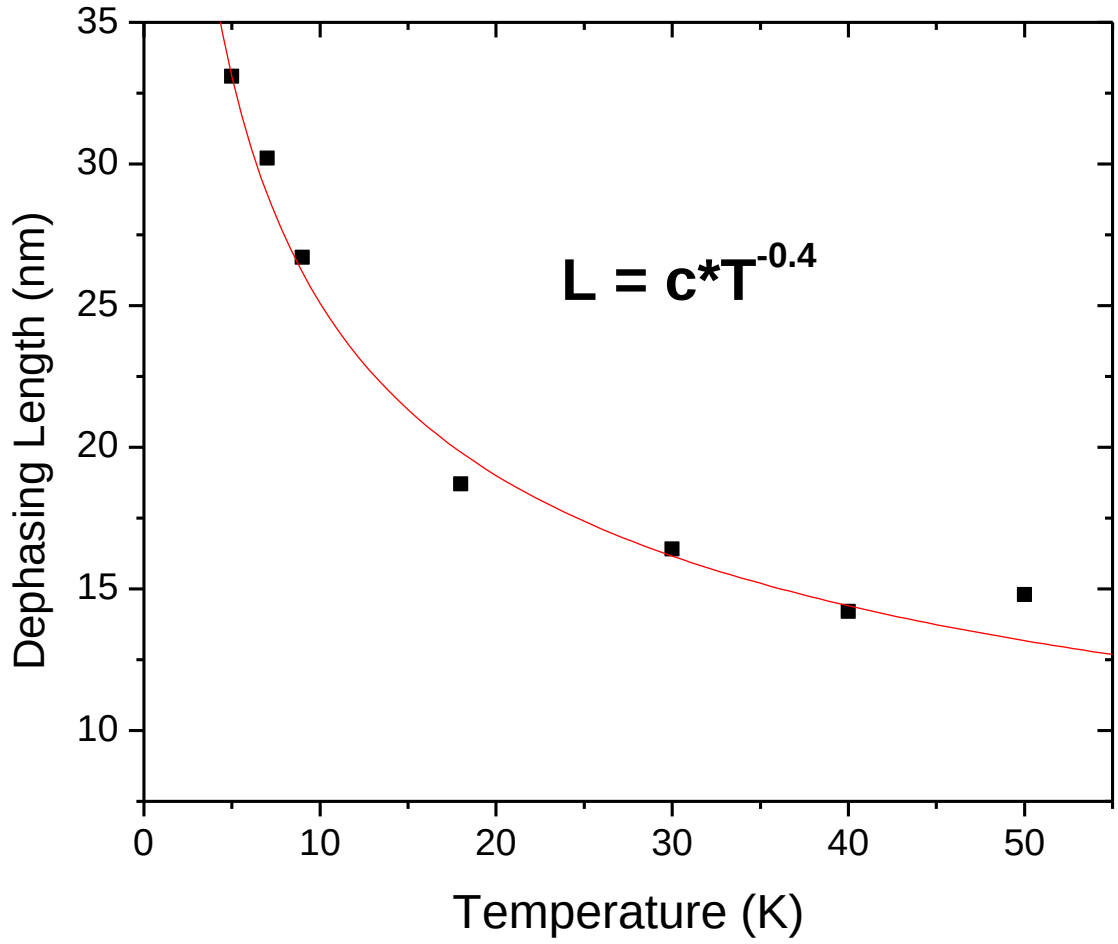


***Fig 5.29**: A graph of the temperature dependence of the dephasing length for the 20% MWCVD-N_2 films*

The temperature dependence of the dephasing length which is obtained from the graph above (Fig 5.29) is $L_\phi \sim T^{-0.4}$ this implies that the value of $p = 0.4$, which is 0.05 more than that obtained in the R-T analysis. We therefore can conclude that this 3D weak localization model with anisotropic corrections is the most appropriate mechanism in the 20% MWCVD-N_2 films. The model is similar to the quasi 2D conductivity observed in artificial superlattices. The high free electrons in the material induce electron-electron interactions which modify the conductivity

significantly at very low temperatures with a temperature dependence of $T^{-0.5}$ as suggested by other researchers [**51**].

5.8 Results and analysis of the MWCVD-N_2 10%

We now turn our attention to the results of the 10% nitrogen doped films. Fig 5.30 shows the conductance and (insert) Resistance - Temperature dependence.

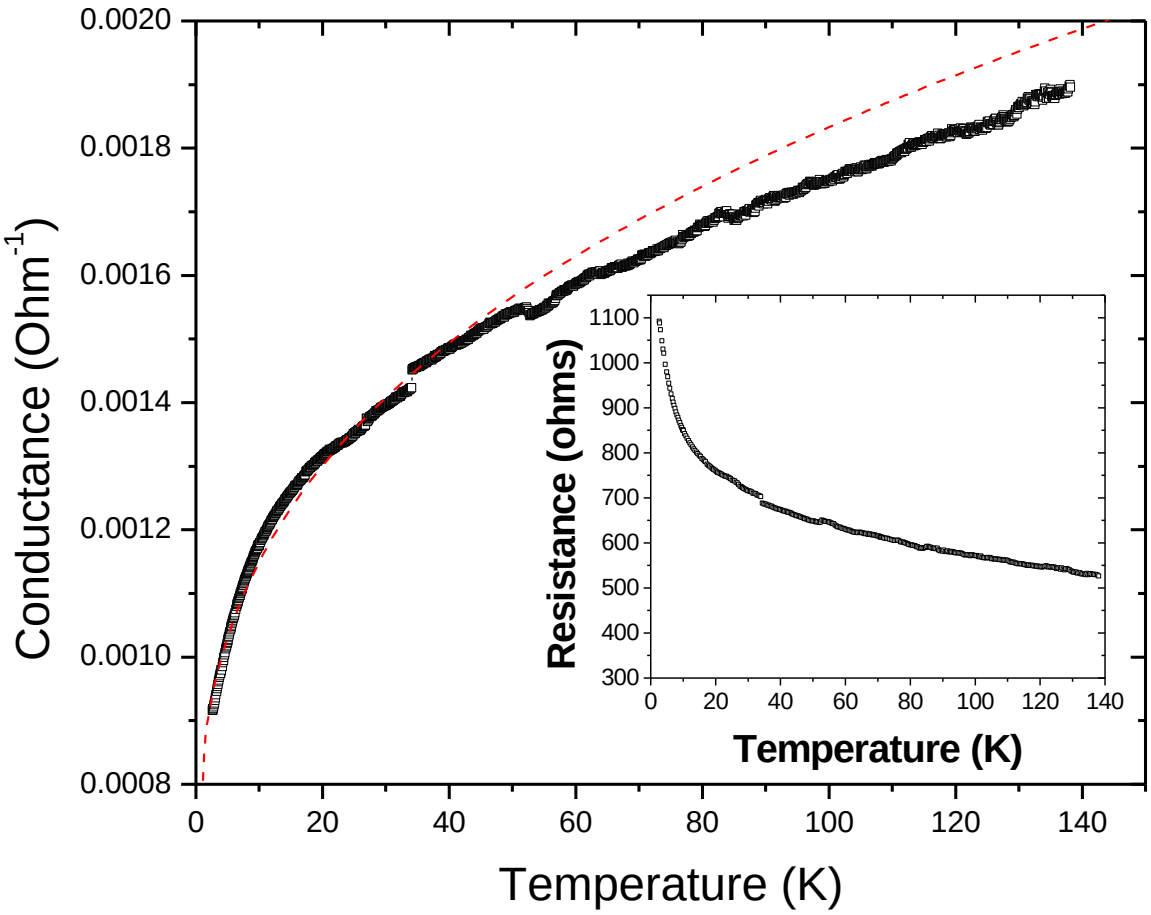


Fig 5.30: *Conductance vs. temperature graph with 3D weak localization fit correction. The insert shows the resistance vs. temperature for the 10% MWCVD-N_2 films.*

As was observed in the 20% MWCVD-N_2 films the resistance increases with a decrease in temperature. The only obvious difference is in the absolute value of the resistance, with the

10% MWCVD-N_2 having higher values as expected. A closer look however, at the R-T measurements and the corresponding analysis we observe slight differences. The graph, Fig 5.31 shows the fitting curves for VRH in the three dimensions.

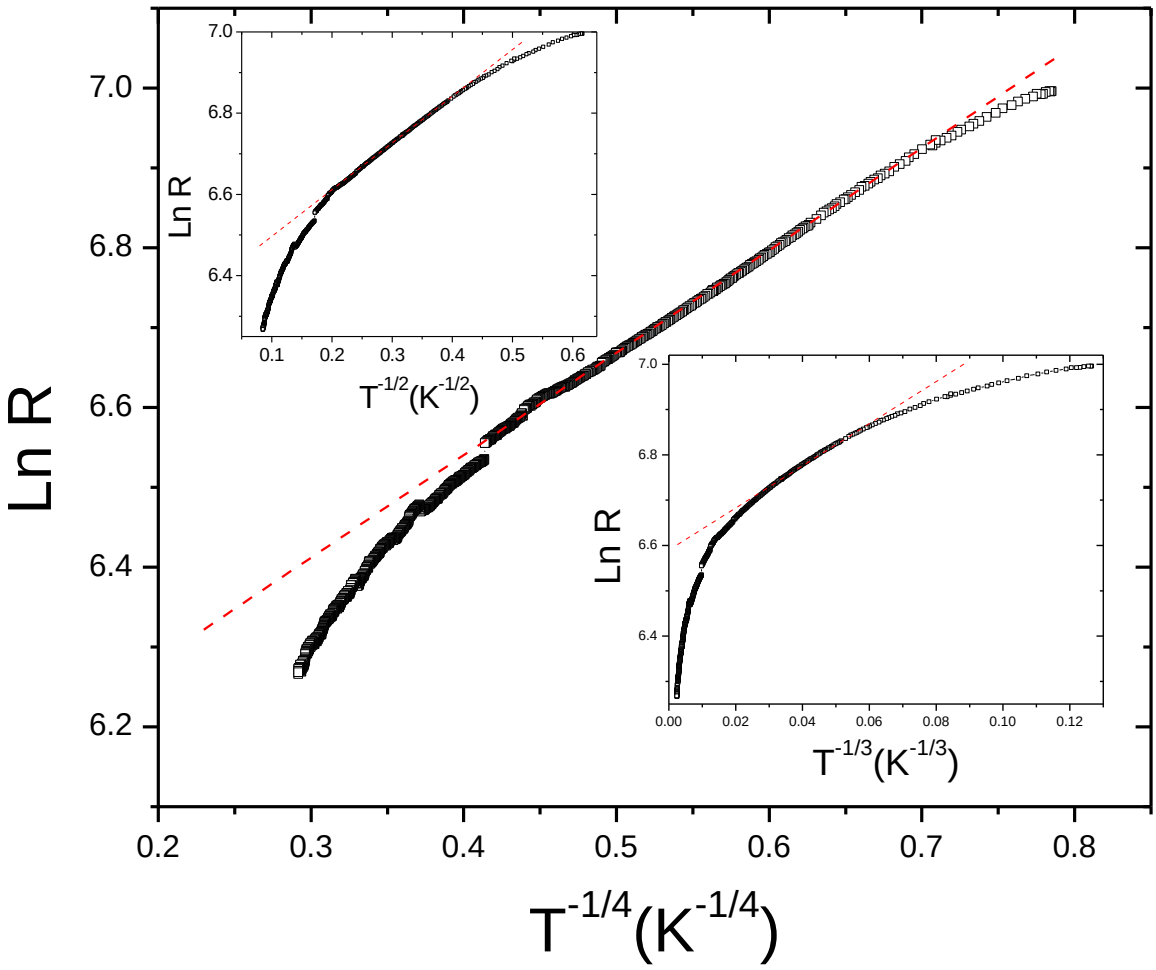


Fig 5.31: *A graph showing 1D (Top insert), 2D (bottom insert) and 3D VRH in 10% MWCVD-N_2 films.*

From the graph (Fig 5.31) and the inserts we can see that 1D and 2D VRH are not appropriate conduction mechanisms in the film. The 3D VRH is not appropriate at very low temperatures but at intermediate temperatures it fits very well suggesting the possibility of hopping conductivity at intermediate temperatures. This trend is however not applicable through the

entire/broad range meaning that this mechanism is not the major contributor to the conduction. It nevertheless has a minor contribution unlike the case in the 20% MWCVD-N_2 films in which we did not observe VRH. The reason for this is as yet unresolved and further investigations are required.

To try and explain the conduction mechanism in the low temperature region we check the weak localization model proposed previously in the 20%, where there is an additional correction to the classical conductivity by incorporating electron-electron interactions (See equation 3). Fig 5.30 shows the fitting of this model on the Conductance - Temperature graph. It is clear that the model fits very well at low temperatures and partially at intermediate temperatures.

As can be seen that we do not have a model that can describe the whole temperature range, the weak localization model is not the best but it is a better model at low and intermediate temperatures. Fitting the conductance- temperature graph with equation (6) we obtain fitting parameters to be:

$$a_1 = 2.44 \times 10^{-5} \left(\frac{C^2}{kg}\frac{S}{m^3}\right)$$

$$a_2 = 1 \times 10^{-4} \left(\frac{C^2}{kgm^4}\frac{s}{k^{0.5}}\right)$$

$$G_o = 0.0006 \ (\text{Ohm}^{-1})$$

Which gives us $D = 5 \times 10^{-7} \ m^2s^{-1}$ and

$$L_\phi \approx 9.91 \ x \ 10^{-9}T^{-0.35} \text{(m)}$$

when *F* is taken to be 0.3 and using equation (6), (7) and (8).

The localization length at the lowest temperature is estimated to be

$$L_c \approx 1.17 \text{ nm.}$$

(a) MR Results for 10% MWCVD-N_2 films

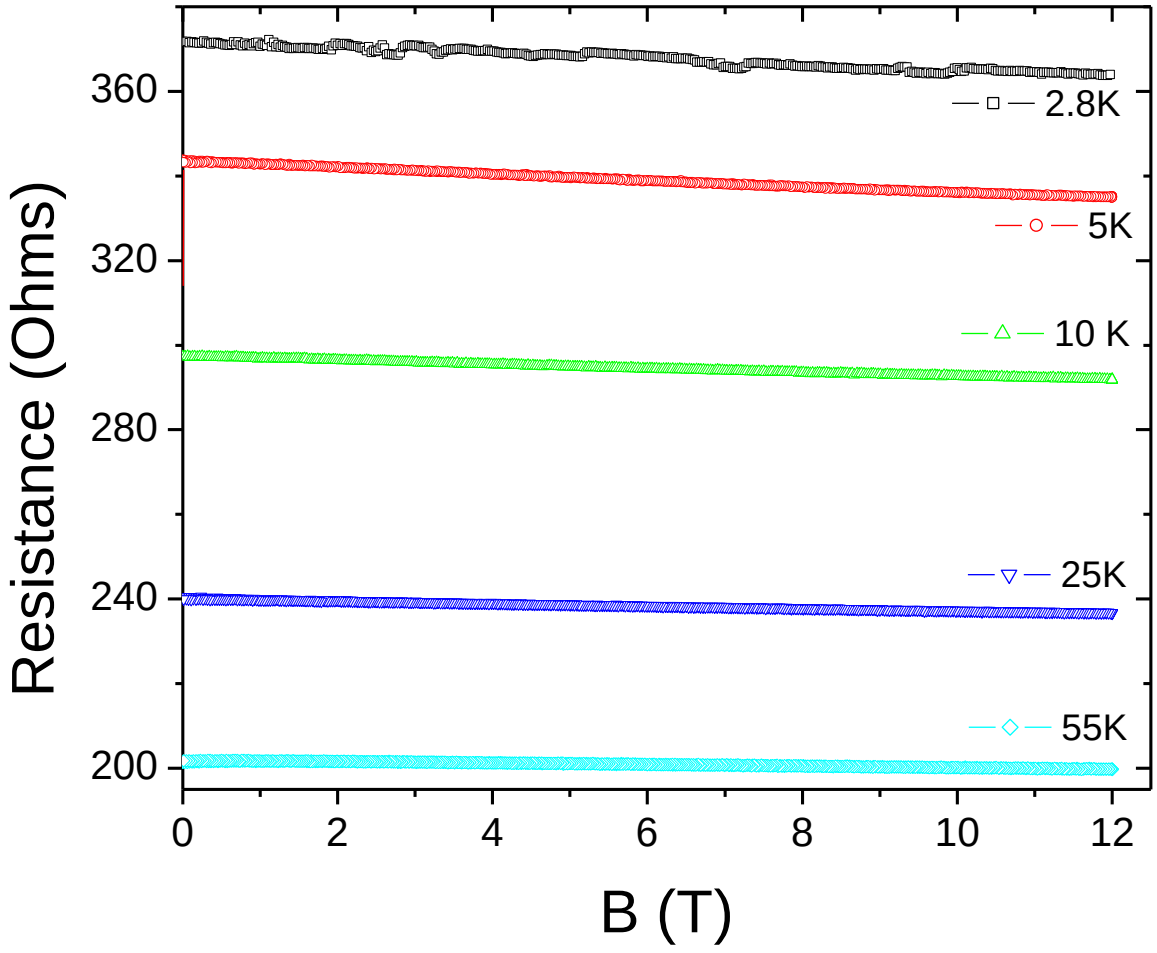


Fig 5.32: *A graph of the resistance vs. magnetic field for 10% MWCVD-N_2 films.*

As observed earlier in the 20% films, we observe a similar trend in the MR results. Pure negative MR at high fields which is parabolic (B^2)at very low fields. The B^2 dependance is not clear using this scale, normalizing the MR results however, shows this behaviour clearly as indicated by Fig 5.33. We now try and confirm the 3D weak localistion model for this MR data. Using the anisotropic model we fit the normalized MR data.

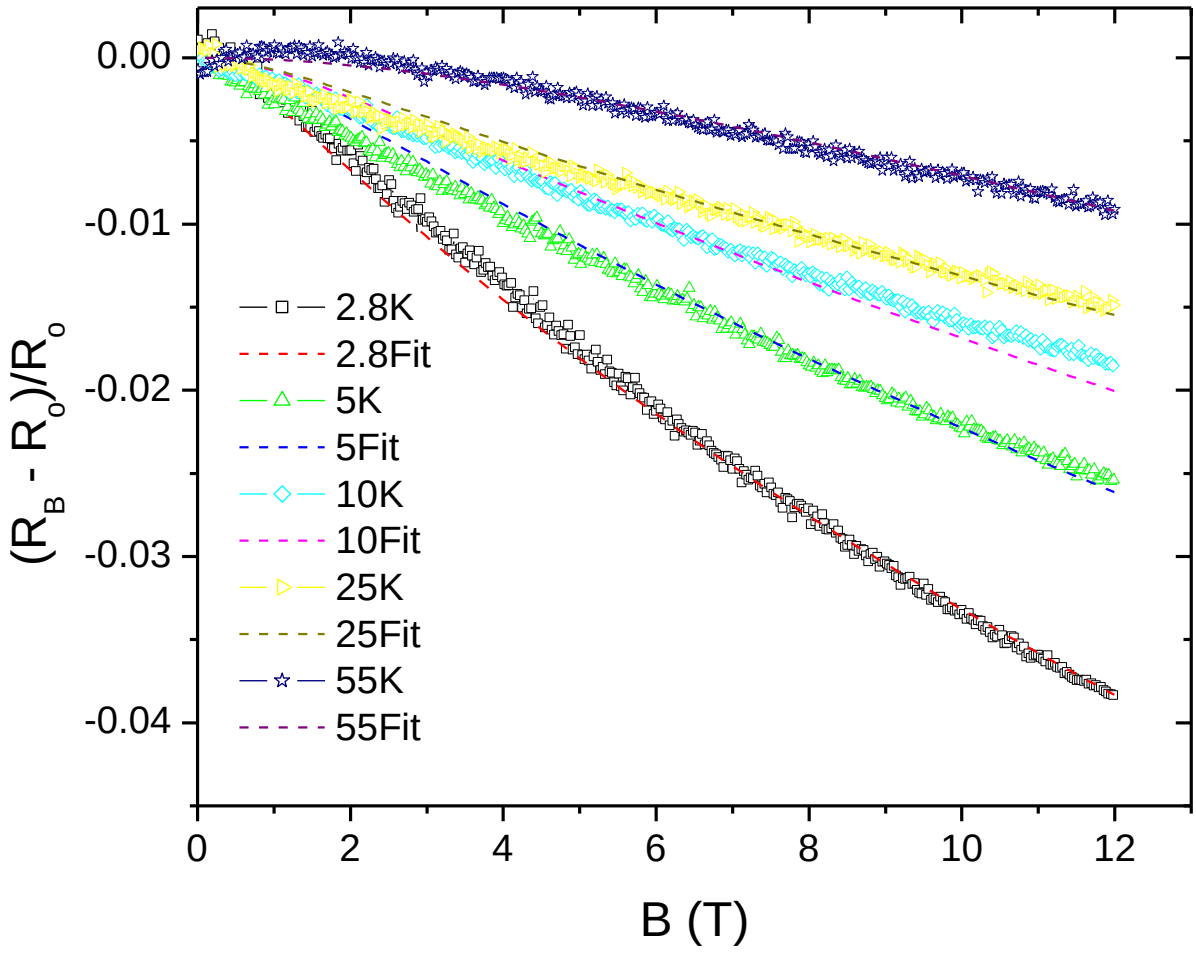


Fig 5.33: *Normalized MR results for 10% MWCVD-N_2 with the 3D WL anisotropic fitting.*

From Fig 5.33, it is evident that the model is very appropriate and fits perfectly well at higher magnetic fields than it does at low fields. The anisotropic coefficient for this sample is found to be 2.7 which is slightly less than that reported in artificial superlattice structures. This means that 10% films are more directional sensitive compared to the 20% films and the reason might not be due to the nitrogen content but maybe due to structural differences in the diamond lattices. This is in agreement with other reports which have said that anisotropic behavior is less

pronounced in highly conducting films and more in insulating films [**52**]. From the fitting curves we thus calculate the dephasing length and determine its temperature dependence.

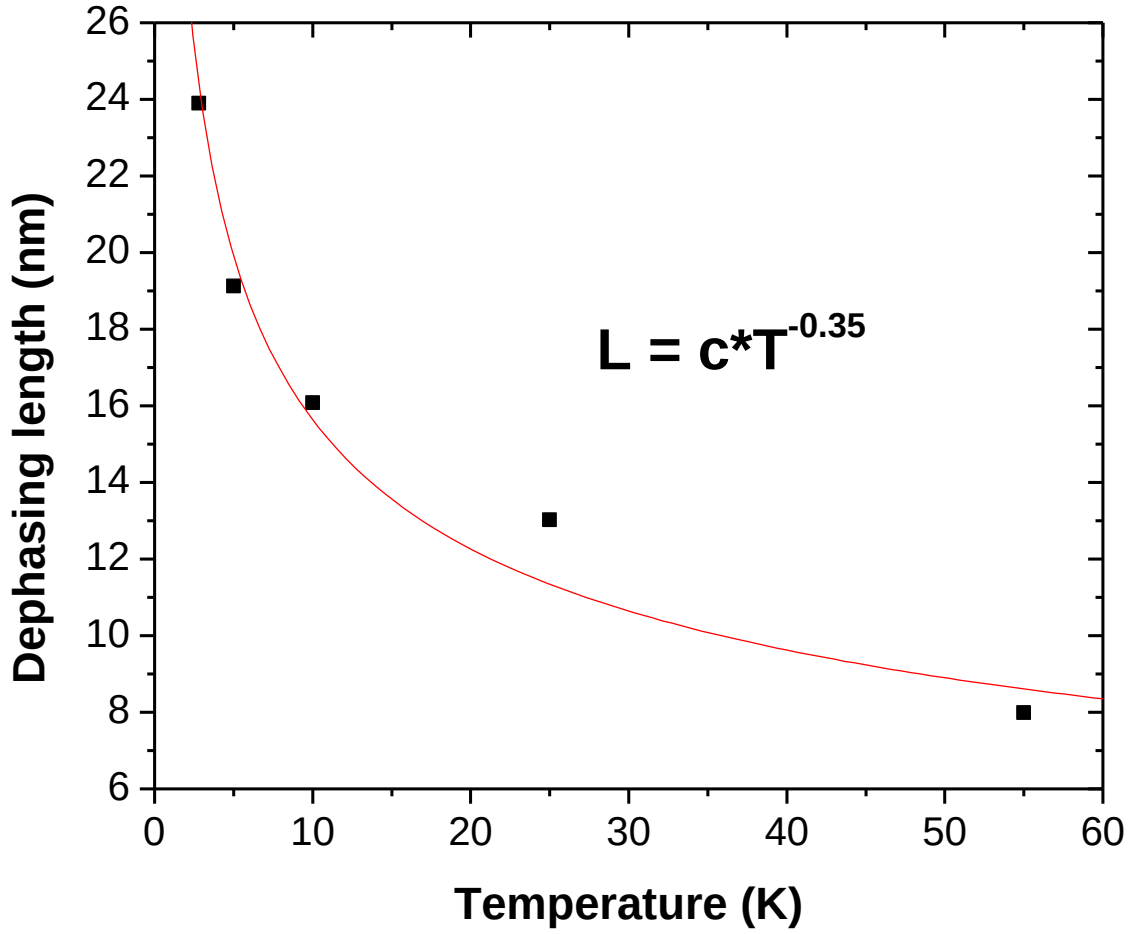


Fig 5.34: *Dephasing length vs. sample temperature to determine its temperature dependence for 10% MWCVD-N_2 films.*

From Fig 5.34 the temperature dependance of the dephasing length is $T^{-0.35}$, this behaviour corresponds to that obatined in the R-T results. Hence we can conclude that 3D weak locazation model with some electron-electron interaction is a more appropriate model for these 10% films. The films have a higher degree of anisotropy (with $\alpha = 2.7$) than the 20% MWCVD films which at present is attributed to the structural differences in the films.

5.9 Electrical conductivity in nanodiamond films- Conclusion

In conclusion to Chapter 5 we summarize the main points made from the study of electrical transport in nitrogen doped HFCVD and MWCVD nanodiamond films. We have observed that the conduction in these films cannot be described by one model in the entire temperature range. In the intermediate temperature range, the conduction for the 20% HFCVD-N_2 films is typical of semiconductors where thermal activation predominates, while in the 22% HFCVD-N_2 films we have semi-metallic behavior in which 3D WL is the dominate process. The activation energy for the 20% HFCVD-N_2 films was found to be approximately 18.2 meV. As explained earlier this suggests the presence of an impurity band below the conduction band. At higher temperatures a different semi-metallic mechanism is observed which is similar to that observed in MWCVD films and the more conducting 22% HFCVD-N_2 films. The electron mobility is diffusive and the correction to the Drude conductivity is made up of two quantum contributions, namely the weak localization and the electron-electron interactions. The later part however is more pronounced in the MWCVD-N_2 films at very low temperatures. This we attribute to the high electron density in the films, although still lower than in metallic materials it makes a significant contribution to the transport properties.

The dephasing length has been found to be weakly temperature dependant with a variation in T from $T^{-0.33}$ to $T^{-0.35}$. This by definition gives a temperature dependence of the dephasing time double that of the corresponding length. Such behavior will give longer dephasing time in these films a property which might help to realize these films in fast electronic devices. A temperature dependence of 0.7 for the dephasing time has so far to our knowledge been reported only in artificial superlattices [**44, 50**].

Unlike other carbon allotropes, nanodiamond films have shown to have some anisotropic property, which is believed to be due to anisotropic distribution of disorder in the grain boundaries. When fully understood this behavior would usher these novel materials in magnetic sensors and other related electronic devices. While the electronic properties of nanodiamond films are very sensitive to the synthesis process, we have however shown that it is possible to a certain degree to produce films by two different methods and still maintain the

fundamental transport properties. Our magneto-resistance measurements in the low and intermediate range bear testimony to that.

Chapter 6

Electronic Transport in Iron filled MWNT's (Fe-MWNT)

6.1 R-T results for the 5% and 27% iron filled MWNT samples compared

In an effort to try and understand the contributions from sp^2 phases in the grain boundary, we studied the electronic transport in iron filled multiwalled carbon nanotubes (Fe-MWNT). In this chapter we give the outcome of this analysis for samples with different iron content, one had approximately 5% iron and other about 27% iron. The iron content was established using thermal gravitational analysis (TGA). The synthesis was done by one of our group members based in the chemistry department.

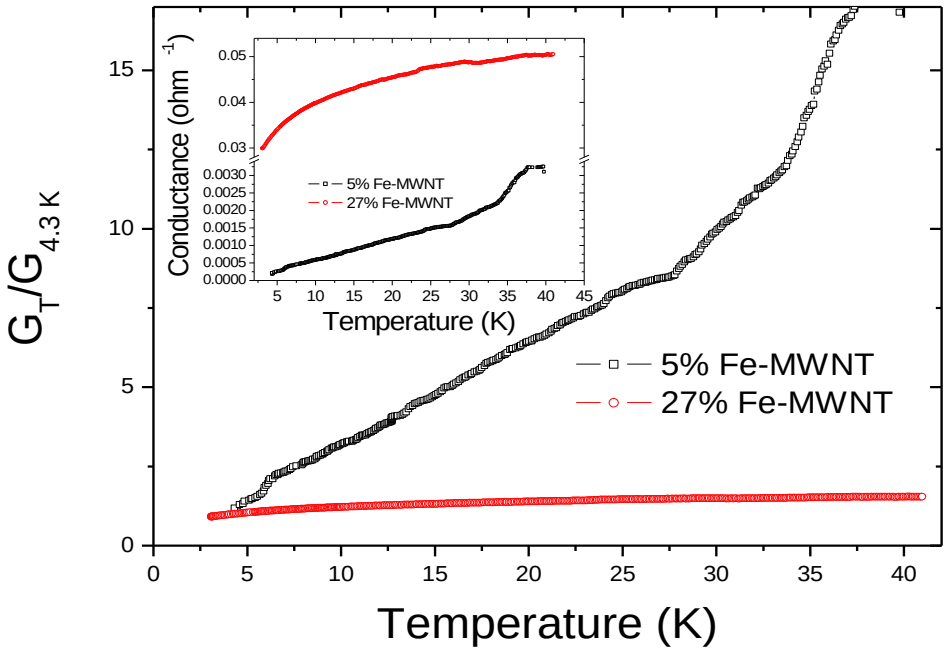


Fig 6.1: *Conductance -Temperature dependence of the two Fe-MWNT Samples compared from 4.3K.The insert shows unnormalized conductance results.*

Figure 6.1 indicates an increased conductance in the 27% Fe-MWNT compared to the 5% Fe-MWNT. The rapid increase in the conductance with temperature for the 5% sample suggests a semiconducting behavior. However from these results only, we are not able to determine the conduction mechanism in the material, to do this we need some analysis using known conduction models in disordered systems as discussed earlier. In chapter 5 we have already talked about the variable range hopping and the analysis thereof. We will try to examine if this model is appropriate for the conduction in iron filled multiwalled carbon nanotubes. But before we do that we will briefly talk about magnetoresistance in strongly localized systems.

6.2 Magnetoresistance in strongly localized regime of disordered systems

We indicated in chapter two that localization can be strong or weak. In strongly localized disordered materials the MR is often seen increasing with magnetic field (i.e. positive MR) this is due to shrinking of the electron orbital's which results in the hopping probability decreasing and hence increase in resistance. This kind of behavior was modeled by W. Schirmacher using the equation (15), below

$$ln\left(\frac{\rho_B}{\rho_o}\right) = \left(\frac{5e^2}{2016\hbar^2}\right)L_c r^3 B^2 \qquad (15)$$

Where *ρ, e, B* and $\hbar$ have their usual meanings (see list of symbols), L_c is the localization length and r is the hopping distance [**53**].

In some materials, MR is observed to decrease with increasing magnetic field (i.e. negative MR); this is a special quantum mechanism in which constructive forward interference of different electron's hopping paths results in a decrease of resistance when we introduce a magnetic field. This is modeled using the equation (16), below.

$$ln\left(\frac{\rho_B}{\rho_0}\right) = N(rL_c)^{\frac{3}{2}} r^2 \left(e/\hbar\right) B \qquad (16)$$

The above two processes were observed in our samples and they are additive, especially at low temperatures giving the equation (17), below

$$ln\left(\frac{\rho_B}{\rho_0}\right) = -a_1 B + a_2 B^2 + a_3 \qquad (17)$$

where $a_1 = N{L_c}^5 \left(\frac{T_0}{T}\right) 1^{P1} (^{e}/_{\hbar})$, $a_2 = \left(\frac{5e^2{L_c}^4}{2016h^2}\right) (\frac{T_o}{T}) 1^{P2}$ and a_3 accounts for the complex behavior at low fields [**50**].

P1 = $^{7}/_{8}$ in Mott VRH and $^{7}/_{4}$ in E-S model , *P2* = $^{3}/_{4}$ in the mott VRH and $^{3}/_{2}$ in the E-S model.

We shall use equation (17), to analyze the MR data in section 6.4, but for now we investigate the R-T results.

6.3 Analysis of 5% FE-MWNT sample

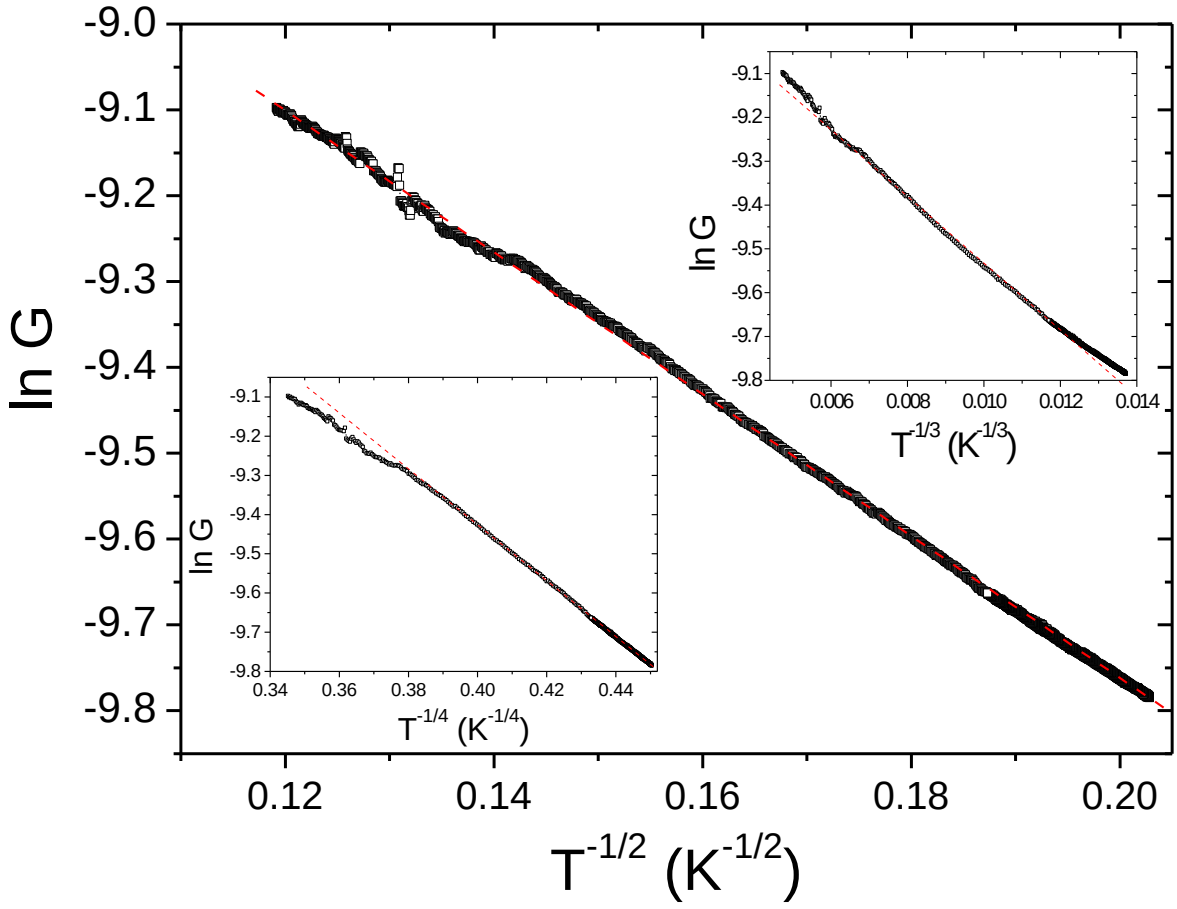


Fig 6.2: *ln G vs. $T^{-1/2}$ to check for Coulomb gap VRH mechanism in the 5% Fe-MWNT sample. Top insert is for ln G vs. $T^{-1/3}$ (2D VRH) and bottom insert is for ln G vs. $T^{-1/4}$(3D VRH).*

The graph (Fig 6.2) shows us that the plot of ln G vs $T^{-1/2}$ is the better fit graph when compared to $T^{-1/3}$ and $T^{-1/4}$ (top and bottom inserts respectively). This would suggest that we have 1D VRH in our sample. However, considering the dimensions of our measured sample (see Appendix B) and the fact that it's a network of MWNT, 1D VRH does not make any logical sense. This $T^{-1/2}$ dependence of ln G can thus be explained according to E-S model in 3D systems where there is a Coulomb gap. Efros and Shkolovskii et al suggested that in the presence of a Coulomb gap

(due to electron- electron interactions) the density of states is reduced near the Fermi level which reduces the temperature dependence of the conductance [**47**].

MR Results for the 5% Fe-MWNT sample

Fig 6.3 below indicates that at the lowest recorded temperature (2.5 K), MR is purely positive, while the 5 K and 10 K have negative components at low fields which turn to positive at high fields. At higher temperatures the MR is purely negative.

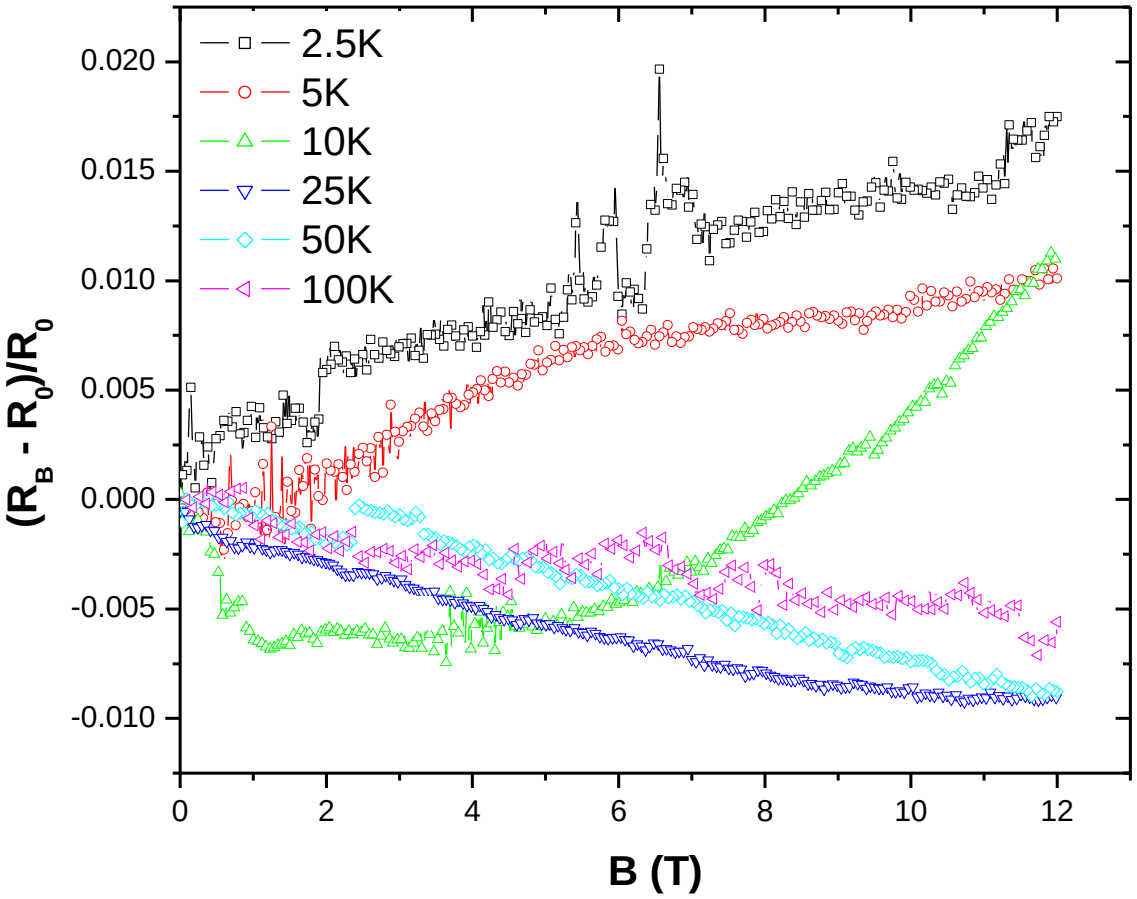


Fig 6.3: *Normalized MR results for 5% Fe-MWNT sample indicating both positive and negative MR.*

A closer analysis of the graph (Fig 6.3) we observe that there is an increase with temperature of the characteristic field (B_c) at which we observe an upturn to positive MR. At 2.5 K this field is

almost zero, while when T is 5 K, B_c is about 2.8 T, when T = 10 K, B_c is about 4.3 T and when T= 25 K, B_c is approximately 10.5 T. At higher temperatures we do not observe this upturn; it is only dominant at low temperatures. This is due to the fact that we begin to have increased phonon interactions which results in the suppression of the mechanism.

6.4: Analysis of 27% Fe-MWNT sample

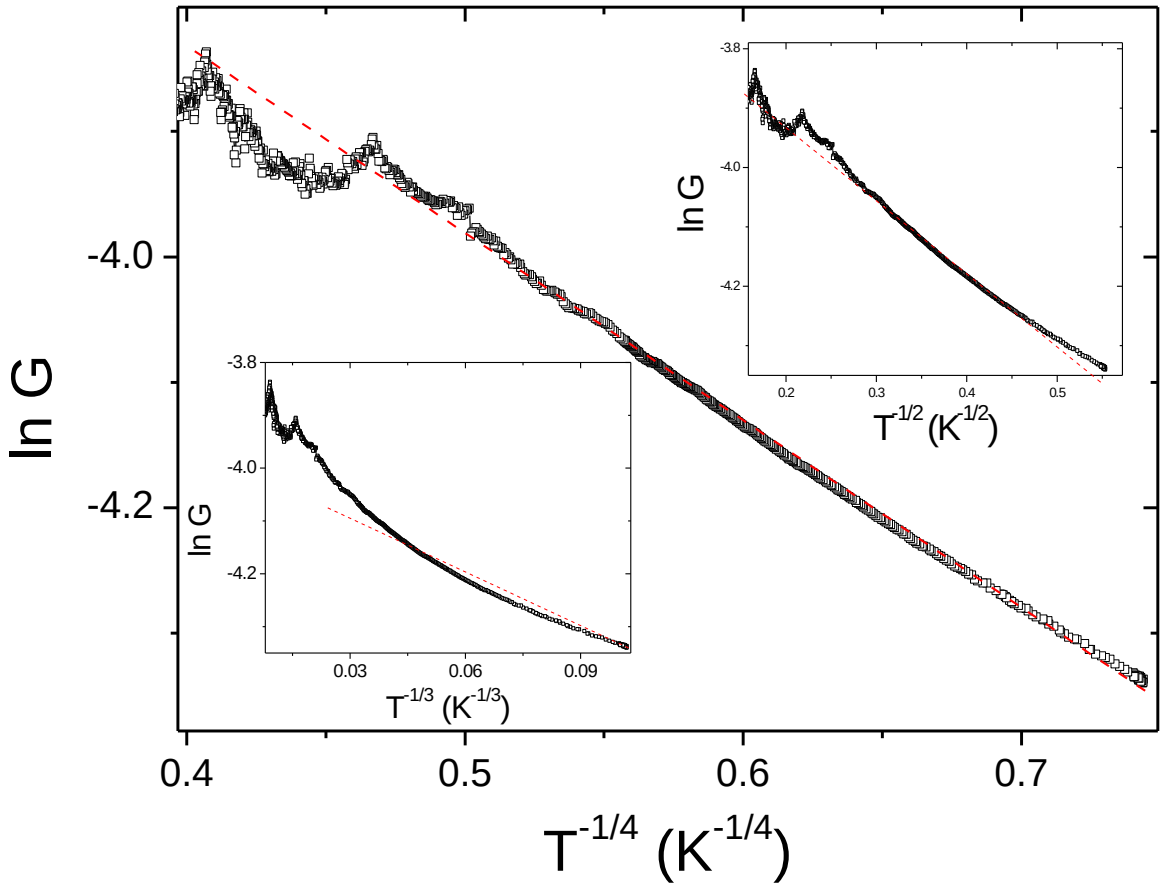


Fig 6.4: *ln G vs $T^{-1/4}$ to check for 3D VRH mechanism in 27% FeMWNT sample. Top insert is a plot of ln G vs. $T^{-1/2}$ (Coulomb gap VRH) and the bottom insert is for ln G vs. $T^{-1/3.}$ (2D VRH).*

In the 27% Fe-MWNT sample we observe a different behavior from the sample discussed earlier. From the inserts of Fig 6.4 we see that the Coulomb gap VRH fit (Top insert) and 2D VRH (Bottom insert) mechanisms do not give an appropriate description of the conduction in this sample at low temperatures. Instead the 3D VRH (Mott Law) has a better fit compared to the other two. Therefore in the 27% Fe-MWNT sample at low temperature the conduction mechanism is 3D VRH. This transition from E-S to Mott mechanism is due to shielding of the coulomb gap by the increased electrons in the 27% sample [**54**].

The magnetoresistance measurement (Fig 6.5) for this sample shows a similar general trend to the 5% FeMWNT sample. However to make a better comparison we plot the MR data at the same temperature on the same axis (Fig 6.6).

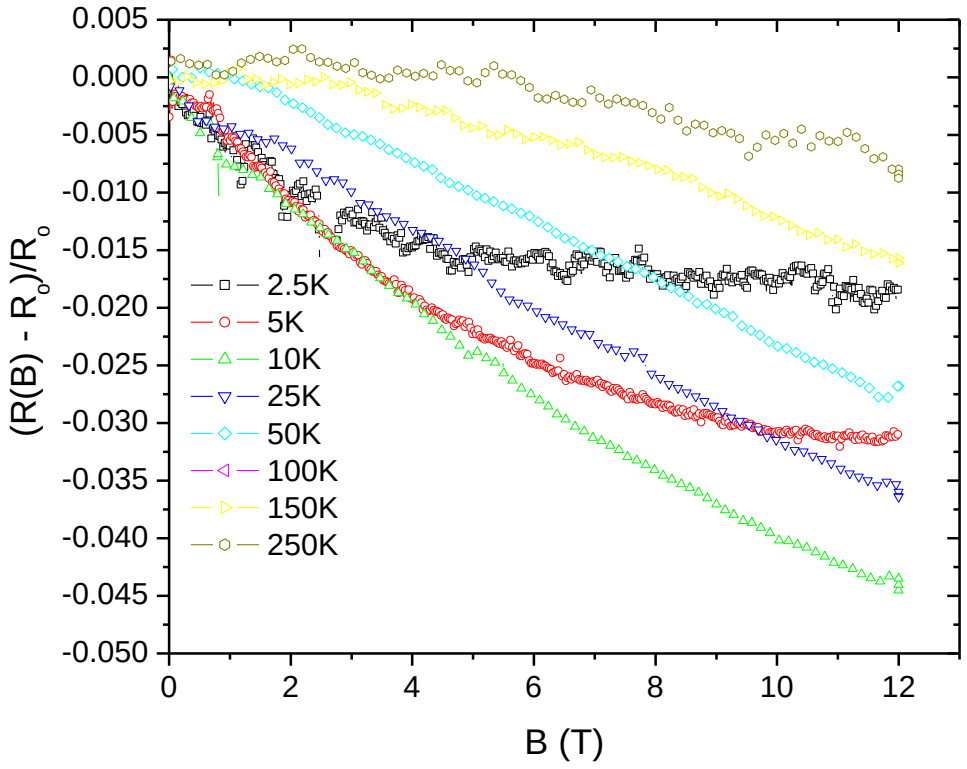


Fig 6.5: *Normalized MR results for the 27% Fe-MWNT sample showing that at low temperatures we have an upturn of the MR.*

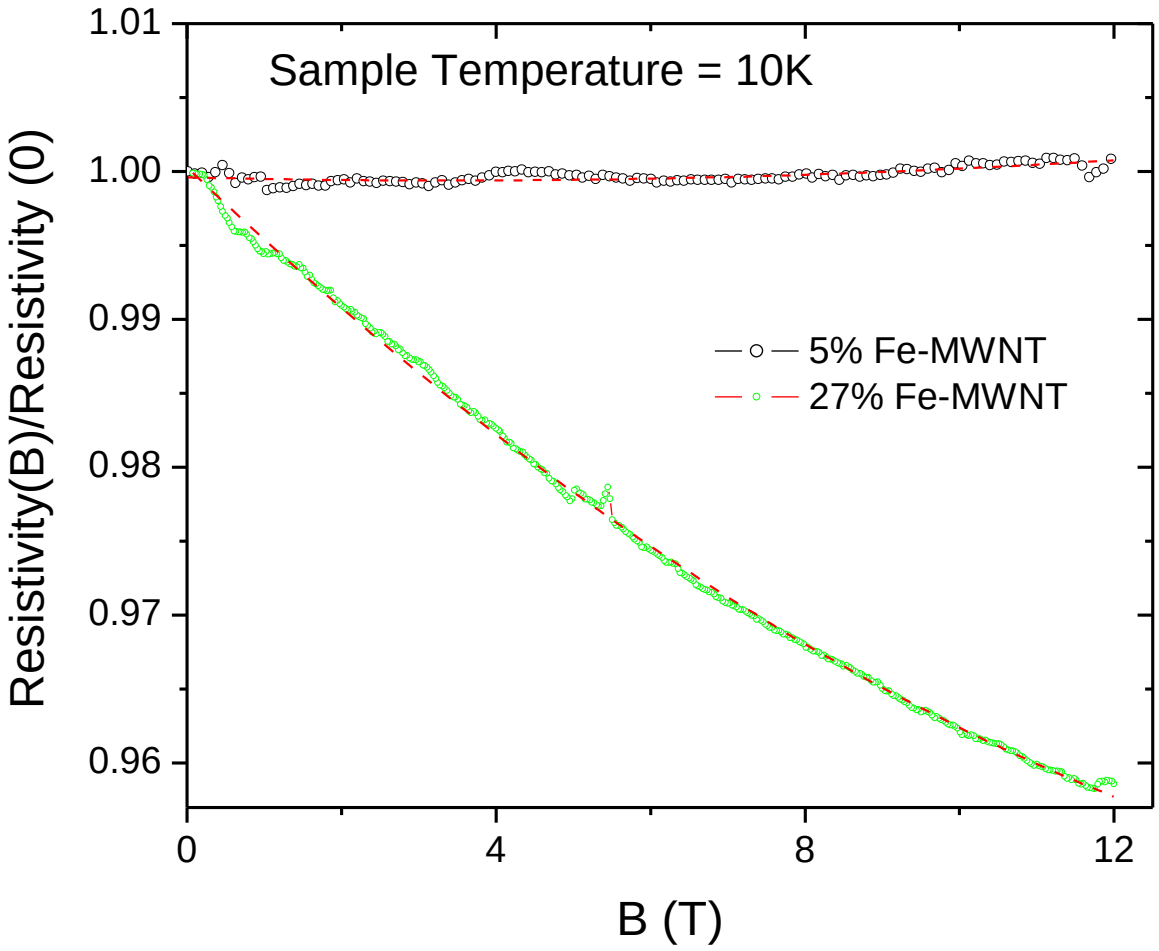


Fig 6.6: *MR measurements at 10 K for the 5% and 27% samples and the respective fitting using equation 15.*

The graph (Fig 6.6) clearly shows pronounced contributions from the wavefunction shrinkage resulting in a positive MR for the 5% carbon nanotube sample as opposed to what is observed in the 27% sample where we have more of the forward interference mechanism as indicated by the negative MR. Fitting the data above (Fig 6.6) using equation (17) we are able to determine the electron localization lengths of the two samples. While the VRH fittings give us the characteristic temperatures see Table 6.1.

The low values of the localization lengths L_c support the fact that we have strong localization and hence hopping conductivity will be the main conduction mechanism in Fe-MWNT. As can be seen from the table, the localization is stronger in the 5% Fe-MWNT sample than it is in the 27% Fe-MWNT. This point is further strengthened by the very low value of a_1, which is an indication of the negative contribution due to the forward interference mechanism. The values of a_2 which indicate the contribution from wavefunction shrinkage are almost of the same order of magnitude and therefore the difference in the films is mainly due to the forward interference. Forward interference in strongly localized systems has been attributed to the interference of the many hopping paths. Since one sample has more iron we speculate that the density of states in this sample is much higher and thus the probability of constructive interference is higher. Other researchers have suggested that negative MR in strongly localized systems is no different to that in weak localized systems [**55**]. We will therefore check for the possibility of weak localization in the 27% Fe-MWNT sample.

Table 6.1: *A table showing some of the calculated parameters for the samples. T_{ES} and T_{mott} are the characteristic temperature according to the ES and Mott model. $L_{c(ES)}$ and $L_{c(mott)}$ are the localization length at 10K according to the ES and Mott models respectively. a_1 and a_2 have been defined in equation (17).*

Sample	**T_{ES}** **(K)**	**T_{mott}**	**Fitting Parameters at 10K**		**$L_{c\ (ES)}$** **(nm)**	**$L_{c\ (Mott)}$**
			a_1	**a_2**		
5%	72.6		1.3×10^{-4}	2×10^{-5}	3.66	
27%		4.48	5.0×10^{-2}	1.2×10^{-4}		14

6.5 Weak Localization in Fe-MWNTs

In this section we present results of electronic transport in iron filled multiwalled carbon nanotubes which have not been reported so far in multiwalled carbon nanotube networks. In our analysis we observed 3D weak localization in the 27% Fe-MWNT sample. This mechanism was modeled by Ramakrishnan et al [**56**] and is governed by the equation (18) below.

$$\sigma_{3D}(T) = \sigma_0 + \frac{e^2}{\hbar\pi^3}\frac{1}{a}T^{p/2} \qquad (18)$$

where *a* is the cross sectional diameter of the sample and *p* is an index depending on the dimensionality and scattering mechanism. The other symbols have their usual meaning.

As indicated earlier, weak localization effects result from the constructive interference of partially backscattered electron waves travelling back along time reversed paths and occur when elastic scattering dominates. Since the inelastic scattering time is inversely proportional to T^P (i.e. $\tau_{in} \alpha T^{-P}$) where *P* depends on the scattering mechanism, weak localization effects are observed at low temperatures when inelastic scattering time is much greater than the elastic scattering time [**57**]. Fitting equation (18) to our low temperature conductivity data Fig 6.7 below indicates a low temperature dependence i.e. $\sigma_{WL} \alpha T^{0.28}$. Giving a value for P = 0.56. This value is in the same order of magnitude to that reported in K- intercalated MWNTs and SWNT ropes whose *P* values are 0.3 and 0.397 respectively [**58**] . Such values of *P* indicate that none of the common 3D scattering mechanism is applicable for our MWNTs network. In perfect periodic 3D potentials *p* = 2 and *p* = 3 for electron-electron scattering and electron- phonon scattering respectively [**58**].

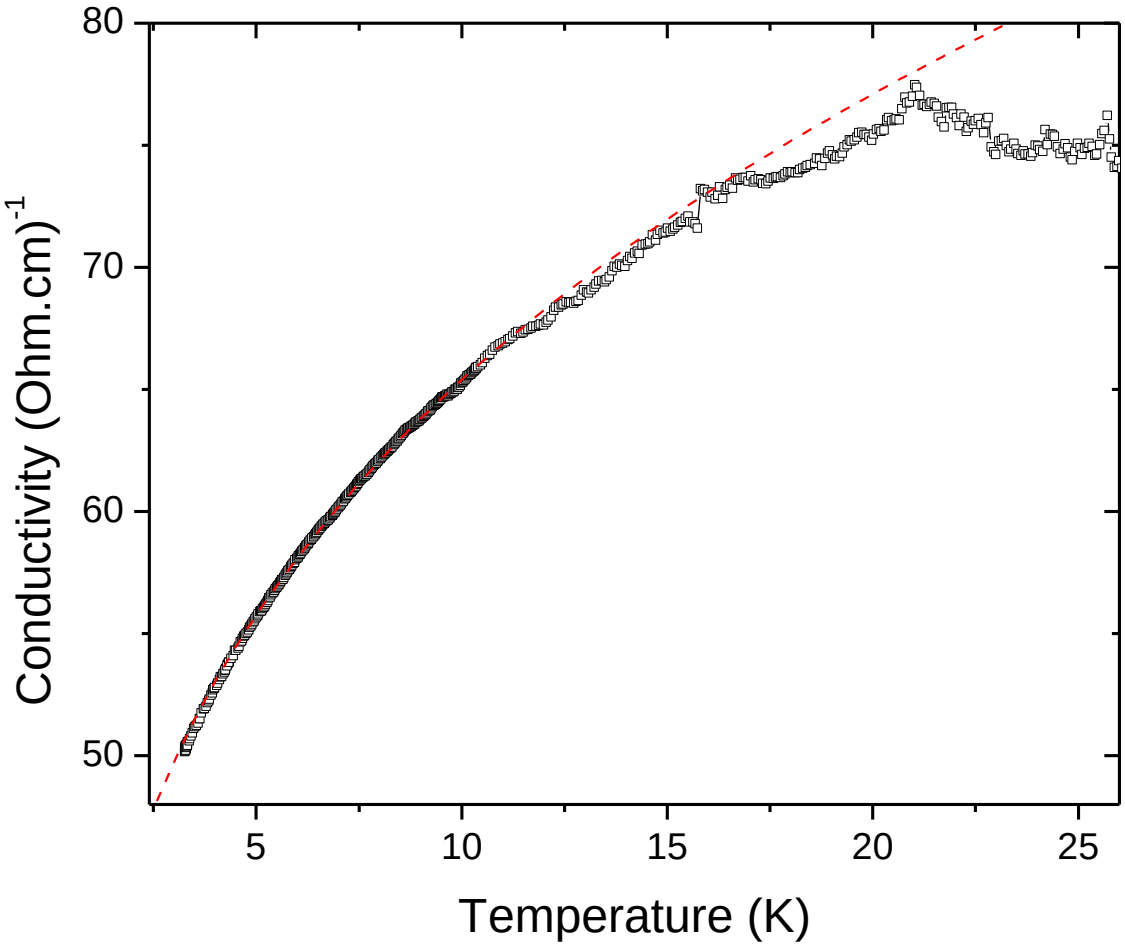


Fig 6.7: *Conductivity – Temperature graph, showing that 3D WL can best describe the conduction mechanism in this temperature range for the 27% Fe-MWNT sample.*

We now turn our attention to the magneto-conductance data to verify this observation. The theory of magneto-conductance change due 3D WL was formulated by Kawabata and is governed by the equation (19) below

$$\Delta\sigma_{WL}(B,T) = \frac{e^2}{2\pi^2}\frac{1}{\hbar l_B}F(\delta) \qquad (19)$$

where the magnetic length $l_B = \sqrt{\hbar/eB}$. The function F (δ), where $\delta = 3{l_B}^2/4l l_B$, ℓ is the elastic scattering length, has two limits for an analytical solution of the form $\Delta\sigma_{WL} \alpha B^n$ exists,

$$\Delta\sigma_{WL}(B,T) = C\sqrt{B}\ (\Omega\text{cm})^{-1} \text{ when B is in Tesla for } \delta \ll 1 \qquad (20)$$

And $$\Delta\sigma_{WL}(B,T) = c\,T^{-3p/4}B^2 \quad \text{for } \delta \gg 1 \qquad (21)$$

The condition in equation (20) is observed for high fields at low temperatures and the square root of *B* behavior of the conductivity is independent of system parameters, a behavior unique to 3D WL [**59**].

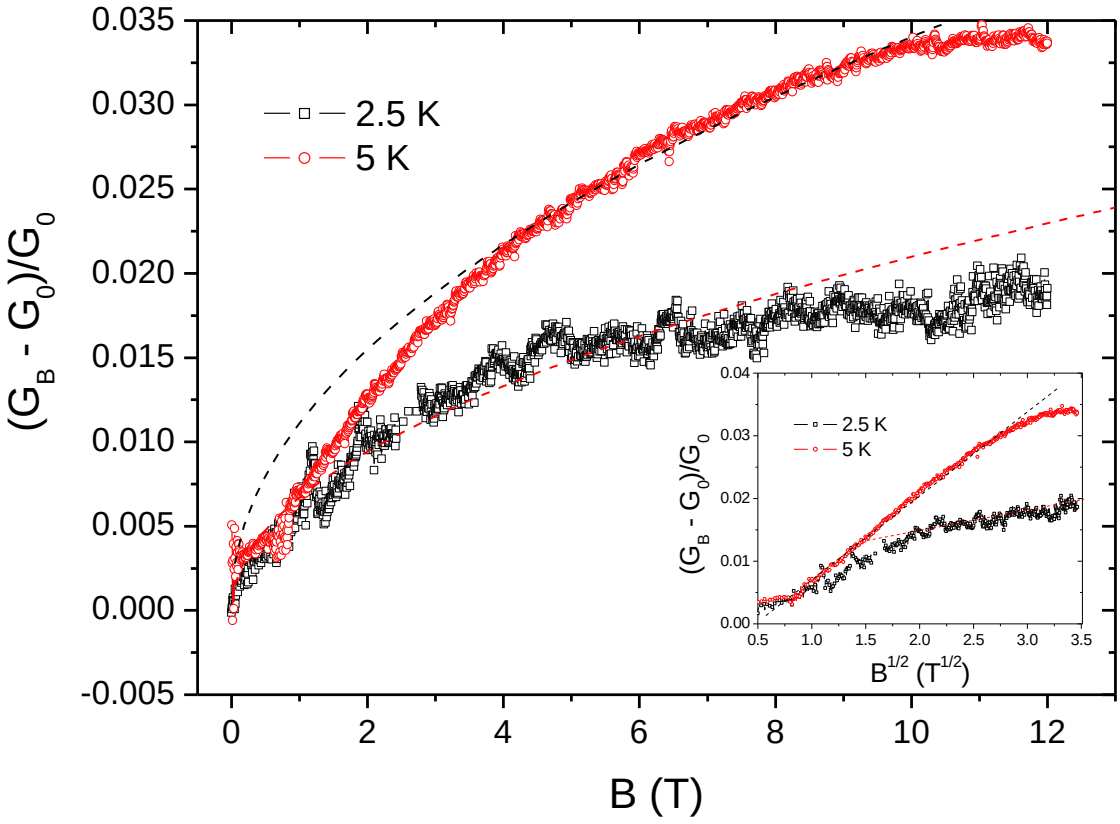


Fig 6.8: *Magneto-conductance data fitted with equation (20), the insert shows the same data plotted against the Square root B scale to show the applicability of the model at high fields for the 27% Fe-MWNT sample.*

Fitting our magneto-conductance data with equation (20) which describes the behavior at high fields and low temperature so as to satisfy the condition $\delta \ll 1, \text{when } \ell_B \sim \ell$. We observe that the model is very appropriate for our data at high fields and low temperature as shown by the graph, Fig 6.8. From the MR data which was given earlier in Fig 6.5 it is clear that this WL model breaks down above 10K where we observe linear dependence of MR with magnetic field. This is in agreement to the suggestion of the conductivity data Fig 6.7 which indicates very good WL fit at low temperatures below 10K. We however are unable to extract and compare the characteristic parameters such as the elastic scattering length because we have no means of approximating the cross- sectional diameter of the material since it is not a single carbon nanotube but a network. Plans are however, at an advanced stage to eliminate this obstacle as we hope to study single MWNT's in the near future. We nevertheless suggest that the physical origin of this weak localization occurs within the disordered metallic nanowires in the core of the MWNTs. The predominating hopping mechanism outlined earlier is of electrons from the one metal site to another, since the iron is discontinuous in the MWNTs.

6.6: Electronic transport in Fe-MWNT – Conclusion

The observations made thus far have shown different electronic transport mechanisms between the mainly sp^2 bonded carbon and the sp^3 carbon. In the Iron filled MWNT a hopping conductivity mechanism is the dominate process with some small contribution from weak localization in highly filled Fe-MWNT unlike in nanodiamond films. The increased iron content in MWNT has been seen to introduce a transition from Efros-Shklovskii (E-S) to the convectional Mott 3D VRH. This has been explained in terms of the fact that the increased iron content enhances the shielding of the Coulomb potential which is responsible of the E-S mechanism. We also observed an improved conductivity as the iron content was increased which should be expected and the reasonable explanations are as follows. Since the iron was found to be discontinuous inside the tubes, we could have additional hopping of electrons from strongly localized iron sites to the next. Furthermore we observed 3D weak localization which we attributed to the metal nanowires in the core of the nanotubes. The iron can also introduce free electrons that can diffuse along the weakly coupled shells and this also would increase the conductivity. We are not able at present to distinguish between the two mechanisms.

The magnetoresistance measurements have shown us wave function shrinkage at very low temperatures which was evidenced by the positive MR at these temperatures and high magnetic fields. The relative magnitude of this positive contribution was less for the much filled samples due to the increased density of states near the Fermi level which means that localization length is increased and the effect of wave function shrinkage is reduced.

As the temperature and iron content was increased, the MR was negative which we attributed to the quantum forward interference of the different hopping paths. This negative MR was observed to be linear at high fields and parabolic at low fields as observed by other workers [**60**]. The reason for this is due to the additive contribution of two mechanisms (wave function shrinkage and quantum interference) at high fields which is not present at low fields.

Chapter 7

Conclusions and Recommendations

7.1 Synthesis of nanodiamond films

Nanodiamond films were synthesized on both silicon and fused silica (quartz) substrates using the HFCVD technique. The average sizes of the nanodiamond clusters varied from 20 nm to 600 nm, with a continuous film mainly at the centre of the substrate i.e. the area directly over the filament. The diamond quality and morphology was found to depend on the gas chemistry, pressure and temperature. The growth rate was found to be highly substrate temperature dependant i.e. increase in temperature resulted in an increase in the growth rate and as such for future studies on this parameter an introduction of a separate substrate heater is recommended as this would allow higher deposition temperatures above $850^{o}C$, the limit of our apparatus. An optimum distance between filament gap and the substrate was found to be 4 mm. The nanodiamond films were made conductive by introducing about 20% or more nitrogen in the gas composition. Nitrogen incorporation in the diamond films introduced more disordered sp^2 phases in the film. These observations were made possible through characterization using Raman Spectroscopy, AFM, SEM and TEM.

7.2 Electronic transport properties of nitrogen doped HFCVD films

The electrical transport measurements of nanodiamond films gave us some well known quantum features observed in disordered materials. However, the conductivity in these films (HFCVD) could not be explained using one mechanism over the entire temperature range. Within the low and intermediate temperature range the activated conduction and semi-metallic behavior were found to be the main mechanisms depending on the amount of nitrogen in the chamber. The semi-metallic behavior is characterized by 3D weak localization and electron-electron interactions processes. The dephasing length was found to be weakly temperature dependant, with a temperature dependence of $T^{-0.33}$. This implies a $T^{-0.66}$

dependence for the dephasing time of the electronic wavefunction. This kind of behavior has been reported in artificial superlattice structures where the conductivity is governed by tunneling transport.

The temperature dependence of the dephasing time plays an important role in determining the characteristics of diamond based nano-electronic devices. The magnetoresistance measurements could best be explained using the 3D anisotropic weak localization model and the anisotropic coefficient was approximately in the range from 1.5 to 2.3, which is close to 3, a figure reported by other researchers in MWCVD ultrananocrystalline diamond. The origin of the anisotropic behavior is not yet fully understood but we believe this is due to anisotropic distribution of disorder in the gain boundaries. The relative extent of the disorder depends on the synthesis conditions - as observed in our research.

The microwave prepared nanodiamond samples had a smaller anisotropic coefficient compared to the HFCVD-N_2 films. More work on this subject is recommended because we have not yet established what parameter really brings about this behavior. However, when fully understood this anisotropic property would help realize the use of these materials in magnetic sensors and related electronics.

Further to the above observations we also found that the semi-conducting HFCVD-N_2 films were highly insulating at very low temperatures, such that it was difficult to measure their electrical properties from 2.3K to 20 K. This was not the case with the semi-metallic HFCVD-N_2 or MWCVD-N_2 films which we found to be highly conducting even at these low temperatures and had a more pronounced contribution from electron-electron interactions. This we attribute to the high energy of the MWCVD method which enhances the incorporation of nitrogen into the films even with less nitrogen in the chamber. The electron-electron interactions we attribute to the high density of free electrons in the films, although still less than that in metallic film, it makes a significant contribution to the conduction. From our observation in nanodiamond films there is very little contribution from the hopping mechanism. We also did not observe positive MR as is the case with multiwalled carbon nanotubes where hopping dominates.

7.3 Electronic transport in Fe-MWNTs

Finally, studies on Iron filled MWNT have shown us that in mainly sp^2 bonded materials such as MWNT networks we have a different transport mechanism from that in mainly sp^3 carbon materials such as nanodiamond films. Research by us and other researchers has shown that the hopping mechanism dominates in CNT networks, which is not the case in nanodiamond films. This might brush aside the notion that conductivity in nanodiamond films is purely due to the sp^2 phases in the films. Our results suggest a totally different behavior from carbon nanotube networks. Metal incorporation in the MWNT networks has been seen to alter the conduction mechanism, from E-S VRH to Mott VRH in 3D as the metal content was increased. Furthermore there was an increase in the characteristic field at which the MR turned from negative to positive with the increase in iron content.

We also observed 3D weak localization effects below 10K in the 27% Fe-MWNT sample which we attributed to the metal nanowires at the core of the nanotubes. Since the iron is not continuous in the nanotubes the contribution of these effects (WL) to the conduction is not much, instead we have hopping being the dominating conduction mechanism. We have therefore demonstrated that transport in MWNTs can be controlled by incorporating iron in the core of the tubes. This work is a prerequisite for carbon based spintronic devices.

7.4 Recommendations

As we have indicated in subsection 7.2 more work is needed to try and understand the origin and parameters that determine the anisotropic behavior in nanodiamond films. Our results have indicated pronounced anisotropy in less conducting films than in more conducting films in which we would expect more structural defects due to increased nitrogen which then raises questions as to what determines this anisotropy.

We also recommend the introduction of a separate substrate heater to the synthesis apparatus so as to allow higher temperature deposition. We believe this would improve the growth rate significantly and maybe enhance nitrogen incorporation in the HFCVD films. In future we would

like to study quantum Hall capacitance or superconductivity in nanodiamond films heavily doped by nitrogen or other impurities.

Finally, synthesis and weak localization studies in single metal filled carbon nanotubes is recommended as to try and distinguish between negative MR due to hopping and that due to weak localization. This however, requires continuously filled carbon nanotubes and hence the need for more work in the synthesis of such nanotubes (i.e. continuously filled carbon nanotubes). And therefore for future studies we would like to improve the synthesis of Fe-MWNT by a pulsed laser assisted deposition technique.

Appendix

A: Nanodiamond film dimensions used during electrical transport measurements.

Sample	Thickness (m)	Length (m)	Width (m)
10% MWCVD-N_2	5×10^{-7}	4.03×10^{-2}	3×10^{-3}
20% MWCVD-N_2	3×10^{-7}	1.02×10^{-3}	1×10^{-3}
20% HFCVD-N_2	2.18×10^{-8}	5×10^{-3}	5×10^{-3}
22% HFCVD-N_2	3.23×10^{-8}	4×10^{-3}	3×10^{-3}

B: Fe-MWNT Sample dimensions used during the electrical transport measurements.

Sample	Thickness (m)	Length (m)	Width (m)
5% Fe-MWNT	5×10^{-4}	5×10^{-3}	3×10^{-3}
27% Fe- MWNT	5×10^{-4}	5×10^{-3}	$2{,}6 \times 10^{-3}$

Bibliography

1. G.V. Samsonov & V.A. Obolonchik, "Frederic Henri Moissan, on the 120th anniversary of his birth"- Powder Metallurgy and Metal Ceramics, vol **11** No 9 DOI: 10.1007/BF00801283, 766.
2. K. Lonsdale, "Further comments on attempts by H. Moissan, J.B. Hanny and Sir Charles Parsons to make diamonds in the Laboratory"- Nature 196:104 DOI 10:1038/ 1961 (1962)
3. H. Tracy Hall, "Diamond synthesis"- US Patent office 2947,608- 02/08 (1960)
4. O.A. Williams, M. Nesladek, M. Daenen, S. Michaelson, A. Hoffman, E. Osawa, K. Haenen, R.B. Jackman, "Growth, electronic properties and applications of nanodiamond", Diamond Relat. Mater. **17**, 1080 (2008).
5. www.e6.com- "The secret life of diamond".
6. A. Krueger, "New carbon materials: Biological applications of functionalized nanodiamond materials"- Chem. European J. vol **14**, 1382 (2008).
7. G.L. Hornyak, H.F. Tibbals, J. Dutta, J.J. Moore - Introduction to Nanoscience and Nanotechnology-CRC Press (Taylor V. Francis Group LLC) - Ch 6 & Ch 17, 2289-295 & 934-935, (2009).
8. B.I. Kharisov, O.V. Kharissova, L. Chavez-Guerrero, "Synthesis and Reactivity in inorganic, metal organic and Nano organic", Metal Organic and Nano-metal Chem. **40**, 84 (2010).
9. W. Zhu, G.P. Kochanski, S. Jin, L. Seibles, D.C. Jacobson, M. McCormack, "Electron field emission from ion- implanted diamond", Appl. Phys. Lett. **67**, 1157 (1995).
10. S. Bhattacharyya, "Synthesis and Characterization of highly-conducting nitrogen-doped ultrananocrystalline diamond films", Appl. Phys. Lett. **79** 1441 (2001).
11. S. Bhattacharyya, "Mechanism of high n-type conduction in nitrogen doped nanocrystalline diamond", Phys. Rev. B **70**, 125412 (2004). S. Bhattacharyya, "Two-dimesional transport in disordered carbon and nanocrystalline diamond films", Phys. Rev. B **77**, 233407 (2008).

12. F.J. Himpsel, J.A. Knapp, J.A. Van Vechten, D.E. Eastman, “Quantum photoyield of diamond (111): A stable negative affinity emitter”, Phys. Rev. **20**, 624 (1979).
13. K. Subramanian, Y.M. Wong, W.P. Kang, J.L. Davidson, B.K. Choi, “Field emission devices for advanced electronics comprised of lateral nanodiamond or carbon nanotubes emitters”, - Diamond Relat. Mater. **16**, 1997 (2007)
14. S.A. Rakha, X. Zhou, Y.G. Suixia, H. Cao, “Influence of CH_4 on the morphology of nanocrystalline diamond films deposited by Ar rich microwave plasma”, J. Appl. Phys. **107**, 1114324 (2010).
15. T. Ikeda, K. Teii, C. Casiraghi, J. Robertson and A.C. Ferrari, “Effect of sp^2 carbon phase on n-type conduction in nanodiamond films”, J. Appl. Phys. **104**, 073720 (2008)
16. E. Rattner- TFoT Newsletter 16/04 (2008).
17. J. Isberg, J. Hammersberg D.J. Twitchen, A.J. Whitehead, “Metal contacts to boron doped diamond”, - Diamond Relat. Mater. **13**,320 (2004).
18. M. Nesladek, D. Tromson, P. Bergonzo, P. Hubik, J.J. Mares, J. Kristofik, D. Kindi, O.A. Williams, D. Gruen, “Low temperature MR study of electrical transport in N- and B-Doped UNCD and NCD diamond films”, Diamond Relat. Mater. **15**, 607, (2006).
19. Y. Tang, “Ploy-crystalline Diamond (Poly C) Technology and Piezoresistive sensor Applications for Cochlear Prosthesis”, PhD Dissertation, Michigan State University, (2006).
20. S. Koizami, C.E. Nebel and M. Nesladek, “Physics and applications of CVD diamond”- Weiley-VCH Verlay G m6 H and Co- (2008).
21. S.B. Nornes , E.E. Donaldson, S. Matsumoto, H. Tosaka, T. Yoshida, M. Kobayashi & A. Yoshikawa, “ Nitrogen doping into ZnSe by catalysis of Transition metal”, J. Chem. Phys. **44**, 2968 (1966).
22. P.W. May, M.N.R. Ashfold & Y.A. Mankelevich, “MCD, NCD & UNCD chemical vapour deposition: Experimental and modeling of the factors that affect the growth rate, nucleation and crystal size”- J. Appl. Phys. **101,** 053115 (2007).
23. P.W. May , Y.A. Mankelevich, “Experiment and Modeling of UNCD deposition using HFCVD: A generalized mechanism for UNCD growth”, J. Appl. Phys. **100**, 024301, (2006)

24. T. Lin, G. Y. Yu, A. T. S. Wee, and Z. X. Shen, K.P. Loh, “Compositional Mapping of the Ar-Ch_4-H_2 system for polycrystalline to nanocrystalline diamond film growth in an HFCVD system”, Appl. Phys. Lett. vol **77**, 17 (2000).
25. A.C. Ferrari and J. Robertson, “Raman spectroscopy of amorphous nanostructure diamond like carbon and nanodiamond”, R. Soc. **10**, 1098 (2004).
26. R.J. Nemanich, J.T. Glass, G. Lucovsky, R.E. Schroder, “Raman Scattering characterization of carbon bonding in diamond and diamondlike thin films”, J. Vac. Sci. Technol. A **6**, 1783 (1988).
27. A.T. Sowers, B.L. Ward, S. English, R.J. Nemanic, “Growth, microstructure and field-emission properties of nitrogen doped diamond films”, J. Appl. Phys. **86**, 3973 (1999).
28. L.C Qin, D. Zhou, A.R. Krauss & D.M. Gruen, “TEM characterization of nanodiamond thin films”, Nanostructured Materials, vol **10**, No 4, 649 (1998).
29. S. Datta, “Electronic Transport in Mesoscopic System”, Cambridge University Press, Cambridge, (1995).
30. R. Schmechel, “Gaussian disorder model for high carrier densities: theoretical aspects and applications to experiments”, Phys. Rev. B **66**, 235206 (2002).
31. A. Bachtold, M. Henny, C. Terrier, C. Strunk, C. Schonenberger, J.P. Salvetat, J.M. Bonard, L. Forro, “ Contacting carbon nanotubes selectively with low ohmic contacts for four probe electric measurements”, Appl. Phys. Lett. **73**, 274 (1998).
32. G. Bergmann, “Weak localization in tunnel junctions”, Phys. Rev. B **39**, 11280 (1989).
33. S. Washburn, R.A. Webb, “Quantum transport in small disordered samples from diffusive to ballistic regime”, Rep. Prog. Phys. **55**, 1311 (1992).
34. N. W. Ashcroft, N.D. Mermin, “Solid state Physics”, Saunders College, pp 6-7, ISBN 0-030839-939.
35. M.S. Kang, W.S. Lee & Y.J. Baik, “Morphology variation of diamond with increasing pressure up to 400 torr during deposition using HFCVD”, Thin Solid Films 398-394, 175 (2001).

36. S. Schwarz, S.M. Rosival, M. Frank, D. Breidt, R.F. Singer, “Dependence of growth rate, quality and morphology of diamond coatings on Pressure during the CVD process in an industrial HFCVD plant”, Diamond Relat. Mater. **11**, 589 (2002).
37. A. Datta, “Heat of dissociation of Nitrogen”, Nature **129**, 870 doi 10, 1038/12987 0b0 (1932).
38. S. Bhattacharyya, “Novel electronic structure and transport properties of confined disorder carbon layers”, Phys. Stat. Sol. B **246** No 5, 1056 (2009).
39. Y. Dai, D. Dai, C. Yan, B Huang & S. Han, “N-type electric conductivity of nitrogen-doped ultrananocrystalline diamond films”, Phys. Rev. B **71**, 075421 (2005).
40. P. Zapol, M. Sternberg, L.A. Curtiss, T. Frauenhein, and D.M. Gruen, “Tight- binding molecular-dynamics simulation of impurities in UNCD diamond grain boundaries”, Phys. Rev. B **65**, 045403 (2001).
41. G. Du, V.N. Prigodin, A. Burns, J. Joo, C.S. Wang, A.J, Epstein- Phys. Rev. B **58**, 4458 (1998).
42. N.F. Mott and M. Kavesh, J. Phys. C **14** L 659; A. Lee and T.V. Ramankrishnan- Rev. Mod. Phys. **57**, 287 (1985); N.F. Mott, Metal-Insulator Transitions, (Taylor and Francis, London 1990).
43. K. Shah, Z. Chiguvare, S. Bhattacharyya, “Anisotropic weakly localized transport in nitrogen-doped ultrananocrystalline diamond films”, Phys. Rev. B **82**, 184206 (2010).
44. W. Szott, C. Jedrzejek, and W.P. Kirk, Phys. Rev. Lett. **63**, 1980 (1989); A. Cassm-Chenai and D. Mailly, Phys. Rev. B **52** 1984 (1995).
45. A. Kanapitsus, C. Tsonos, D. Triantis, I. Starrakas, C. Anastasiadis, P. Photopoulos, P. Pissis, V. Em. Vamvakas, “Thermally activated conduction mechanism in silicon nitride MIS structures”, Thin solid films 518, 2357 (2010).
46. N.F. Mott, “Conduction in Non-crystalline materials”: Oxford University Press: Oxford pp 27 (1987).
47. B.I. Shklovskii & A. Efros, “Electronic properties of Doped Semiconductors”: Springer-Verlag, Berlin- pp 228 (1984).

48. M. Jaiswal, W. Wang, K.A. Shiral Fernando, Ya-Ping Sun, & R. Menon, “Magnetotransport in single–wall carbon nanotubes networks”, Phys. Rev. B **76** 113401 (2007).
49. A. Bright, Phys Rev. B **20**, 5142 (1979); V. Bayot, L. Piraux, J.P. Michenaud, J.P. Issi, M. Lelaurain, & A. Moore, Phys. Rev. B **41** 11770 (1990).
50. Y. A. Pusep, M.B. Ribeiro, H. Arakaki, C.A. de Souza, S. Malzer, and G.H. Dohler, Phys. Rev. B**71**, 035323 (2005); J. Chiguito, Yu. A. Pusep, G.M. Gusev and A.I. Toropov, Phys. Rev. B**66**, 035323 (2002).
51. S. Bhattacharyya, S.J. Henley, E. Mendoza, L.G. Rojas, J. Allm and S.R.P, Silva, “Resonant tunneling and fast switching in amorphous carbon quantum well structures”, Nature Mater. **5**, 19 (2006).
52. Y.A. Pusep, M.B. Ribeiro, H. Arakaki, C.A. de Souza, P.A. Zanello, A.J. Chiquito, S.Malzer, and G.H. Dohler, “Anisotropy of Quantum interference in disordered GaAs/$Al_xGa_{1-x}As$ superlattices”, Phys. Rev. B **68**, 195207, (2003)
53. W. Schirmacher, “Quantum-interference magnetoconductivity in the VRH regime”, Phys. Rev. B **41** 2461 (1990).
54. K. Yanagi, H. Udoguchi, S. Sagitani, Y. Oshima, T. Takenobu, H. Kataura, T. Ishida, K. Matsuda, Y. Maniwa, “Transport Mechanism in Metallic and Semiconducting Single-Wall carbon Nanotube networks”, American Chemical Society vol **4**. No 7 4027, (2010).
55. Y.Z. Long, Z.H. Yin and Z.J. Chen, “Low- Temperature Magnetoresistance Studies on Composite films of conducting Polymer and Multiwalled Carbon Nanotubes”, J. Phys. Chem. C, **112**, 11507 (2008).
56. T.V. Ramankrishnan, P.A. Lee, “Disordered Electronic systems”, Rev. Mod. Phys. vol **57** No 2, 287, (1985).
57. M. Baxendale, V.Z. Mordkvich, and S. Yoshimura, “Magnetotransport in bundles of intercalated carbon nanotubes”, Phys. Rev. B **56**, No 4, 2161, (1997).
58. S.N. Song, X.K. Wang, R.P.H. Chang, and J.B. Ketterson, “Electronic Properties of Graphite Nanotubules from Galvanomagnetic Effects”, Phys. Rev. lett., vol **72**, No 5, 697, (1994).

59. A. Kawabata, “Theory of Negative Magnetoresistance”, J. Phys. Soc. Jpn. **49**, No 2, 628, (1980).
60. Y.Z. Long, Z.H.Yin & Z.J. Chen, “Low Temperature magnetoresistance studies on composite films of conducting polymer and multiwalled carbon nanotubes”-J. Phys. Chem. C **112**, 11507 (2008).